GNSS-R Remote Sensing of the Ocean: Surface Waves and Related Phenomena

by
David D. Chen

A dissertation submitted in partial fulfillment
of the requirements of the degree of
Doctor of Philosophy
(Electrical Engineering)
in the University of Michigan
2016

Doctoral Committee:
Professor Christopher S. Ruf, Chair
Professor Jeremy N. Bassis
Associate Research Scientist Roger D. de Roo
Professor Leung Tsang

En route to Vancouver Island, August 12, 2004.

To You
Yes, *you*. Because, despite our differences, we have much in common…

Acknowledgements

Throughout the course of my Ph.D. program, I have worked on a multitude of different projects, many of which do not appear in this thesis. Nonetheless, I’d like to acknowledge here everyone who has made a significant contribution to my research and education in the past several years.

First, I would like to acknowledge my research advisor, Chris Ruf. I, as one of a rather opinionated nature, have not always followed his advice. However, I know he has always advised me with my best interests at heart. And that is all I can ask for from an advisor.

In addition to Chris, I have benefitted from the mentorship of Roger de Roo, Jeremy Bassis, Leung Tsang, Valery Zavorotny, Paul Hwang, and Scott Gleason. I am also grateful for the input and advice of Bill Plant, Mark Donelan, and David Lyzenga. I thank Hitoshi Tamura, Mounir Adjrad, Tony England, Roger Backus, Ron Rizor, Paolo de Matthaeis, Tripp Collins, Andrew O’Brien, Michael Long, Faozi Said, Brandon Reichl, Jeonghwan Park, and Rachael Kroodsma for their help and support. Aaron Ridley, Marc Perlin, Manjunath Ganesh, Deepak Singh, David Austerberry, Tianlin Wang, Mary Morris, Maria-Paola Clarizia, Sid Misra, John Xun Yang, Derek Posselt, Justin Tsu, Darren McKague, Amanda Mims, and Kamal Sarabandi have also contributed to my studies in various capacities.

I am grateful for the encouragement of my friends; they include Josué Carranza, Xiaoen Ju, Jasmine Jones, Yuanyuan Zhou, John Wang, Yang Li, Jinjin Pan, Jielun Tan, Shiya Song, and Haipeng Wu. I have learned a great many computer tricks from Bryan White, Darren Britten-Bozzone and Melissa Terwilliger from the IT Department; their expertise and enthusiasm put a silver lining on every IT problem. The kindness and dedication of my high school teachers Peter Mleziva and Maureen de St. Croix have been a source of inspiration that pushed me onwards.

I am grateful to NASA and NSERC for providing the bulk of my financial support over the years.

I thank my family. They have shared the ups, downs, and everything in between with me over the years, and gave me unfaltering support, as well as room to discover things for myself.

Valuable feedback from my committee was taken into account in the revisions of this thesis. Any remaining errors in the text are my responsibility and mine alone.

D. D. C. Z.
September 2016
Ann Arbor, Michigan, USA

Contents

List of Figures

List of Tables

List of Appendices

Abstract

In this thesis, we explore several fundamental issues in GNSS-R remote sensing. Global Navigation Satellite System - Reflectometry (GNSS-R) is a relatively young remote sensing technique proposed to measure geophysical surface features and processes, such as ocean surface wind speed and roughness. GNSS-R uses a bistatic geometry at L-band frequencies. These two factors imply GNSS-R sense longer surface waves than traditional radar scatterometers and altimeters. Longer waves are known to take a longer time and more spatial coverage to respond to wind and propagate further before decaying. Our focus in this thesis is on quantifying some of these effects in the context of GNSS-R sensing of windspeed. We first attempt to bound the response time of GNSS-R surface roughness due to wind, using in-situ buoy measurements. These measurements are then used to validate a surface wave model. Coupling this surface wave model with an electromagnetic scattering model, we develop a novel end-to-end forward model for GNSS-R. This model shows superior performance against spaceborne GNSS-R measurements, with significant skill improvements over a state-of-the-art model. Among its many uses, it sheds light on factors that can improve GNSS-R remote sensing of ocean surface windspeed. The results presented herein are applicable to L-band bistatic sensing techniques in general, including those leveraging reflectometry of communication signals of opportunity.

Chapter 1

Background and Theory

Since the 1960s, microwave remote sensing has provided observations of the Earth unprecedented in resolution and coverage. These observations have been critical not only to the operational monitoring of our planet, but also to significant advances in the understanding of a wide range of physical phenomena. However, remote sensing itself requires a detailed understanding of the physical processes inherent to the technique in question – this, in fact, is the objective of study for many in the sensing community.

In this thesis, our focus is on the properties of surface wave processes relevant to remote sensing. The motivation behind this dissertation, and its primary domain of application, lies in the remote sensing technique of GNSS-R (Global Navigation Satellite System Reflectometry). We examine topics on surface waves and their interaction with electromagnetic waves and wind in the context of wind sensing capability of GNSS-R.

The need for ocean surface winds is well-known; many atmospheric and marine processes depend on near-surface winds on the first-order. For instance, wind is primary source of energy input in the generation ocean waves, and wind products are used solely, at the time of writing, to drive operational wave models, providing forecasts of marine weather in the United States [Tolman, 2014]. Determination of heat, momentum, and mass fluxes over the ocean also requires knowledge of surface winds [e.g., Smith, 1988, Atlas et al., 2011]. These fluxes are critical for weather predictions over land as well as climatological forecasts.

Results in this work can be applied to other sensing techniques based on L-band quasi-specular scattering (discussed in Section 1.5), such as those leveraging communication signals of opportunity (SoOP). In addition, they are useful in the study of fundamental mechanics of surface waves, of which much has yet to be understood.

1.1 Remote Sensing of Ocean Surface Winds

To date, airborne and spaceborne remote sensing techniques of surface winds have *only* been developed over water bodies – no such technique is yet available for land surface wind measurements, although, ground-based Doppler profilers have been developed and used operationally to remotely sense the wind profile in the atmospheric boundary layer over land. For ocean, the primary emission and scattering elements on the surface are water waves, which are absent over land and ice.

The passive radiometry approach to the sensing of ocean winds depends fundamentally on changes in the thermal emission of the surface. For a beam-filling, semi-infinite homogeneous medium, undulations of the surface, or roughness, causes only minor changes in its emission characteristics. Breaking of surface waves entrains air into the waves and results in foam, a material that is electrically different from salty water and thus has a different emissivity [e.g., Wilheit 1979] – much higher, in fact, because it presents a better match in intrinsic impedance to air. Thus, it is the presence of foam, or fraction of foam coverage specifically, that is sensed in radiometric methods. Both wind speed and direction can be retrieved [e.g., Yueh et al., 1994; Li and Chang, 1996].

A second technique actively transmits a radar pulse and measures the backscatter from the sea surface. The dominant contributor to the return signal in this monostatic (collocated transmitter and receiver) approach results from a process known as Bragg-scattering, whereby periodic roughness elements with spacings consistent with the observation wavelength (modified by incidence angle dependencies) generate return pulses that add constructively [e.g., Ulaby et al., 1986; Apel, 1994]. These radars (see Section 1.6) typically operate in the C and Ku bands (e.g. QuikSCAT [Yueh et al., 2003] with a frequency of 13.4 GHz or 2.24 cm in wavelength), which corresponds to centimeter-scale capillary waves. Active instruments are more expensive in general than passive radiometric instruments, as extra power is needed for pulse transmission, resulting in larger solar panels, heavier satellite, costlier launch methods, not to mention the extra RF instrumentation required.

In both of the above techniques, at the frequencies commonly used in the past, the physical surface features sensed are highly coupled to the local winds: foaming due to micro-breaking and Bragg-scattering capillary waves respond quickly to the local winds. Surface tension plays a significant role in the governing equations for these centimeter waves. They grow almost instantaneously in response to winds and also dissipate quickly when the winds die down, or as they propagate away from their source of generation.

However, this is not the case for the relatively young remote sensing technique of GNSS-R [e.g., Komjathy et al., 2000; Gleason et al., 2009]. GNSS-R is most sensitive to gravity-capillary waves with wavelengths on the order of tens of centimeters. For these waves, the degree of coupling of wind and waves is less well known [e.g., Vos van Steenwijk et al., 2010; Cardellach et al., 2014]. GNSS-R has three important features for our discussion: 1) bistatic geometry, meaning the transmitter and receiver are not the same satellite nor are they collocated, 2) operation at microwave L-band (1-2 GHz) frequencies, and 3) use of GNSS signals.

As will be discussed further in Section 1.5, factors 1) and 2) determine the surface waves' wavelengths sensed by GNSS-R (and hence provides the raison d'être for this dissertation). Despite the issues in wind-wave coupling, there are several significant benefits of GNSS-R over the previous two techniques stemming from these three factors. These benefits have led to significant funding and development of many facets of the GNSS-R technique in the recent past, including theoretical modeling [e.g., Zavorotny and Voronovich, 2000; Lin and Katzberg 1999], instrumentation [e.g., Gleason et al., 2016], and retrieval algorithms [e.g., Clarizia et al., 2014].

Firstly, L-band operation allows signals to penetrate precipitation. This is especially advantageous for tropical cyclone conditions – incidentally, hurricane winds are also structured [e.g. Willoughby and Rahn, 2004] and high-speed, which causes the wind-wave decorrelation mentioned previously to be not as pronounced. The wind and waves in hurricanes have, in fact, been found to obey certain growth laws very well [Hwang, 2016]. Secondly, many GNSS systems are already in operation, and thus do not contribute to the cost of GNSS-R infrastructure. In the United States, the Global Positioning System (GPS) is the main GNSS system, and finds many civilian geolocation and navigation applications. They can be received anywhere on Earth (land or sea, as no cell phone tower required) with guaranteed levels of service. End-user receivers are ubiquitous in navigation and mobile devices. The availability of GPS has enabled explosive growth in location-based services and entertainment, including games such as Ingress and Pokémon GO on mobile platforms. The "reduction" in cost for GNSS-R is not just in the transmitting space segment – market incentives have spurred commercial development of high-performance GPS receivers with low power and low cost – granted, some modifications would be beneficial for GNSS-R, like removing floating gain control, for example (also mentioned in Chapter 3.) Thirdly and lastly, the fact that the signals leveraged by GNSS-R are used for navigation is also beneficial for remote sensing signal processing. The GPS transmitter satellites have crystal clocks which are tuned very accurately, taking relativistic effects into account, with uncertainties on the order of tens of nanoseconds. GPS is set up such that the code sent by the GPS transmitters can be replicated by the receiver with high fidelity. Having this reference signal is critical to the operation of the cross-correlation receiver, identifying the delay in the received signal necessary for the construction of the Delay Doppler Maps (DDMs) discussed in Section 1.5.

1.2 Ocean Surface Waves

The total ocean wave field at a given location consists of waves of various scales. The wind-generated waves have periods of less than about 30 s. They can be further divided into capillary waves and gravity waves. Gravity waves can in turn, but loosely, classified as wind sea (short, locally-generated waves closely coupled to the wind) or swells (long waves that originated as wind waves elsewhere). The distinction between the wind sea and swell is seldom clear-cut (see Section 2.4). In Table 1 below, we summarize the nomenclature used in the surface wave community for waves of various length scales [Munk, 1950; Holthuijsen, 2007]; note the ranges indicated are necessarily approximate.

Table 1: Surface wave length scales

Name	Period	Wavelength
Capillary waves	< 0.25 s	< 10 cm
Gravity waves: Swell and wind sea	0.25 s - 30 s	0.1 – 1500 m (deep water)
Infra-gravity waves	30 s – 5 min.	1500 m to 100 km
Tsunamis, surges, tides	> 5 min.	> 100 km

The wave scales relevant to GNSS-R are discussed rigorously in Sections 1.3 and 1.5.

In this thesis, the only waves sensed by and relevant to GNSS-R fall under wind-generated waves, and gravity waves in particular (Sections 1.3 and 1.5). The growth of wind sea alone depends on many factors other than the local windspeed, such as wind duration, fetch, atmospheric stability, internal waves, currents, water depth, and presence of surfactants such as oil. Fetch at a location is the distance upwind of the location over which a uniform wind has been blowing [e.g., Hwang and Wang 2004 JPO]. The decay of wind waves, on the other hand, has not received as much attention in the wave community, but is equally important to GNSS-R wind sensing.

Waves are often described statistically. When using and deriving these statistics from measurements, it is assumed that the wave processes are stationary, in a small time interval around some time instant of interest, and some small distance away from the location of interest. To emphasize the main concepts, let us use a simple model for the surface elevation at some arbitrary location. It can be assumed to be a one-dimensional zero-mean stationary random process denoted by $\zeta'(t)$ with SI unit of meters. Its univariate auto-correlation function is defined by

$$R_{\zeta'}(\tau) \triangleq < \zeta'(t+\tau)\zeta'(t) >, \tag{1.1}$$

where $<.>$ is the ensemble mean operator. Let $S'(f)$ be the Fourier transform of $R_{\zeta}(\tau)$; the SI unit of $S'(f)$ is m^2/Hz. It can then be shown that

$$< \zeta'(t)^2 > = R_{\zeta'}(0) = \int_{-\infty}^{\infty} S'(f)\,df. \tag{1.2}$$

Note all three (equal) quantities are not functions of time but single-number characterizations of $\zeta'(t)$, a consequence of the stationary assumption. This quantity is appropriately termed as the mean square elevation. $S'(f)$ is also known as the power spectral density (PSD) of $\zeta'(t)$, because $S'(f)$ has the interpretation of elevation variance per frequency at f. In literature, $S'(f)$ is also referred to as elevation variance frequency spectrum, spectral wave density [NDBC, 2015b], omnidirectional spectrum [Elfouhaily et al., 1997], or simply wave spectrum [Stewart, 2008]. It turns out that elevation variance and wave energy are intimately related. In particular, the total potential and kinetic energy per unit area, E_{total} can be expressed as

$$E_{total} = \rho g < \zeta'(t)^2 > \ , \tag{1.3}$$

where ρ is the mass density of sea water and g is the gravitational constant. C

Correspondingly, we can define the wave energy frequency spectrum $S_e(f)$ such that

$$E_{total} = \int_{-\infty}^{\infty} S_e'(f)\,df \ . \tag{1.4}$$

Equating the right sides of (1.3) and (1.4), and using the last equality of (1.2), we see

$$S_e'(f) = \rho g S'(f) \ , \tag{1.5}$$

which is reason that $S'(f)$ is sometimes loosely referred to as the wave energy density.

For remote sensing, we are often interested in slope and curvature. Similar to the above development, we can define a one-dimensional random process as a function of position x, for a given instant of time. The elevation variance wavenumber spectrum is then analogously defined as

$$S(k) \triangleq \mathfrak{F}[<\zeta(x+u)\zeta(x)>],$$

where $\mathfrak{F}[.]$ is the Fourier Transform operator, and k is the wavenumber. The elevation variance over a specific band is fixed, so that $S(k)dk = S(f)df$.

For linear waves in deep water, the following dispersion relation holds. Letting $\omega \triangleq 2\pi f$ be the angular frequency,

$$\omega^2 = gk \ .$$

It can then be shown

$$S(k) = \frac{g}{8\pi^2 f} S(f) \ ,$$

with k and f related per the dispersion relation above. This equation allows us to convert between the frequency spectrum, which is measured by buoy accelerometers, and the wavenumber spectrum, which is of more relevance to remote sensing.

The wave slope is defined as

$$s \triangleq \frac{d\zeta(x)}{dx}$$

in the context of our one-dimensional wave. Note that like ζ, $<s>=0$. The mean square slope is then defined as

$$mss \triangleq <s^2> \ .$$

It can be shown that the slope variance wavenumber spectrum is equal to $k^2 S(k)$, so that

$$mss = \int_{-\infty}^{\infty} k^2 S(k)\, dk. \tag{1.6}$$

The factor k arises due to the differentiation of a sinusoid, and the second power is due to the fact of it being a variance spectrum. Since mss is unitless, $S(k)$ has units of m^3, which we also expect from the units of $S(f)$ by duality.

Extending this definition, the one-dimensional curvature or dimensionless spectrum is defined as $k^3 S(k)$.

For the discussion in this thesis, and a later simplifying assumption made on seas being isotropic (Chapter 3), we will not need to use two-dimensional wave spectra. However, a discussion is included in Appendix A for the interested reader.

An example of the elevation wavenumber spectrum is shown in Figure 1. The wave spectra plotted are due to Elfouhaily et al. [1997], which is a strong function of U_{10} (the windspeed at 10 m height).

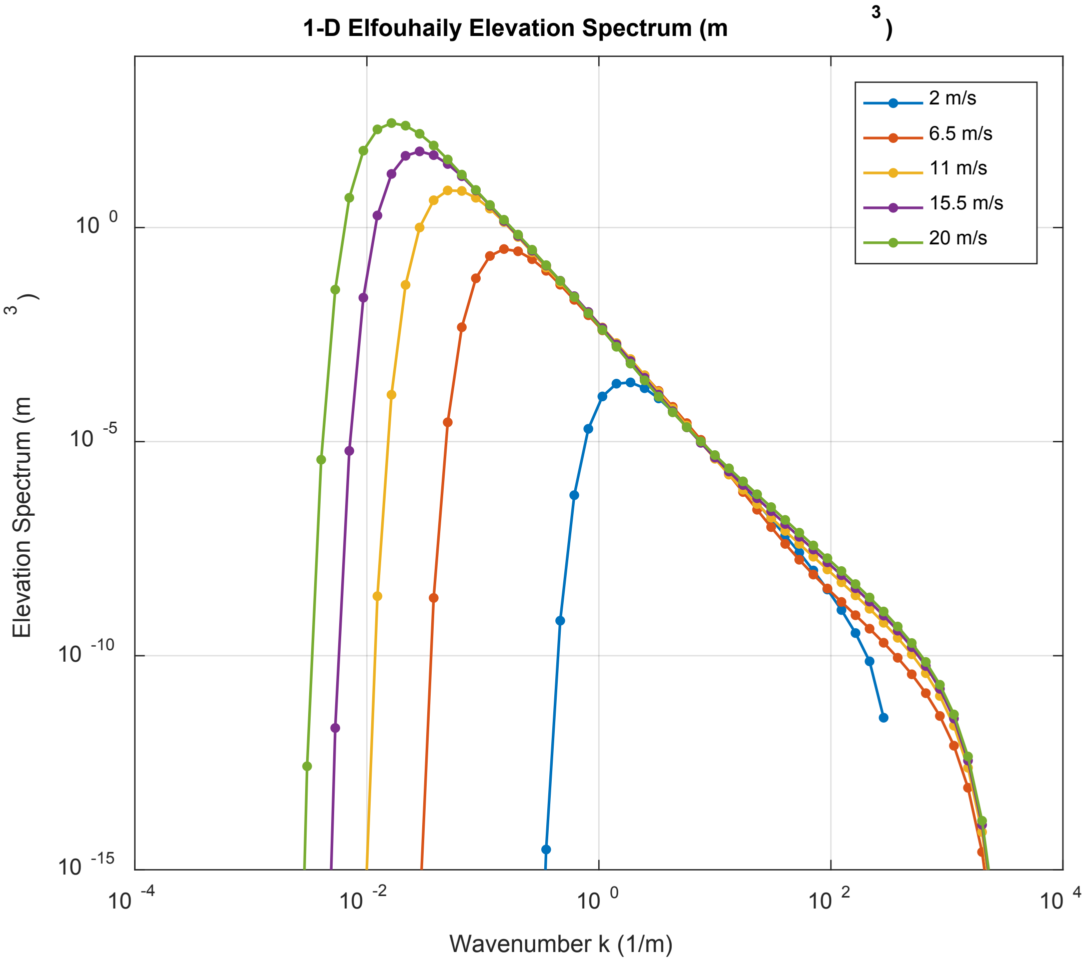

Figure 1: Examples of elevation wavenumber spectra. The Elfouhaily model is used, for well-developed conditions. The maximum of a spectrum is known as the spectral peak.

1.3 Surface Wave Models

For phase-averaging surface wave models, one important goal is to quantify the spectral energy accurately in the form of a wave spectrum, which can range from a one-dimensional directionally-integrated spectrum in the simplest case to a full three-dimensional frequency-wavenumber-direction spectrum for nonlinear waves. These models can generally be divided into two types: 1. empirical models based on dimensional analysis and parameterized by wind speed and, possibly, wave age (stage of wave development dependent on duration and fetch), and 2. spectral evolution models based on the energy-balance equation.

The first type typically constrains the shape of the spectrum, which is usually a smooth function of the input parameters. Often, conditions are classified as duration- or fetch-limited [Hwang and Wang, 2004], and the wave age is computed accordingly. The wave age and windspeed are then used to parameterize the wave spectrum. The Pierson-Muskowitz [Pierson and Moskowitz, 1964], JONSWAP [Hasselmann et al., 1973], Elfouhaily [Elfouhaily et al., 1997], and Hwang [Hwang et al., 2013] spectra are of this type. The second type of model includes WAVEWATCH3 [Tolman et al., 2014] (denoted by WW3 hereafter), University of Miami Wave Model [Donelan et al., 2012], SWAN [Booij et al., 1999], and WAM [Komen et al., 1994]. These models solve the energy balance equation numerically. A Eulerian form of this equation in simple cases (conditions given below) may be expressed as

$$\frac{\partial E(k,x,t)}{\partial t} + c_g \frac{\partial E(k,x,t)}{\partial x} = ST(k,x,t) \ , \tag{1.7}$$

where E is the one-dimensional wavenumber-direction spectrum with SI units of m^3, with the wavenumber energy spectrum being $\rho g E$ with units of J/m. ρ is the mass density of sea water, and g is the gravitational constant. c_g is the group velocity in the x direction. $ST(k,x,t)$ is the collective source term combining the effects of wind input, whitecapping dissipation, and non-linear wave-wave interaction. Equation (1.7) models the temporal evolution and spatial propagation of the elevation variance of a one-dimensional wave in deep water and neglects the effects of currents. In practice, an equation of this type is discretized and integrated in time and space to solve for the wave spectrum at each time step and grid point. The source terms, with improved understanding of wave physics, have undergone significant development in the last 50 years, and are now in their "3rd generation" [Komen et al., 1994].

For the second type of wave model, rather than having an a-priori form, the individual source terms are crafted, and the spectrum is left free to evolve. Before the 1950s, models of the first kind were used for wave forecasting. However, several aspects are challenging for the parametric models to handle, such as the accounting for swell generated afar, and irregular bathymetry and coastlines [Ardhuin, 2016 p.52]. In addition, Chen et al. [2016] found that two such empirical models show significant errors in modelling the response time of waves to wind in general conditions, while later investigations showed the third-generation model WW3 performs significantly better in comparisons with in-situ measurements.

Despite its shortcomings, the parametric models and the associated experiments that led to them are widely used when modelling idealized duration and fetched-limited cases of wave growth (before the wave becomes "fully-developed" with the wind forcing). These ideal cases have been invaluable in the development of the spectral-evolution models' source terms, and they continue to serve as reference calibration points for the state-of-the-art third-generation models. Moreover, these parametric models are considered the current state-of-the-art models for high frequency waves. The form and shape of the spectral tail assumed in the models is still an area of active research [Ex. Plant, 2015, Reichl et al., 2015, Hwang et al., 2013], partly due to the challenges in their accurate measurement [Hwang, 2005]. Many electromagnetic models to-date have incorporated these parametric models [e.g., Voronovich and Zavorotny, 2001; Apel, 1994; Hwang and Fois, 2015] as the surface wave model, with the inverse wave age often set to 0.84 for "well-developed" conditions. It should be noted that formulations of source term balance of short Bragg waves have been attempted [e.g. Lyzenga et al., 1988], but much uncertainty remain [Hwang et al., 2013].

As we will see in Section 1.5, the GNSS-R forward scatter can be modelled as quasi-specular incoherent scatter in most conditions. This scattering mechanism is dependent on the long, tilting waves under the two-scale electromagnetic formulation. So, for GNSS-R, the surface roughness of relevance is the low-pass-filtered mean square slope (mss)

$$LP_{mss}\left(k_u\right) \triangleq \int_0^{k_u} k^2 S\left(k\right) dk \quad , \tag{1.8}$$

where k_u is known as the scale-dividing parameter, and sets an effective upper limit on the frequency of waves GNSS-R is sensitive to. It is this parameter that makes precise the otherwise ambiguous usage of "long waves" and "short waves". Under the two-scale model, surface features are divided into two scales based on their size: the short Bragg waves and the long tilting waves. Just as division of roughness features into two distinct regimes is somewhat arbitrary, so is the dividing parameter itself. However, once the parameter is chosen, it applies equally well for both the short, Bragg regime, and the long tilting regime.

An empirical value of k_u corresponding to 3λ was suggested by Brown [1978], with λ being the electromagnetic wavelength. Even though this parameter was introduced as the lower frequency limit for backscattering, it also sets the upper frequency limit for forward, quasi-specular scatter, and its use is implied in the thorough treatment of Brown [1990]. More recently, Garrison et al. [2002] extended the "three-lambda" criterion to take into account the dependence on incidence angle, resulting in

$$k_u = \frac{2\pi \cos\theta}{3\lambda} , \tag{1.9}$$

where θ is the incidence angle of the measurement. For the GPS L1 carrier with a frequency of 1.575 GHz, and typical incidence angles of less than 35 degrees, $k_u \approx 10$ rad/m, so waves of about 60 cm and longer are sensed by GNSS-R.

In 2005, this dividing parameter was further studied by Thompson et al. [2005], who developed a parameter that was dependent on U_{10}. In 2015, Zavorotny et al. [2016] used a more accurate (but more computationally expensive) scattering model, known as the Small Slope Approximation (SSA) model, to evaluate the effects of the dividing parameter. The Elfouhaily et al. [1997] wave spectra is used assuming fully-developed conditions. They found no significant differences in using the two dividing parameters of Garrison [2002] and Thompson [2005], and the results also agree reasonably with the Katzberg et al. [2013] model developed from observations. For the modelling work in this thesis, Chapter 4, we are concerned with first-order effects, so we select the cutoff parameter suggested by Garrison [2002] in Equation (1.9).

We mention in passing that the quantity significant wave height, usually denoted as Hs and used in our analysis in Chapter 4, can be computed from the wavenumber spectrum as

$$Hs = 4\sqrt{\int_0^\infty S(k)\,dk}\ . \tag{1.10}$$

Once the wave spectrum is known, LP_{mss} can be readily calculated. Katzberg et al. [2013] developed a semi-empirical, one-to-one relationship between windspeed and mean squared slope by fitting data provided by airborne GNSS-R experiments and an adjusted high resolution windspeed model. The Katzberg model is even simpler than the parametric wave models because it does not involve the wave spectrum. This relationship is expressed as follows

$$\begin{aligned}
&LP_{mss} = 0.45(0.00316 f(U_{10}) + 0.00192 f(U_{10}) + 0.003) \\
&f(U_{10}) = U_{10}, \qquad\qquad 0 < U_{10} < 3.49\ m/s \\
&f(U_{10}) = 6\ln(U_{10}) - 4, \quad 3.49 < U_{10} < 46 \\
&f(U_{10}) = 0.411 U_{10}, \qquad 46 < U_{10}
\end{aligned} \quad , \tag{1.11}$$

where U_{10} is the windspeed at 10 m height. The Katzberg relationship is plotted in Figure.

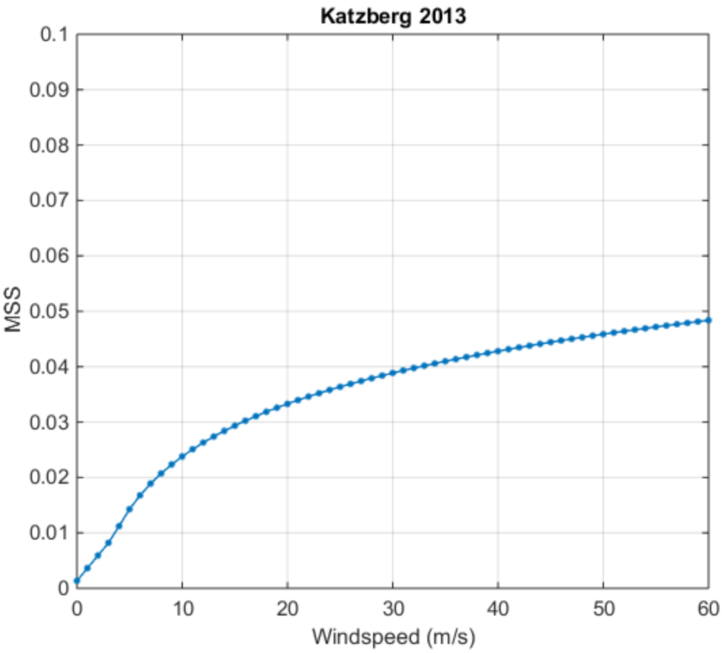

Figure 2: Katzberg 2013's empirical mss vs. windspeed relationship.

The end-to-end forward model/simulator for CYGNSS [Ruf et al., 2016a], considered to be the state-of-the-art, ingests windspeed and generates the delay-Doppler-map. It currently uses the Katzberg relationship.

According to the Elfouhaily spectra shown in Figure 3, the long waves contribute a considerable portion of the LP_{mss} sensitivity to wind. Such characteristics are similar to other spectra [e.g., Fig. 6 of Apel, 1994].

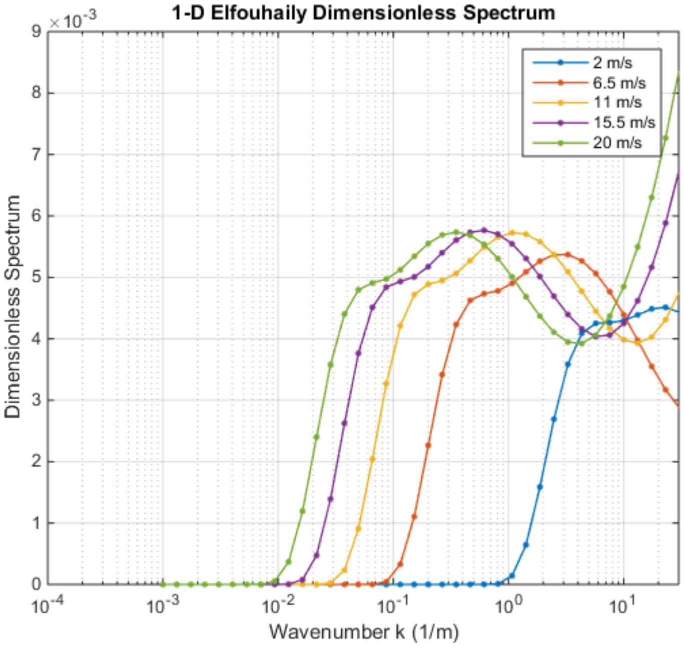

Figure 3: Elfouhaily slope spectrum in area-conservative form. The relevant portion for GNSS-R is about 10 rad/m and below.

As noted above, the inclusion of a third-generation model, which focuses on the energy-containing long waves, has not been of importance for other sensing techniques. Whether a model would benefit GNSS-R is a question we explore in Chapters 3 and 4. As third-generation wave models have demonstrated considerable skill in forecasting wave properties dominated by the energy-containing waves near the spectral peak (such as significant wave height and peak period) [e.g., The WAMDI Group, 1988; Ardhuin et al. 2010; Chu et al., 2004], we make use of this type of model in our work. In particular, in Chapters 3 and 4, we select WAVEWATCH III ® (WW3) as the low-frequency wave model, which is run operationally by the National Weather Service (NWS). The source terms of WW3 include wind input, dissipation, non-linear interaction, bottom friction, ice scattering, among others.

1.4 The Need for the Spectral Tail

Third-generation wave models do not explicitly resolve high frequency and high wavenumber waves; one reason is that the source terms have yet to be resolved with reasonable certainty. For GNSS-R, these unresolved waves constitute a sizable portion of the mean square slope, so to use the 3rd generation models, a high frequency tail needs to be attached.

Here, we briefly introduce a two-dimensional tail that was recently developed for WW3. Reichl et. al [2015] at University Rhode Island conducted a study of wind stress in hurricane conditions, and how it is affected by the sea state, using WW3. The wave spectrum modifications for the spectral tail used in that study, with the cutoff frequency adapted for GNSS-R, are summarized below.

1. Start with the stock WW3 spectrum.

2. For the frequency range below 1.5 times the peak frequency, the frequency corresponding to the maximum of the stock WW3 spectrum is kept.

3. From 1.5 times to 3 times the peak frequency, the curvature spectrum is linearly varied to a limiting value of 0.006 rad^2.

4. Above 3 times of the peak frequency, the saturation spectrum is kept constant at 0.006 rad^2 until the cutoff frequency (9.54 rad/m for CYGNSS).

5. MSS is computed diagnostically by integrating the modified spectrum.

The code segment implementing these modifications was received from Reichl et. al, and this was then integrated into the latest WW3 model, version 4.18, at the University of

Michigan by Chen (the author) et al. The Tolman-Chalikov [Tolman] source terms are used to model the base, stock spectrum. Hurricane Ivan, a Category 5 storm from the 2004 Atlantic hurricane season, is used as a test case. The time series of input wind vector fields are H*WIND product obtained from [NOAA]. The model is ran for 60 hours of simulation time (starting from 20040913 133000 and ending at 20040916 000000). A spatial MSS field is then generated by WW3 at regular time intervals. A sample snapshot of the wind speed input nearing landfall is shown in Figure 4.

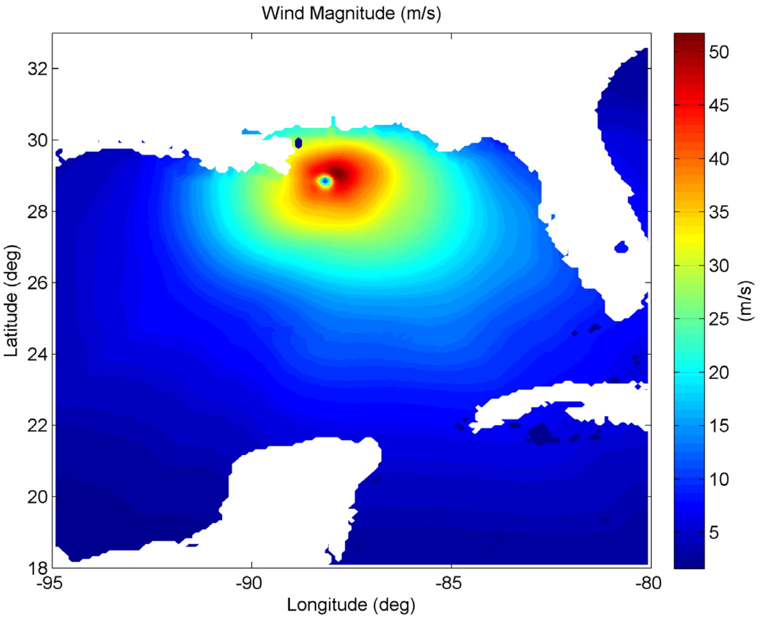

Figure 4: Windspeed snapshot at 20040916 00:00

By matching each value of MSS with the magnitude of input windspeed geographically, a total MSS vs. local windspeed scatter plot can be generated. This is shown in Figure 5 below for the snapshot at Sep. 16, 2004 00:00 (simulation end time).

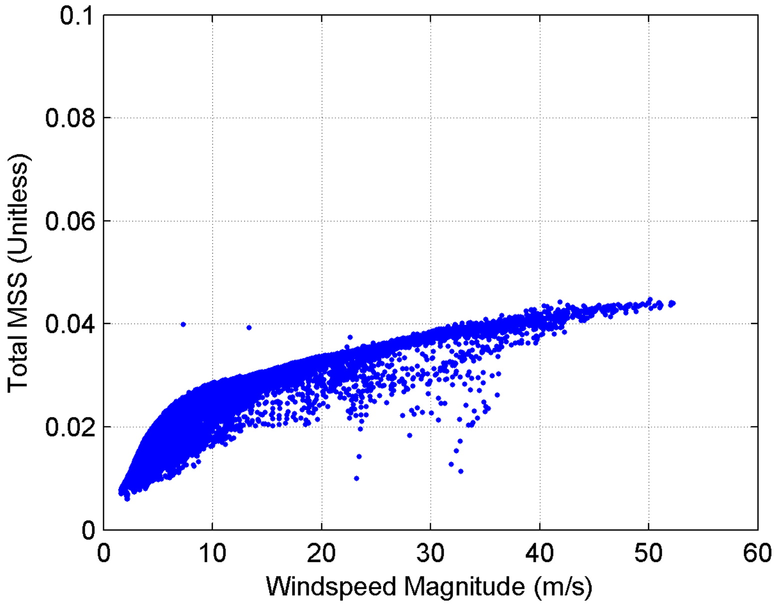

Figure 5: Total MSS vs. windspeed with modified spectral tail at 2004 09 16 00:00:00 for Hurricane Ivan

It is seen that this MSS-windspeed relationship indeed follows the behavior shown in the Katzberg relationship qualitatively. However, there is still some scatter, which represents the errors in the retrieval of the windspeed if a one-to-one wind-mss relationship is used. An effort aimed at making this relationship more precise and more amenable to inversion by leveraging the knowledge of other ancillary parameters is an area of ongoing research, with some discussion included in Chapter 5.

1.5 Electromagnetic Scattering and Signal Processing

The bistatic geometry for GNSS-R is shown in Figure 6 below. In the case of GPS, the receiver would have direct line-of-sight contacts with at least 4 GPS transmitters (just like any other GPS receiver). Direct signal acquisition is currently required for all known GPS-R sensing instruments.

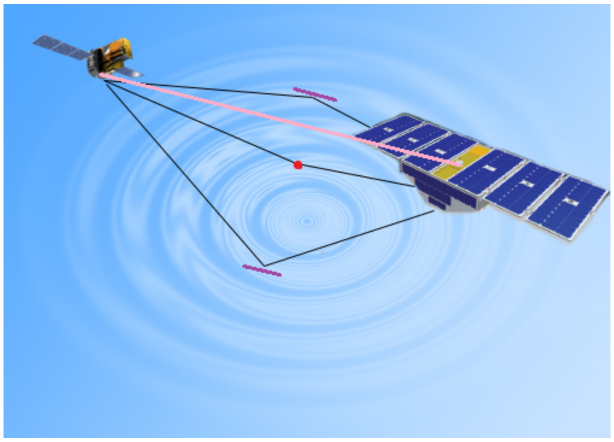

Figure 6: Scattering geometry for a receiver (with blue panels) and one transmitter satellite. The black lines are select rays of incident and scattered waves. The red dot denotes the specular point. The purple lines denote the favorable orientation ("slope") of the local facet that results in reflection toward the receiver in a geometrical optics (GO) formulation. The pink line denotes the direct signal, required for present GNSS-R sensors.

The direct signal, shown in pink above, is needed because the orbit ephemeris and PRN (pseudo-random noise) codes of the GPS constellation are not stored by the receivers. Thus, the only way to know the precise location of the receiver, transmitters, and the transmitter PRN codes is to compute them based on information gathered from the transmitters. Four pieces of information are needed to determine the scattering geometry: transmitter position, transmitter velocity vector, receiver position, and receiver velocity vector. The velocities are needed to compute the Doppler shift of the GPS signals, explained later.

The specular point for a given geometry is the unique location on Earth's surface for which the sum of distance to the transmitter and distance to the receiver is minimum. When the surface becomes rough, points other than the specular point can scatter the incident signal to the receiver as well.

The Doppler shift in the signal returns is caused by the relative motion of the transmitter, sea surface, and the receiver. Each point on the surface, due to possibly different scattering geometries, are associated with different Doppler shifts. This frequency shift can be detected by the receiver with appropriate filters. Combined with delay τ (output by the cross-correlation receiver), this allows us to create 2-dimensional plot of the received power as a function of delay τ and Doppler frequency shift. This plot is known as the Delay-Doppler Map (DDM). Figure 7 shows an example of a DDM, which is a simulation of a TDS-1 (see Chapter 4) measurement geometry with an input wind of 6.1 m/s.

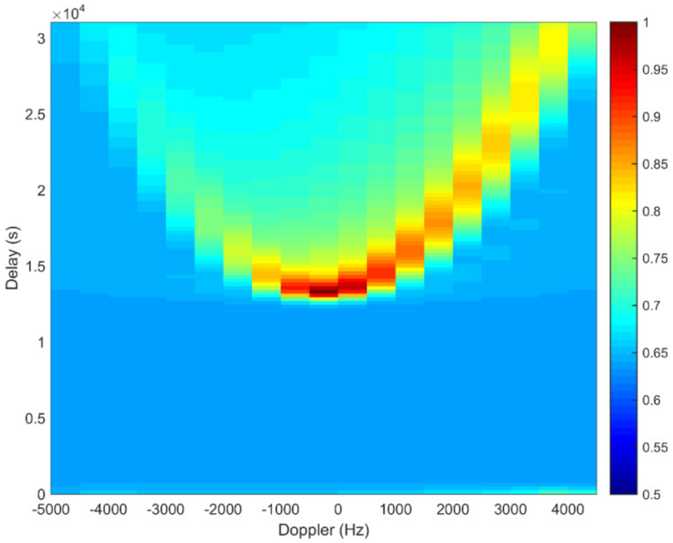

Figure 7: Example DDM. This DDM has been normalized by the peak power.

The ZV model developed by Zavorotny and Vornovich [2000] is a widely used scattering and signal processing model for the GNSS-R received signal. Because the ZV model connects the wave model and the GNSS-R observables and is pertinent to our signal processing methods used later, we discuss it here in some detail. The ZV model applies the theory of quasi-specular electromagnetic scattering from rough surfaces to GPS L1 signals.

This theory has been treated in detail in numerous works, such as Bass and Fuks [1979], Barrick [1968], Beckmann and Spizzichino [1987], Brown [1990], Valenzuela [1978], and Ulaby et al. [1982] Chapter 12. This model is based on the Kirchoff Approximation's Geometrical Optics limit (KA-GO), which yields a simple form for the normalized radar cross section. However, it should be noted that only the incoherent component is modelled. Thus, the surface must be sufficiently rough to ensure a large Rayleigh parameter, and the incidence angle must be far from grazing. In practice, this equates to winds higher than about 3 m/s and an incidence angle smaller than 70 degrees.

Under the ZV model, the signal power intercepted by the receiver antenna is expressed as

$$P_s(\tau,f) = CP_t \iint \frac{G_t G_{rant}}{R_t^2 R_r^{\ 2}} \chi^2(\Delta\tau,\Delta f)\sigma_0(\vec{s})dA \ . \tag{1.12}$$

The surface integral is performed over an area large enough for the desired τ and f ranges, and is known as the glistening zone. For us, τ ranges over about 30 us and f ranges over about 10 kHz. The glistening zone is chosen to be 200 km by 200 km centered at the specular point, which is sufficient for most scattering geometries of the TDS-1 instrument considered in Chapter 4.

$\Delta\tau = |\tau_g - \tau|$, with τ_g being the delay associated with the location of the differential surface element, dA. $\tau_g = (R_t + R_r)/c$ and for a given geometry, it is a constant for a given surface location, independent of $\tau \text{ and} f$. Similarly, $\Delta f = f_g - f$, and $f_g = -f_{CW}(\overrightarrow{u_R}\cdot\overrightarrow{v_R} + \overrightarrow{u_T}\cdot\overrightarrow{v_T})/c$. f_{CW} is the frequency of the carrier wave; for GPS L1, it is 1.575 GHz. $\overrightarrow{u_R}$ is the unit vector from the specular point to the receiver, $\overrightarrow{v_R}$ is the receiver velocity vector, $\overrightarrow{u_T}$ is the unit vector from the specular point to the transmitter, and $\overrightarrow{v_T}$ is the transmitter velocity vector.

$P_s(\tau, f)$ is the signal power for delay τ and frequency f. C is a constant that depends on the electromagnetic wavelength and coherent integration period of the receiver. P_t is the GPS transmitter power and is assumed to be constant, as is G_t, the product of transmitter antenna and instrument gains. G_{rant} is the receiver antenna gain. R_t , R_r are the distances from the dummy integration position on the grid to the transmitter and receiver, respectively. χ is dependent on the signal modulation and coding, and it is the product of a triangle and a sinc function. $\chi^2(\Delta\tau, \Delta f)$ is commonly known as the ambiguity function and models the selectivity of the radar system. Letting τ_0 and f_0 be the delay and Doppler shift corresponding to the specular point, respectively, if the selectivity is sufficiently high such that $\frac{G_t G_{rant}}{R_t^2 R_r^{\ 2}} \sigma_0$ is constant for some small area ΔA around the specular point, then, because $\chi^2(0,0) = 1$,

$$P_{s0} \triangleq P_s(\tau_0, f_0) = CP_t \frac{G_t G_{rant}}{R_t^2 R_r^{\ 2}} \sigma_0 \Delta A \ . \tag{1.13}$$

This equation is useful for our later work in Section 3.3.

Similar to τ_g , f_g , G_t, G_{rant}, R_t , and R_r, $\vec{s}$ is also a constant for a given location (independent of τ, f) – it specifies the favorable orientation (two perpendicular slope components) of a facet that reflects the incident ray toward the receiver. The scattering cross section $\sigma_0(\vec{s})$ is where the surface roughness enters; it is proportional to the PDF of slopes as well as the square of the Fresnel surface reflectivity:

$$\sigma_0 = \frac{\pi \,|\, \Re \,|^2 |\, \hat{q} \,|^4}{{q_z}^4} P(\vec{s}) \ , \tag{1.14}$$

where $\Re$ is the Fresnel reflection coefficient dependent on medium properties such as sea-surface temperature and salinity; $\hat{q}$ is the plane-normal unit vector to a facet of favorable orientation. More precisely, if we let $\hat{n}$ be the unit vector of scattered wave (from surface point to receiver), and $\hat{m}$ be the unit vector of the incident wave (from transmitter to surface point), then $\hat{q} = \hat{n} - \hat{m}$. q_z is the vertical component of the $\hat{q}$.

The PDF of slopes, $P(\vec{s})$, is where the surface roughness dependence is introduced. For a two-dimensional Gaussian PDF, $P(\vec{s})$ can be completely parameterized by the upwind and crosswind slope variances, which are equal to the mean-square-slope components. It should be remembered that the variances or mean square slopes of $P(\vec{s})$ must be sufficiently large for the ZV model to remain valid. If the surface is calm, an additional coherent component becomes significant, and should be taken into account. Such a scattering model accounting for both components are currently under development for GNSS-R [personal communication, Zavorotny, 2016].

1.6 Survey of Spaceborne Ocean Surface Wind Missions

A partial but representative list of vector wind missions in the past and undergoing development is presented in Table 2.

Table 2: Selected ocean surface wind missions.

Name (Instrument); Agency	Spatial Resolution (km)	Operating Frequency (GHz)	Period in Service
SEASAT (SASS); NASA	50	14.6	June 1978 to Oct. 1978
ERS-1 (AMI); ESA	50	5.3	July 1991 to June 1996
QuikSCAT (SeaWinds-1); NASA	25	13.4	Jan. 2003 to -
Coriolis (WindSat); US Navy	25	6.8, 10.7, 18.7, 23.8 and 37.0	Jan. 2003 to -
METOP-B (ASCAT-B); ESA	50	5.255	Sept 2012 to -
CYGNSS	25	1.575 GHz	Nov. 2016 to -

Sources: Martin [2014]; Remote Sensing Systems [2016]; COAPS FSU [2016]

Of the list above, only WindSat is a passive sensor. With several frequencies, it can also retrieve Sea Surface Temperature (SST). All known scatterometers (including those not the representative list) operate in the C or Ku bands. This is because the atmospheric transmissivity is very high in those two bands. Scatterometers and radiometers are capable of sensing both the wind speed and wind direction. Scatterometers employ a variety of pulse shaping and signal processing techniques to reduce effects of clutter and improve spatial resolution, including range binning and Doppler binning. At oblique angles of incidence, surface points closer the radar have a smaller delay times than those further away. This physical mechanism allows the separation of surface features to improve spatial resolution. A similar frequency filter is used in the receiver to achieve Doppler binning. On the other hand, the spatial resolution of passive radiometers is dictated by the antenna footprint.

GNSS-R instruments uses similar delay and Doppler binning techniques. However, it should be noted that CYGNSS currently uses only pixels near the specular point as its baseline retrieval algorithm. Theoretically, however, pixels in other areas of the DDM can be used to retrieve winds elsewhere. A similar technique is being explored by Garrison et al. via a Kalman-filtering approach.

For CYGNSS, it also has unprecedented coverage, deploying 8 observatories that are each capable of making up to 4 measurements simultaneously. Figure 8 shows the QuikSCAT satellite being tested in a thermal vacuum chamber before launch. Figure 9 shows several CYGNSS observatories undergoing the same test. As can be seen, the GNSS-R technique allows much smaller satellites to be used.

Figure 8: QuickSCAT undergoing tests in a thermal vaccuum chamber. Source: https://directory.eoportal.org/web/eoportal/satellite-missions/q/quikscat

Figure 9 CYGNSS observatories undergoing tests in a thermal vaccuum chamber. Source: http://www.nasa.gov/press-release/nasa-invites-media-to-learn-about-new-hurricane-mission

CYGNSS also have a 25 km spatial resolution, but in addition to windspeed measurement at low winds, it will be adept at measuring tropical cyclone windspeeds, with less relative uncertainty. However, the ability of GNSS-R to measure wind direction is inconclusive at the time of writing.

1.7 Topics of the Thesis

Much of the efforts of the surface wave community have been devoted to the energy-containing long waves near the spectral peak. On the other hand, the ocean remote sensing community have spent considerable efforts on scattering from capillary waves. As a result, these “intermediate-scale” waves appropriate for GNSS-R have not received adequate attention. We present results on two wind-wave coupling studies for these “intermediate-scale” waves in subsequent chapters.

If we take windspeed as the input of a system and the surface waves as the output, it is clear such a system is not linear, owing to the complex non-linear processes involved. In Chapter 2, we try to determine the response time of this system empirically. The results of this study may find application in data assimilation of GNSS-R winds, for instance. Measurements using moored buoys are used, which, it turns out, are not capable of sensing all the waves relevant to GNSS-R. Nonetheless, we obtain concrete bounds and speculate results based on extrapolation. The surface wave models discussed previously are also compared and validated with these results.

In Chapter 3, we attempt to augment the state-of-the-art forward models for GNSS-R by taking non-local wind dependencies into account. We compare modelled results with recently collected spaceborne measurements in Chapter 4. The skill of our model are also compared with that of one of the best existing models.

Chapter 5 concludes the thesis, and provides detailed descriptions of future work.

Chapter 2

Temporal Response of MSS

In this section, we attempt to characterize the response time (defined later) of mean square slope sensed by GNSS-R. We are interested in the response time as it provides insight on questions like "does the measured winds correspond to the winds 10 minutes or 2 hours ago?", and the response time, if resolved satisfactorily, should be taken into account in assimilating GNSS-R measurements with atmospheric models.

2.1 Introduction

The evolution of ocean surface waves has been the subject of study for many decades. Much effort has been devoted to the study of two wave properties: wave height and peak frequency [e.g., Young, 1999; CERC, 1977]. Wave height is important to mariners, surfers, and coastal engineers. Peak frequency dictates the velocity of the dominant waves, and is therefore critical to the forecasting of the time of arrival of waves at the coast.

The bulk of past studies on the growth of these two quantities has focused on two ideal cases:

1. Temporal steady-state, in which a steady wind blows for a sufficiently long duration. The wave properties can then be described as a function of distance downwind. This case has been termed "fetch-limited" growth [e.g., Hasselmann et al., 1973].

2. Spatial steady-state, in which the winds are steady over a sufficiently large distance. The wave properties are then only a function of time. The wind forcing is considered to be a step function starting from calm conditions. This scenario is known as “duration-limited” growth [e.g., Hwang et al., 2004a].

In bistatic remote sensing and radar altimetry, the specular and quasi-specular reflection from large scale slopes is believed to be the dominant contributor to the measurement, and so the low-pass filtered mean square slope (defined in Chapter 1) is the quantity directly relatable to the radar cross section [Valenzuela, 1978; Zavorotny et al., 2000]. In both cases, measurements related to mss are assumed to be, indirectly, proxy measurements of the local winds. The response time of the mss to wind is, then, of fundamental importance to these techniques of ocean wind remote sensing.

Although there have been some studies of the mean square slope and the relevant portions of the wave spectrum, from modelling [e.g., Hwang et al., 2013], in-situ sensing [e.g., Hwang et al., 2004b], and remote sensing [e.g. Cox and Munk, 1954; Jackson et al. 1992] approaches, empirical research on the evolution of mss as a function of fetch or duration has remained scarce. In this paper, we study the temporal evolution of low pass filtered mss in a variety of field conditions over many years – specifically, measurements by 46 National Data Buoy Center (NDBC) buoys are analyzed. The dataset ranges from 2004 to 2014, inclusive.

2.2 Data Source and Processing

The NOAA NDBC operates and maintains moored buoys in the coastal U.S. regions. The 3 m, 6 m, and 10 m discus buoys are capable of measuring the wave frequency spectrum as well as many other environmental parameters such as wind speed, wind direction, air temperature, and sea surface temperature (SST). The majority of the buoys are of the 3 m discus type. The non-directional wave spectrum is derived from a time series of heave acceleration measurements collected by hull-fixed accelerometers [NDBC, 1996]. The frequency range of the waves sensible by the buoys is dictated by the dimensions of the buoys.

The wave spectra data typically range from 0.02 Hz to 0.485 Hz. For linear waves, this corresponds to 0.0016 rad/m to 0.95 rad/m in wavenumber, or about 4 km to 6.64 m in wavelength.

From the data, it is seen that most wind speeds range from 5 to 15 m/s. The wind speeds are measured at a height of 5 meters.

Most buoys acquire wave data for a duration of 20 minutes each hour, at 20 min. to 40 min. after the hour. These measurements are then averaged to derive the wave spectrum, which is reported at hourly intervals.

Not all measurements are taken continuously and simultaneously. A data product known as “continuous wind”, however, is measured continuously, and is averaged every 10 minutes. The first continuous wind measurement of the hour starts at minute 0 and ends at minute 10.

Meteorological data such as air temperature and SST are 8-minute averages, collected hourly from 42 to 50 minutes after the hour [NDBC, 2009b]. The air temperature is measured at a height of 4 meters.

NDBC historical data were accessed from [NDBC, 2015]. We take the time of each measurement to be at the center of the averaging period. For example, a wind measurement averaged from 10 to 20 min after the hour is taken to be the wind speed at 15 min after the hour. Likewise, the wave measurements made between 20 and 40 min after the hour are taken to be the sea state at 30 min after the hour. (It should be noted, however, that the reported timestamps in NDBC datasets are not at the center but vary by the type of measurement [NDBC, 2012a]; care is taken to interpret the timestamps correctly.) To synchronize the wind and wave data, both datasets are interpolated to 5 minute intervals. A spectrum-preserving sinc interpolator is used. For other meteorological data, only long term averages are needed for our analysis and so no interpolation is necessary.

Due to vandalism and possibly other issues (recovery and redeployment, for example) [Teng et al., 2010], the data sometime contain gaps. If the gap is less than 1.5 hours, data are filled in by interpolation. Otherwise, the data series is broken into chunks for processing. This is of relevance because our analysis techniques (see Sections 3.1 and 3.2) require a continuous series of data.

A list of buoys selected for use in this analysis, along with their relevant properties, can be found in Appendix A: Table of Buoy Stations and Their Properties. The distance to the nearest coast is obtained from NASA's Ocean Biology Processing Group dataset [NASA, 2009]. For bathymetry, the cell-registered version of ETOPO1 [Amante et al., 2009] is used.

Stations with any of the following characteristics are excluded from the analysis:

- Nonstandard wave acquisition times [NDBC, 2012b; NDBC, 2002],

- Anemometer not at the usual 5 m height, or the air temperature sensor not at the usual 4 m height [NDBC, 2009a],
- Location with ocean depth less than 193 m (see Section 2.2 for explanation), and
- Location less than 10 km from the coast.

Older spectral data, which do not range from the typical 0.02 Hz to 0.485 Hz, are also excluded.

2.3 Computation of Low-Pass Filtered Mean Square Slope

Because the mss is a spatial property, the one-dimensional frequency spectrum measured by buoys first needs to be converted to a wavenumber spectrum. The linear dispersion relation in deep water is invoked to perform this conversion. To ensure that the deep water approximation holds, we exclude buoys in shallow coastal waters, in which the behavior of waves is significantly more complicated [Donelan et al., 2012]. To compute a depth threshold, we first note that the wind speeds measured by buoys rarely exceed 20 m/s. From the fully-developed Elfouhaily spectrum [Elfouhaily et al., 1997] at 20 m/s, the dominant waves have a wavenumber of approximately 0.0163 rad/m, and this corresponds to a wavelength of about 386 m. Since the deep water approximation is generally valid at depths of greater than ½ the wavelength, the depth threshold is set at 193 m.

The low pass filtered mss (LPmss) is then computed from the wave elevation wavenumber spectrum according to Equation (1.8). As noted above, for the 3-m discus buoys, the upper wavenumber of the waves the buoys are capable of sensing is about 1 rad/m. In practice, there is also a lower bound. This lower bound is small enough to be not of significance, because not only is there little wave energy in the longer wavelengths, the mss statistic also emphasizes the higher wavenumber portions of the wave spectrum.

For short waves, it is known that the current or longwave-induced Doppler shift may be a significant source of error in blind applications of the above conversion procedure. The Doppler frequency shift is equal to $\vec{k} \cdot \vec{c}$, where $\vec{k}$ is the vector wavenumber and $\vec{c}$ is the vector current velocity. The wavelengths measured by discus buoys are comparatively long, so, as will be discussed in a later section, a bound can only be computed for the microwave regime. These relatively long wavelengths fortuitously imply that the Doppler shift can be ignored given the typical magnitudes of current velocities [Hwang, 2005b].

2.4 Separation Frequency and Swell

For this study, wind seas are of exclusive interest. Field data inevitably include both swells and wind seas. Winds in nature are also never truly constant nor steady in time or space, so the division between wind seas and swell is somewhat artificial. A common method used to separate swell and wind seas for a 1-D spectrum involves the designation of a "separation frequency", above which the waves are classified as wind seas; the rest are taken to be swell [e.g., Hwang et al., 2012]. In this study, no separation frequency is used for the following reasons. First, the division between wind seas and swell is seldom clear-cut. As wind seas become more mature, the peak frequency downshifts and may occupy the same frequency band as swell, in which case the application of a separation frequency is no longer justified. Secondly, the mss is dependent on the wavenumber limits of integration. Even if the region of overlap between wind sea and swell wavenumber is small, if the separation frequency is changed at each instant in time, errors in the estimation of the separation frequency and in their changes could introduce artificial signals in the mss that affect the correlation between wind and waves. Introducing a constant separation frequency would be equivalent to considering only a bandpass filtered version of the mss, which has been carried out in [Chen et al., 2012]. (It should be noted that the results in Chen et al. [2012] overestimate the lag time by approximately 25 min due to an erroneous interpretation of the wind and wave acquisition times.)

Swell is, by definition, uncorrelated with the local wind. Swell may well be correlated (albeit indirectly) with the response of the waves, however. The level of swell, as well as its direction, is expected to be highly correlated with location, which in turn is related to the fetch, and, as shown in Section 5, fetch has a strong effect on the evolution of the wind sea. But this relationship is correlative only – swell does not cause the response time to shift, because it has zero correlation with temporal changes in the wind speed. Thus, whether swell is removed in processing or not is immaterial to the response time itself. In particular, given our method for determining response time (discussed in the next section), the presence of swell, or lack thereof, is only expected to shift the noise floor, but not the response time statistic itself.

2.5 Response Time Analysis

In deep water, the action balance of waves dictates that the growth of waves is dominated by three source terms: input due to wind forcing, dissipation due to breaking, and nonlinear quadruplet wave-wave interactions. When there is a net energy input, the waves grow continuously, and the rate of growth decreases over time. Whether there exists an asymptotic limit, the so-called “fully-developed” condition, remains an open question

[Hwang et al., 2004a]. Drawing from the theory of duration-limited and fetch-limited growth of dimensionless energy and frequency, we are led to propose that the growth of mss, a non-dimensional quantity, can be expressed as a function of dimensionless duration and dimensionless fetch:

$$mss = F\left(t^*, x^*\right)$$

where $t^* = tg/U$ is the dimensionless duration and $x^* = xg/U^2$ is dimensionless fetch, both scaled by a wind speed U at some arbitrary height. t and x are the corresponding dimensional quantities, and g denotes the gravitational acceleration.

In the following analysis, instead of attempting to derive the growth functions themselves, we restrict our analysis to the determination of a single characteristic response time. Because the winds are non-steady, there is no obvious choice for the wind speed scaling. We therefore focus on the determination of a dimensional response time in this study, and reserve consideration of a non-dimensional growth function for future work.

Chen et al. [2012] previously presented a definition of response time based on the lag-correlator. The lag-correlation between two continuous-time signals $r(\tau)$ and $s(\tau)$ is defined as the convolution given by

$$\psi_{rs}(t) \triangleq \lim_{T\to\infty} \int_{-T}^{T} r(\tau'+t)\, s(\tau')\, d\tau'.$$

The response time was then defined as the time lag, t, at which the lag correlation is maximized. We propose here an alternative definition for response time that is found to be much less susceptible to noise in the wind and wave data. The alternative procedure follows these steps:

1. Start with a time series of wind speed and mss data, $U(\tau)$ and $mss(\tau)$, for a given buoy.

2. Form a population of sample pairs, $\{U(\tau), mss(\tau - t)\}$, where τ is a (variable) time lag.

3. Perform a least-squares, second order polynomial fit between $U(\tau)$ and $mss(\tau - t)$. Note the residual RMS difference in the fit.

4. Vary the time lag, t, and find the lag which minimizes the residual RMS difference. This lag is defined as the response time.

An example of this procedure is presented in the next subsection. We then use the procedure to derive a stable, long term response time, and discuss general characteristics applicable to all cases. In this paper, we will refer to this method as the RMS minimizer, in contrast to the lag-correlator.

2.5.1 Example of Response Time Determination and Discussion

We consider here the continuous 30-day wind and mss measurements made by Station 42058 from Jan. 1 to Jan. 31 of 2009. A scatter plot of the wind speed and mss measurements with no lag time applied is shown in Figure 10.

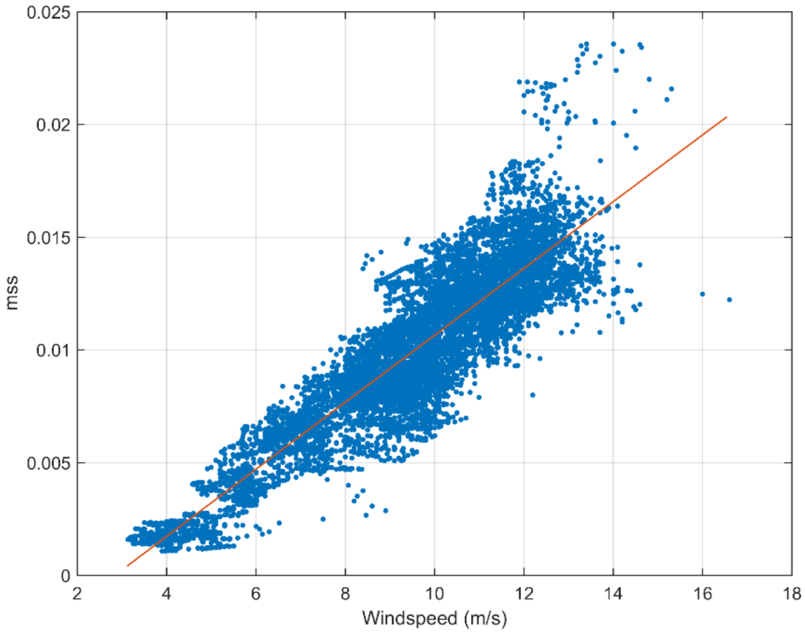

Figure 10: Scatter plot of the wind speed and mss measurements made by Station 42058 from Jan. 1 to Jan. 31, 2009, with no lag time applied. The quadratic fit is shown in red.

The scatter could be due to swell, duration, and other factors considered in the following sections. In addition, scatter is also contributed by averaging and interpolation – we recall the waves are 1 hour averages while the winds are 10 min averages. We see, later, however, that by leveraging the data collected over eleven years, we can derive with some confidence a response time better than 1 hour in resolution.

We note that the swell contributes a positive bias to the wind sea mss; the mss in the scatter plot is not just due to wind waves. However, as noted, the swell is uncorrelated with wind speed and changes in wind speed. Therefore, it does not impact the derived response time. However, note that inclusion of the swell mss is desirable if we are trying to derive a geophysical model function that relates wind speed to the remotely sensed mss observable, because the mss observable also includes swell contributions.

A least-squares, second order polynomial fit is applied to the data shown in Figure 10, and the residual RMS difference is noted. This is then repeated using time lags of between 0 and 10 hours. The resulting residual difference vs. lag time is shown in Figure 11.

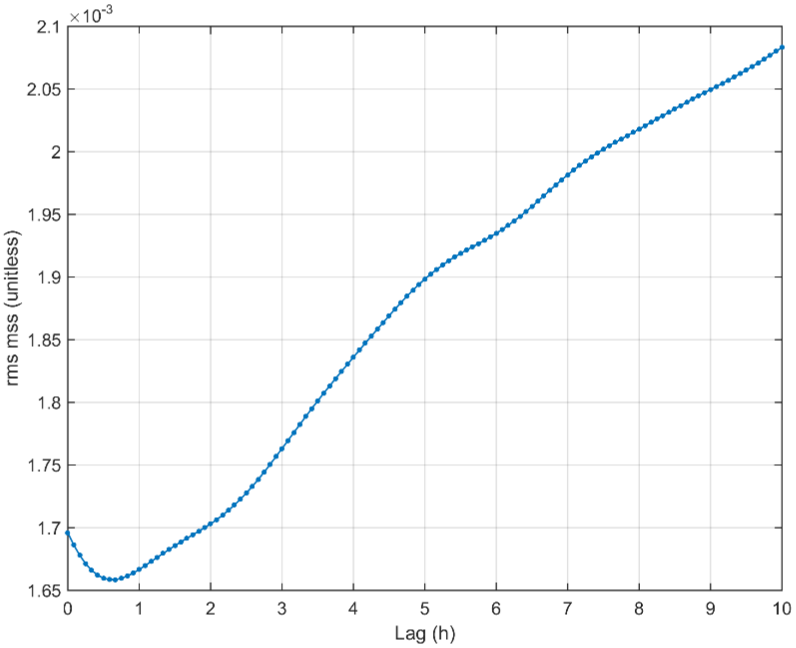

Figure 11: Residual RMS difference vs. lag time, for Station 42058 from Jan. 1 to Jan. 31, 2009.

The time lag at which the residual RMS difference is minimized is found to be 40 minutes (~0.7 h). This, then, is the response time of the mss to the local wind speed for this 30-day data set.

It should be noted that the above procedure needs to be applied to continuous, gap-free wind and wave signals to ensure the proper time match-up of lagged waves and wind. We apply the above method to all continuous 30 day signals over the full 11 years of data for the same buoy. A histogram of the resulting response times for Buoy Station 42058 is shown in Figure 12.

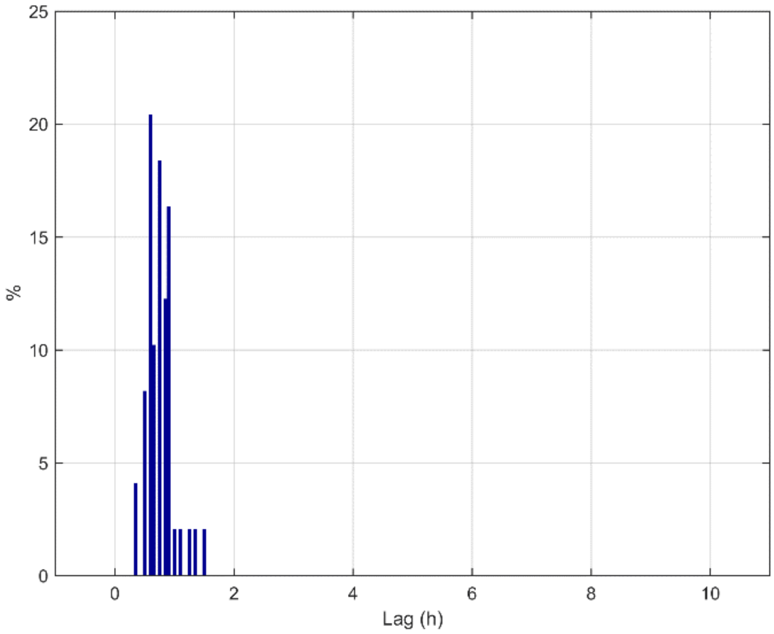

Figure 12: Histogram of response times derived from consecutive 30-day measurements of Station 42058 over 11 years (2004 to 2014, inclusive). The response times are found by minimizing the residual RMS difference.

Note that, while there is some spread in the derived response time over the 11 years, the distribution is not uniform but rather highly localized. The mean value of the response time is found to be ~0.8 hours (45 min). *This value is considered as our best estimate of the response time for Station 42058.*

For comparison, we apply the lag-correlator technique used in Chen et al. [2012] to the same dataset in 30 day segments. Figure 13 shows the histogram of response times produced using its procedure.

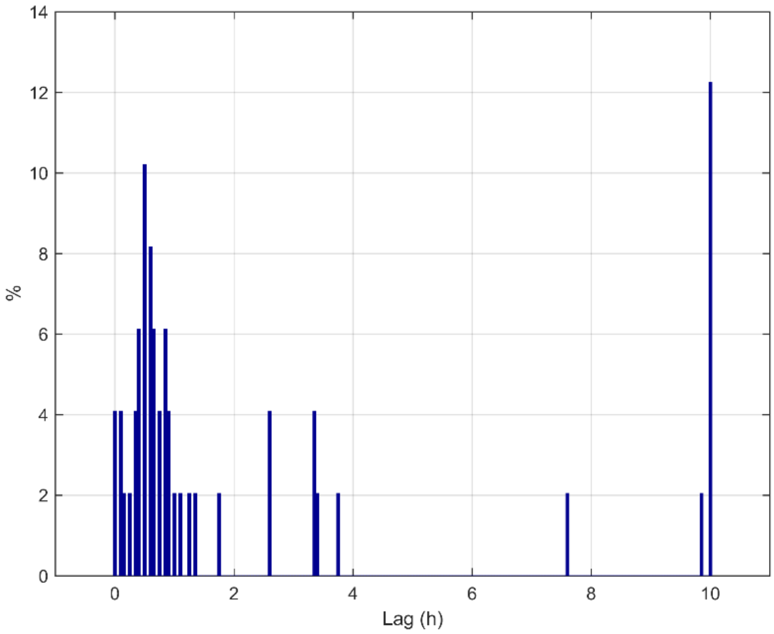

Figure 13: Histogram of lag-correlation response times found derived from consecutive 30-day measurements of Station 42058 over 11 years. These response times are found to be less stable than the ones derived by minimizing the RMS residual, so they are not used in this paper.

The lag-correlator method is seen to be less stable, and sometimes misidentifies the wind wave response resulting in a more than 10 hour lag. Response times greater than 10 hours are not believed to be physically reasonable – when the signal lengths are increased, these anomalously long lags are no longer seen. Because of this, the lag-correlator is not used in this study. We note, however, that if the 10-hour-and-greater response times found by the lag-correlator are excluded, the mean response time found by both the RMS-minimizer and the lag-correlator are reasonably close.

2.6 Results for All Buoys

Forty-six NDBC buoys were found to satisfy the criteria specified in Section 2.2. We apply the RMS minimization procedure to all 46 buoys, with 11 years of data, to obtain response times for each location. Data in all field conditions are used. Figure 7 shows a map of the response time derived at each buoy location.

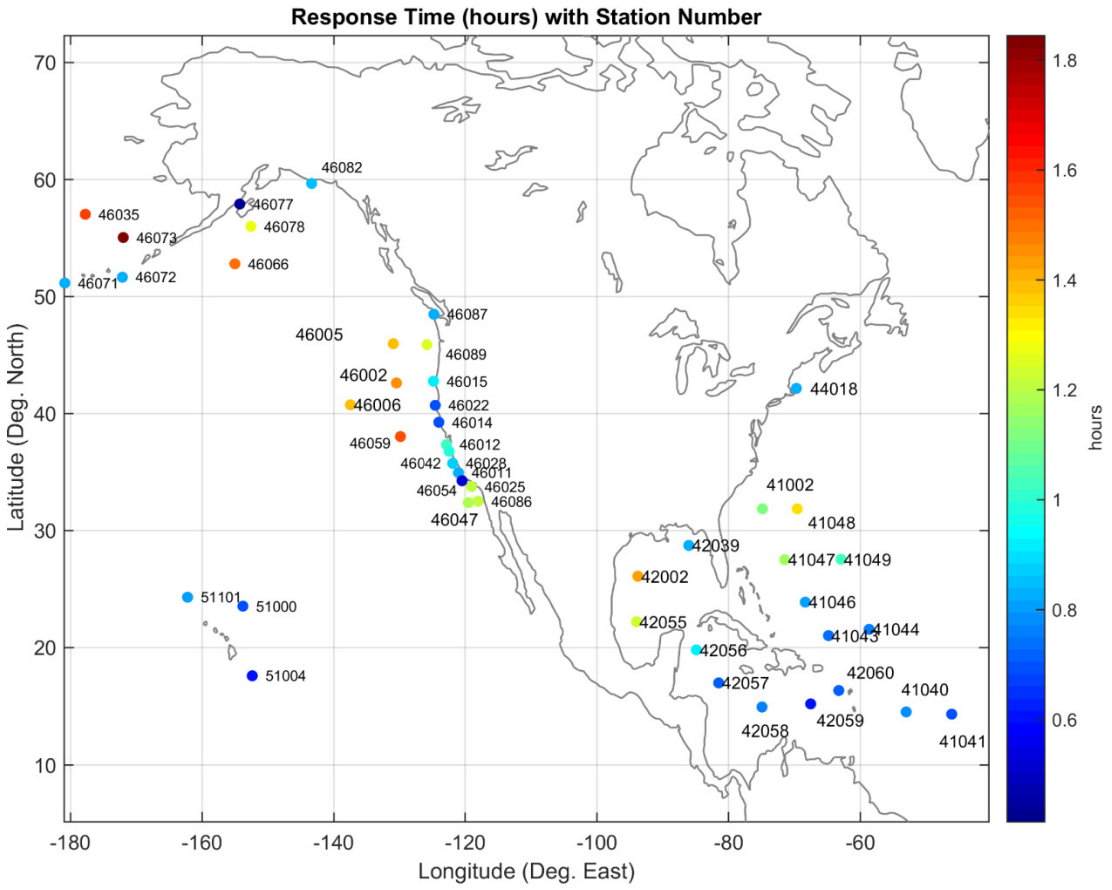

Figure 14: Response times of the 46 buoy stations under study.

The response times are seen to vary between 0.4 and 1.8 hrs. It is also seen that, in general, stations with a close proximity to one another have similar response times, likely because they are subjected to the same environmental conditions. In Sections 2.8 to 2.10, we investigate the dependencies of these response times on environmental factors.

2.7 Comparisons to Wave Models

Hwang et al. [2013; 2015] and Elfouhaily et al. [1997] designed models of wave spectra that depend on wind speed and wave age. By using the second-order duration-limited growth functions from [Hwang et al., 2004a; Hwang et al., 2005a], the wave age can be computed knowing the duration and wind speed. The wave age and wind speed can then be used with the wave spectrum models to compute an LPmss bounded above by 1 rad/m (as measured by the buoys). The duration-limited growth of LPmss predicted by the two wave spectra are shown in Figures 15 and 16.

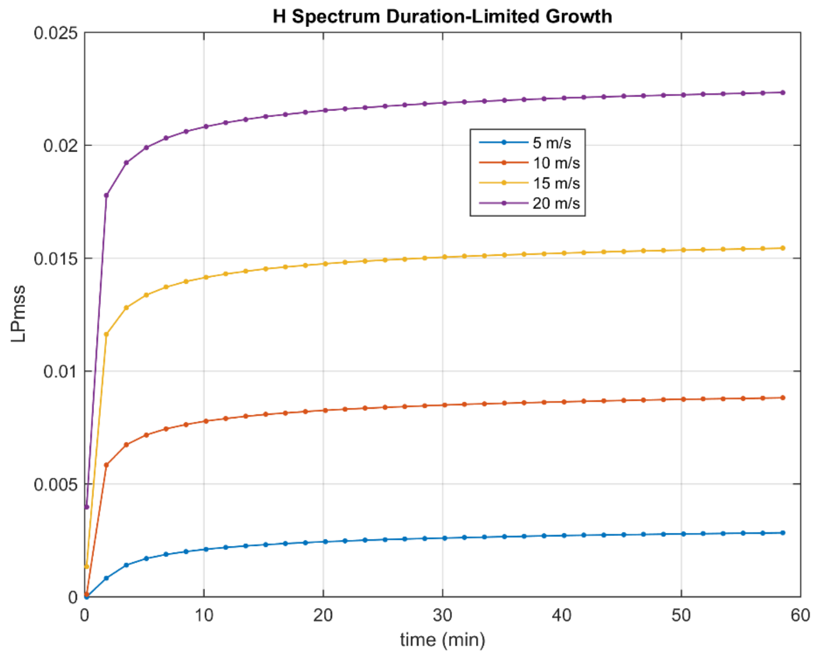

Figure 15: Duration-limited growth of LPmss, as predicted by the wave-age dependent H spectrum. Note the unit for time on the abscissa is minutes.

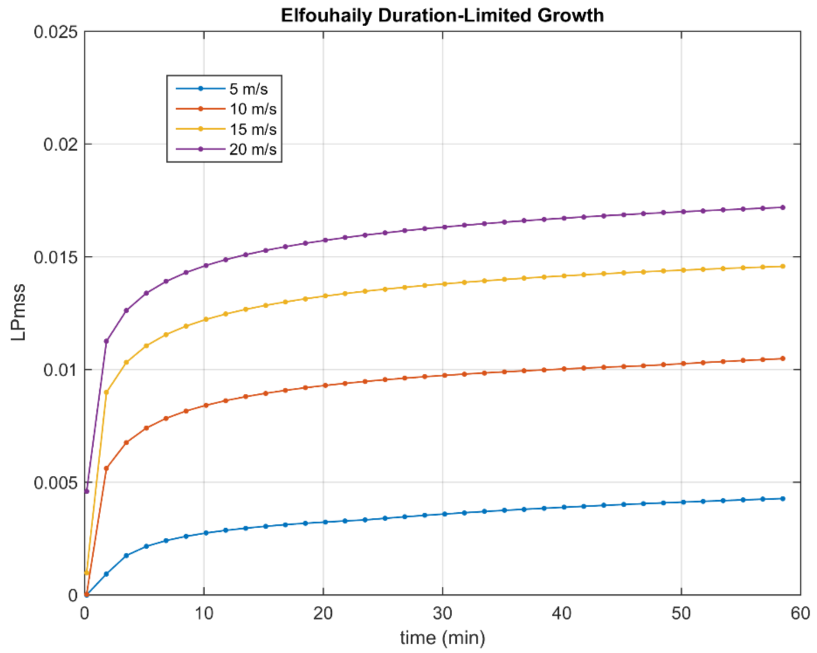

Figure 16: Duration-limited growth of LPmss, as predicted by the wave-age dependent Elfouhaily spectrum. Note the unit for time on the abscissa is minutes.

Duration-limited growth assumes a wind speed step function waveform starting at 0 m/s up to the scaling wind speed magnitude (varied from 5 to 20 m/s in Figures 15 and 16). As mentioned in Section 2.1, duration-limited growth implies large fetch. In reality, wind speed fluctuations are not step functions starting from calm conditions, the fetch is finite, and the correlation of wind and waves incorporates wave growth as well as wave decay.

However, the response time (as defined in Section 2.5) of wave growth in ideal duration-limited conditions can be derived from the results in Figures 15 and 16. An order-of-magnitude estimate of the response time corresponds to the time the duration-limited LPmss grows to 50% of its final, steady state value (assuming one exists). Had the wave response been a ramp function, this estimate obtained with this method would be perfect. The response times derived thus are shown as a function of wind speed in Figure 17.

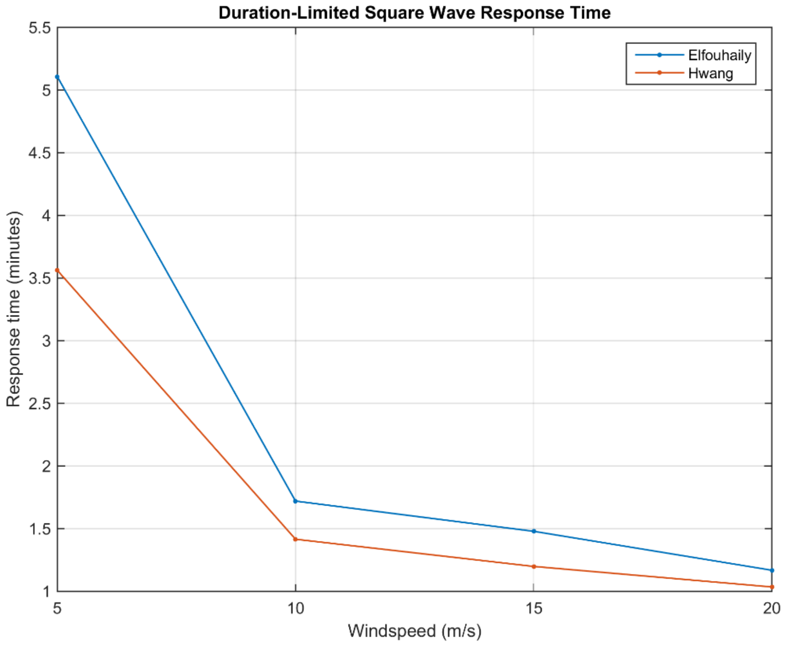

Figure 17: Response time vs. U10 magnitude, as predicted by the H and Elfouhaily spectra. Note the unit of the ordinate is minutes.

The response times corresponding to wave growth, as predicted by the two models, are seen to be significantly lower than the empirical results found from the NDBC buoy data. This could be due to a much slower wave decay rate than growth rate, or the overestimation of the wave growth rate in the models. Further study, perhaps with data collected in carefully controlled conditions, is needed to resolve this question.

Next, we use a third-generation wave model that does not restrict the shape of the spectrum. As mentioned in Chapter 1, WW3 [Tolman et al., 2014] is a third generation wave model that is run operationally by the National Weather Service (NWS). Our first task is to verify the consistency between WW3 output and our buoy mss results. There have been many validation efforts involving the significant wave height product of WW3, which is of primary interest to mariners and sailors. The publicly available WW3 code consists of several source term packages, which can be selected at compile-time. Only one, however, has been validated with regards to mss, and only at low wind speeds. This is the “ST4” package due to Ardhuin et al. [2010].

Since our buoy mss response results have not been generalized through non-dimensionalization, we derive a dimensional response time from the wave model output to make an order-of-magnitude comparison.

Again, we consider only deep water conditions, in which WW3 performs well. We set up an ideal duration-limited scenario, and select a location with a sufficiently large fetch.

We note that our response times estimated from buoy measurements are due to both wave growth and decay. For wave growth, we apply a step function as the wind forcing, and to simulate wave decay, we apply a negative step function, shown in the top panels of Figures 18 and 19. The wind inputs applied are spatially uniform in both cases – a representative value of 7.5 m/s is chosen. The time series of *LPmss* for the downwind location can be derived from model output. We first consider *LPmss* with k_u = 1 rad/m, the upper wavenumber sensed by buoys. The resulting *LPmss* time series for both cases are shown in the lower panels of Figures 18 and 19.

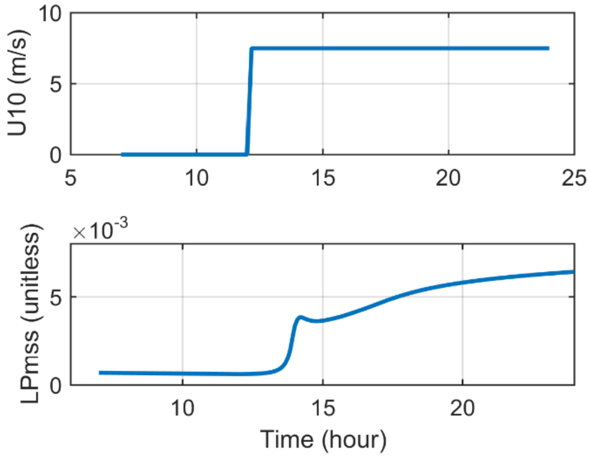

Figure 18: Wave growth time series: wind speed at 10 m height (top), and LPmss up to 1 rad/m (bottom)

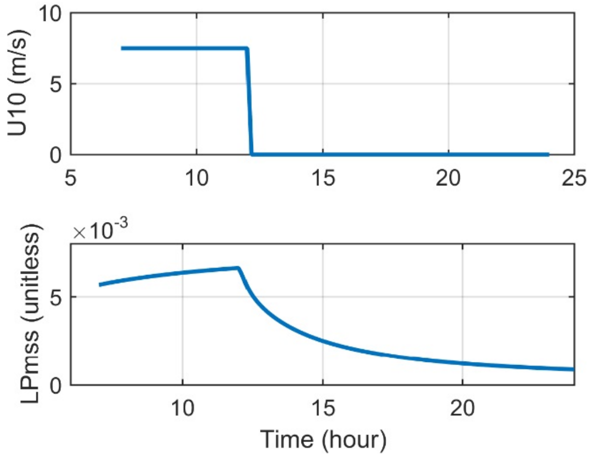

Figure 19: Wave decay time series: wind speed at 10 m height (top), and LPmss up to 1 rad/m (bottom)

Next, we apply the same rms minimization method used to derive the response times from buoy measurements. The rms vs. lag time plots are shown in Figures 20 and 21, for wave growth and decay, respectively. The lag time corresponding to the minimum of the plots is the response time, which we find to be 1.83 hours for growth, and 1.17 hours for decay.

Interestingly, we see that in the case of wave decay, the rate of change is lower than that of wave growth. However, the response time for decay is shorter than growth – in wave growth, the wind takes some time to initiate significant growth, at which point the rate increases quickly. This can perhaps be attributed to the transition from “skin drag” to “form drag” mechanisms of wind input [Donelan et al., 2012].

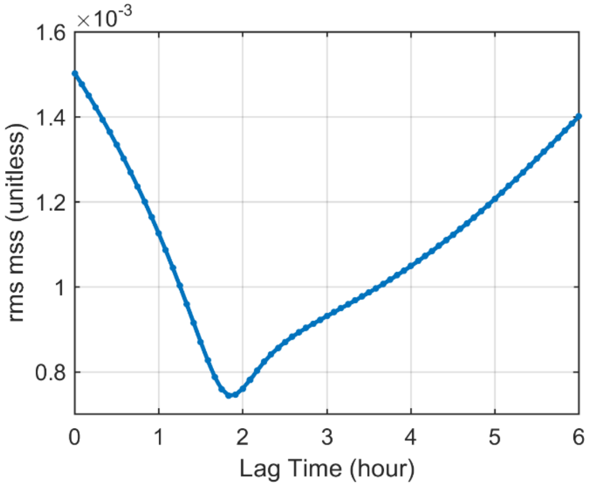

Figure 20: RMS mss vs. lag time for wave growth. The response time is found to be 1.83 hours.

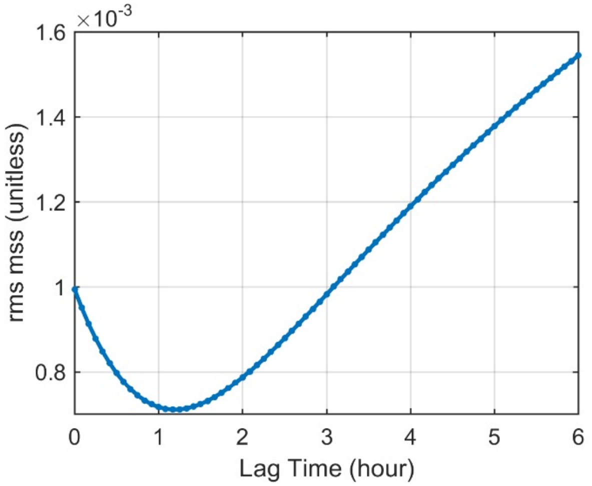

Figure 21: RMS mss vs. lag time for wave decay. The response time is found to be 1.17 hours.

The average of the response times for wave growth and decay is 1.5 hours, which is in keeping with the response time derived from buoy measurements.

Our next step is to use the wave model to predict the response time of the CYGNSS *LPmss*. The appropriate k_u for CYGNSS is found to be about 9.54 rad/m. By integrating the wave spectra output of WW3, as was done in comparison to buoy *LPmss*, we find the CYGNSS L-band wave growth response time to be 0.42 hours, and the decay response time to be 0.25 hours. These average to about 0.3 hours, or 20 minutes.

2.8 Dependence of Response Time on Wind Speed

The analysis based on parametric wave models, as illustrated in Figure 17, predicts that the response time decreases as wind speed increases. To assess whether this behavior is also exhibited by the NDBC buoy data, we apply the same RMS minimization procedure discussed previously to the wind speed and LPmss data of each buoy, except now we bin the data according to wind speed and consider the data in each bin separately. The response times identified for each bin are then averaged. We consider 3 wind speed bins: 0 – 6 m/s, 6 – 8.5 m/s, and 8.5 – 20 m/s. The binning was made non-uniform because most data fall between 5 and 15 m/s; even so, there is insufficient data for some bins for some buoys, in which case a response time cannot be determined reliably for that case.

Due to the number of buoys, we present the results in two separate plots in Figure 22 to avoid clutter:

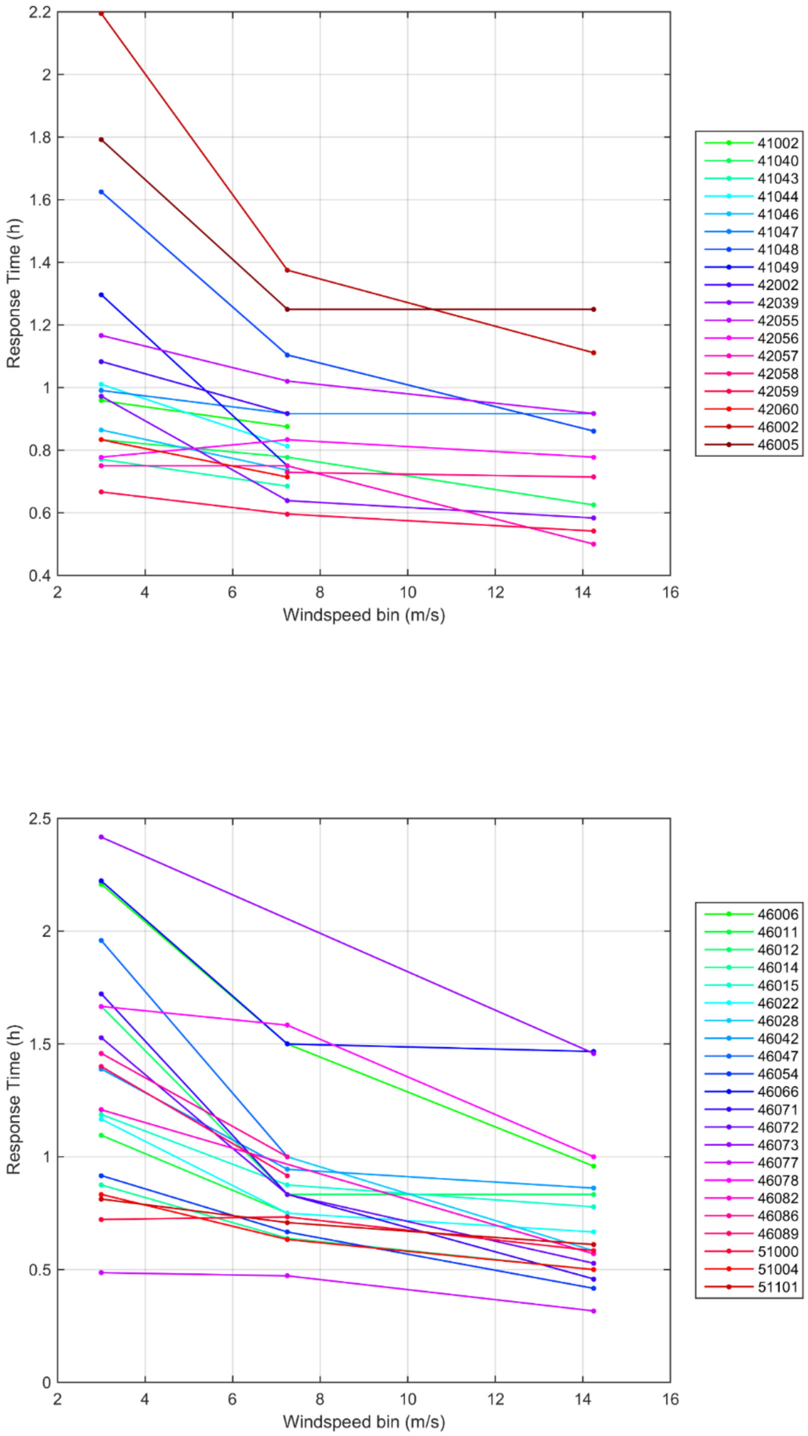

(a)

(b)

Figure 22: Response time dependency on wind speed magnitude.

In almost all cases, a monotonically decreasing response time for increasing wind speed is evident, in agreement with the models.

2.9 Dependence of Response Time on Fetch

Fetch is often difficult to quantify. In this section, fetch is not explicitly calculated. We are able to make inferences of the relative magnitudes of fetch, however, by examining the dominant wind direction in some locations.

The histogram wind direction for all 11 years of data is presented in Figure 23 for Station 42058 as an example. Station 42058 is located in the middle of the Caribbean Sea with a nominal position of 14°55'23" N, 74°55'4" W. The wind direction convention is clockwise from the North, and indicates where the wind is coming from.

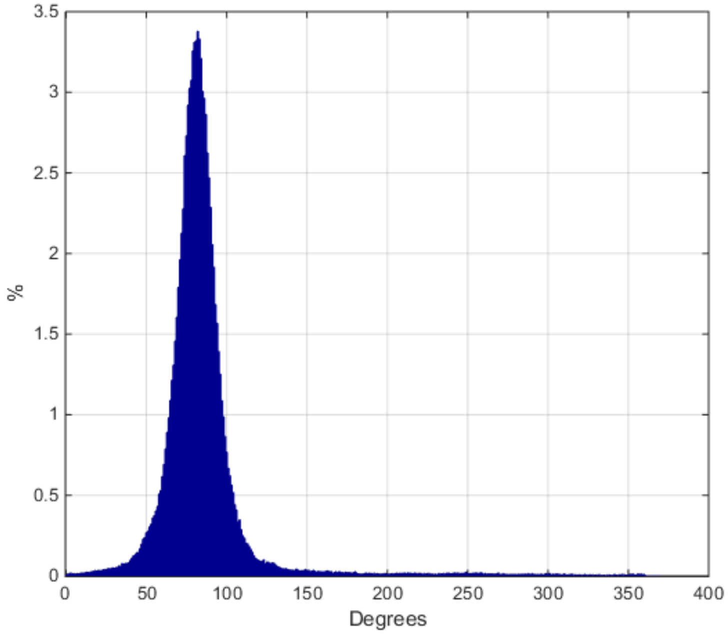

Figure 23: Wind direction histogram of 42058 over 11 years. The wind direction is clockwise from the North, and indicates the direction the wind is coming from. It is seen that the dominant wind direction is from East to West for Station 42058.

We define the dominant wind direction to be the direction where the distribution is maximum. The maximum is used instead of the average, because the wind direction distribution may be multimodal.

In Figure 24, we plot the dominant wind directions for all 46 buoys. The arrow points downwind (in the direction of air flow).

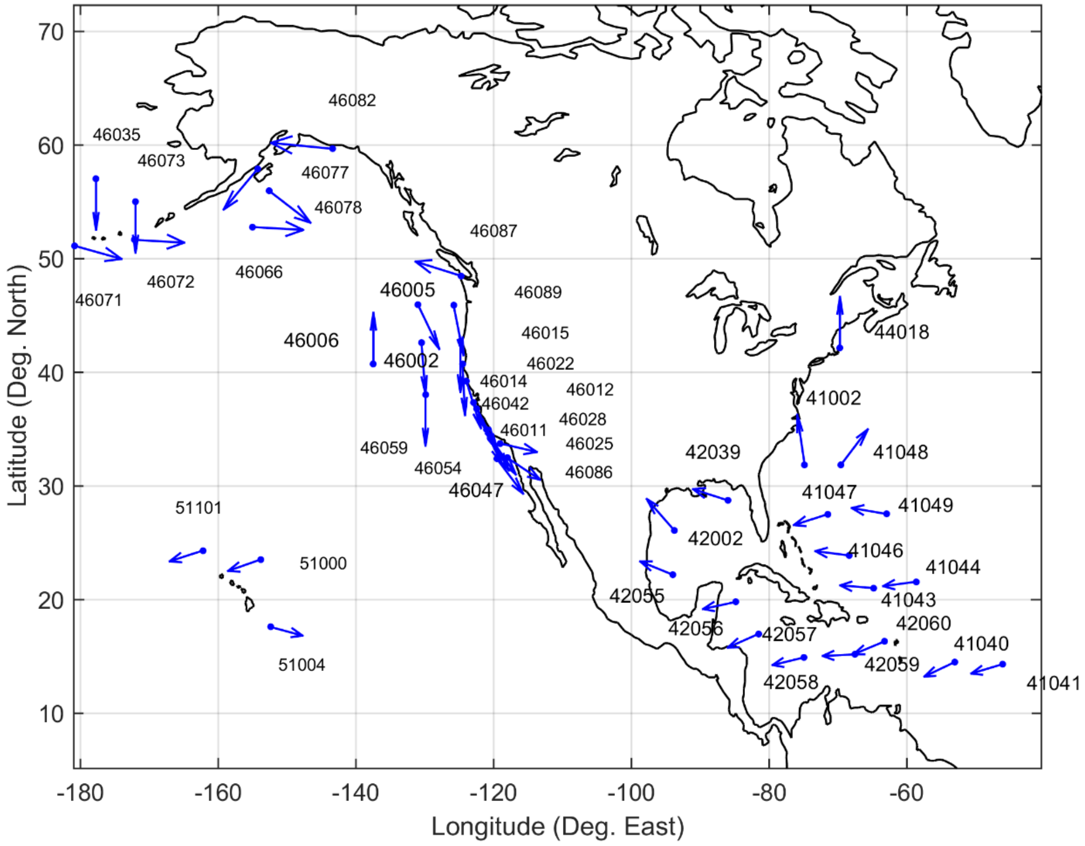

Figure 24: Dominant wind directions for the 46 buoys under study. The arrows point downwind.

We then choose suitable locations for fetch studies. The locations should be close in proximity with approximately the same wind direction, because it is desirable that winds do not change appreciably over these distances. Only locations far from land are considered to avoid coastal wave processes such as reflection and bottom refraction. The selected stations, along with the response times, are shown in Figure 25.

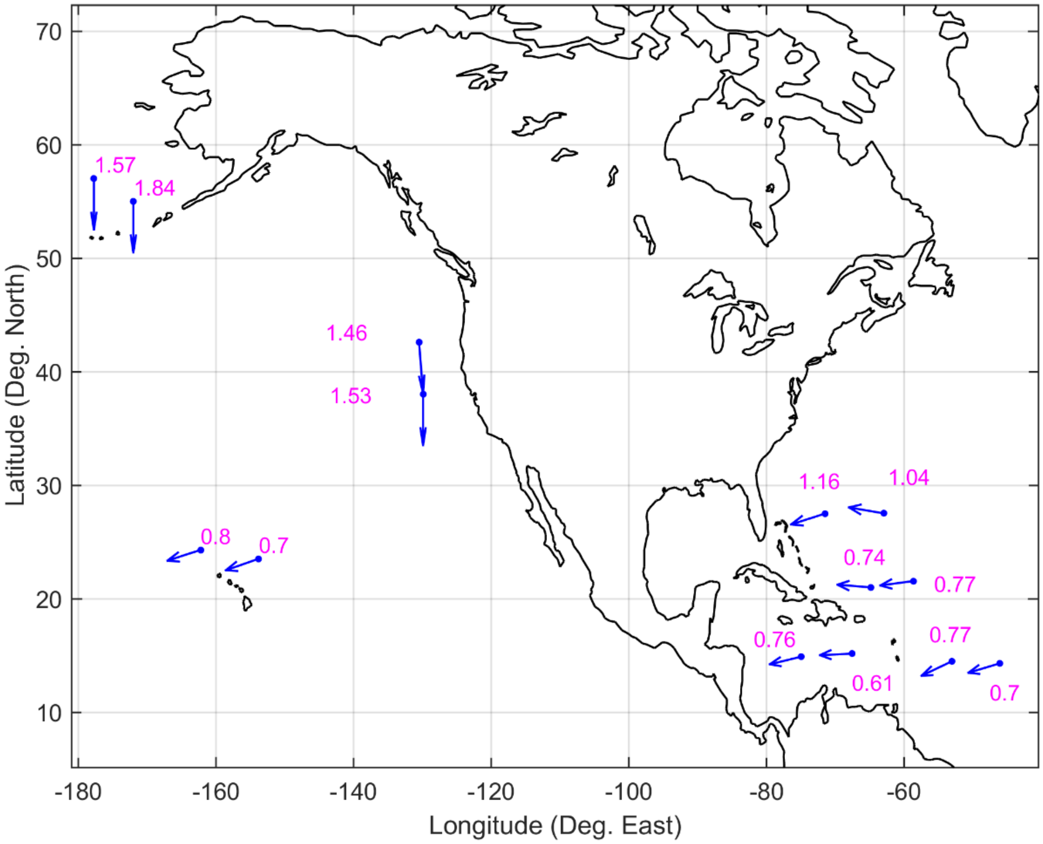

Figure 25: The arrows point in the direction the wind is blowing towards. Numeric labels correspond to response time in hours. Stations 41043 (downwind) and 41044 (upwind) are circled in red; their response times in the context of fetch is discussed in the text.

We see that in all cases but one, the downwind location, with larger fetch, has a longer response time. The one exception is circled in red. This is possibly because the downwind station, 41043, has a slightly higher average wind speed (0.3 m/s) than the upwind station. Section 6 indicates that the atmospheric stratification is less stable on average at 41043 than 41044, which may also contribute to the lower response time of 41043.

2.10 Dependence of Response Time on Atmospheric Stability

Kahma et al. [1992] analyzed six well-known fetch-limited datasets available at the time in an attempt to reconcile the differences in wave growth. They derived the fetch-limited growth relations separately for unstable and stable conditions, and noted that unstable stratification enhanced wave growth, even when using friction velocity as the scaling wind speed. Young et al. (1998) analyzed data from the Lake George experiment, which is documented in [Young and Verhagen, 1996], using the Bulk Richardson Number to characterize atmospheric stability. It is defined as

$$R_b = \frac{g\left(T_a - SST\right)}{z_t T_a \left(U / z\right)^2} \tag{2.1}$$

where SST is the sea-surface temperature, T_a is the air temperature at height z_t, and U is the wind speed at height z. Thus, negative values are indicative of unstable stratification while positive values represent stable conditions. In addition to other findings, they concluded that wave growth is more pronounced (as a function of fetch) in unstable conditions, in agreement with Kahma et al. [1992]. Since duration-limited growth can be related to the fetch-limited growth using the space-time conversion relations [Hwang et al., 2004a], we expect that waves grow more rapidly as a function of time in duration-limited cases as well. This implies a shorter response time in less stable conditions, which we now verify.

In the following analysis, we also employ the Bulk Richardson Number as a measure of stability, using the averaged 5 m height wind speed for scaling. Averaged T_a and SST

values are used in Equation (2.1) to compute an R_b for each station, and this is then plotted against the response time in Figure 26.

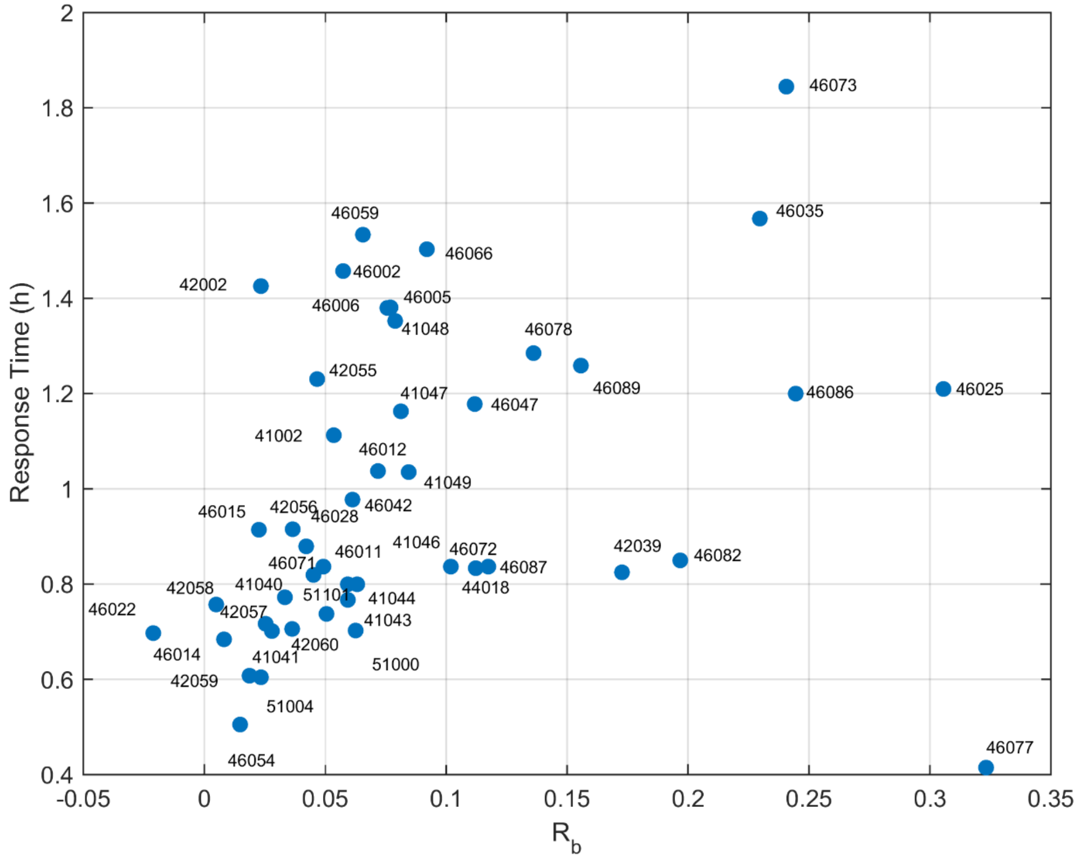

Figure 26: Wave response time vs. the Bulk Richardson Number. A positive correlation is seen, indicating lower atmospheric stability corresponds to a faster response.

A positive correlation is seen, with lower atmospheric stability being associated with a shorter response time, in agreement with previous empirical studies. Our results, therefore, support the idea [Young, 1998] that wave growth similarity theory should be augmented with a dimensionless group characterizing atmospheric stability, in addition to dependencies on dimensionless fetch and duration. The apparent outlier in Figure 26, Station 46077, is located just south of Alaska and north of an island. This station likely experiences short fetch wave conditions, and this may contribute to its short response time.

2.11 Dependence of Response Time on Wavelength and Implications for L-band Remote Sensing

We now investigate the behavior of the response time as the upper limit of integration in Equation (1.8) is varied. Note that, instead of analyzing the bandpass mss studied previously by Chen et al. [2012], we study the LPmss, which is of interest to bistatic sensors and radar altimeters. We choose 4 upper limits, and they are chosen so that the cumulative distribution function (CDF) of LPmss as a function of wavelength attains 25%, 50%, 75% and 100% respectively for the 4 LPmss'es. (The CDF is computed using the Elfouhaily wave spectrum, which is very similar to the CDF derived from the H spectrum [Hwang et al., 2013].)

Similar to the method used to analyze the wind speed dependency, we average the response times for each LPmss and each buoy for 11 years. The results are presented in the two plots of Figure 27.

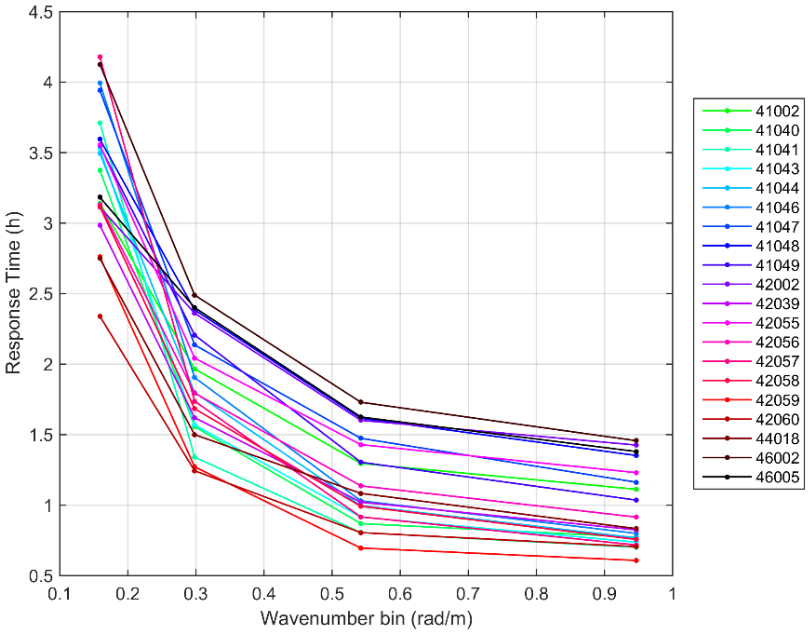

(a)

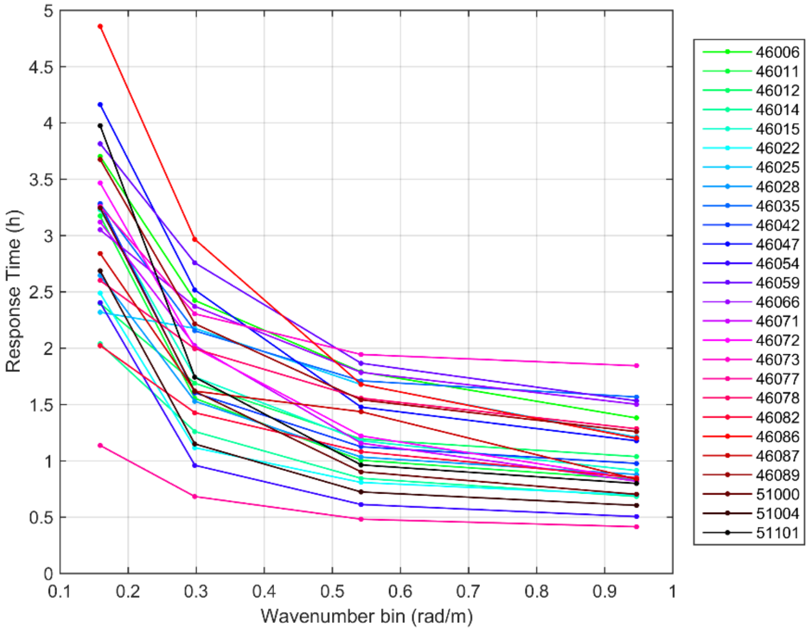

(b)

Figure 27: Response time dependency on upper limit of integration of LPmss. The buoys have been divided into two sets and plotted separately in (a) and (b) to reduce clutter.

The response time is seen to decrease monotonically as the upper wavenumber is increased, for almost all of the buoys under study. This is consistent with the present understanding on wind-wave growth: shorter waves become well-developed first, when the energy they possess saturates. At this point, further energy input from wind is either dissipated by breaking or transferred to longer waves by nonlinear interactions.

Spaceborne L-band bistatic remote sensing of ocean surface wind speed has recently been proposed by Ruf et al. [2012]. In the rest of this section, we obtain rough estimates of the response times at L-band by extrapolation. It was found that power functions of the form of Equation (2.2) fit the data well for almost all of the buoys under consideration.

$$t(k) = ak^b + c \tag{2.2}$$

Functional fittings are performed for all 46 stations, and the fitting function is then used to extrapolate to a response time at L-band (10 rad/m). The fitting function for one station resulted in a non-physical negative response time at L-band, which we take to be 0 for the statistics presented in the rest of this section. The function fittings for two stations are shown in Figure 28 – these being the ones with the maximum and minimum (physical) response times. The parameters of the fitting functions for these two stations are listed in Table 3.

Table 3: Parameters of the fitted power function (Equation 5) for the stations with extremal response times.

	a	b	c
Station 46073 (Max. Response Time)	0.07758	-1.614	1.751
Station 46071 (Min. Response Time)	0.996	-0.8508	0.1071

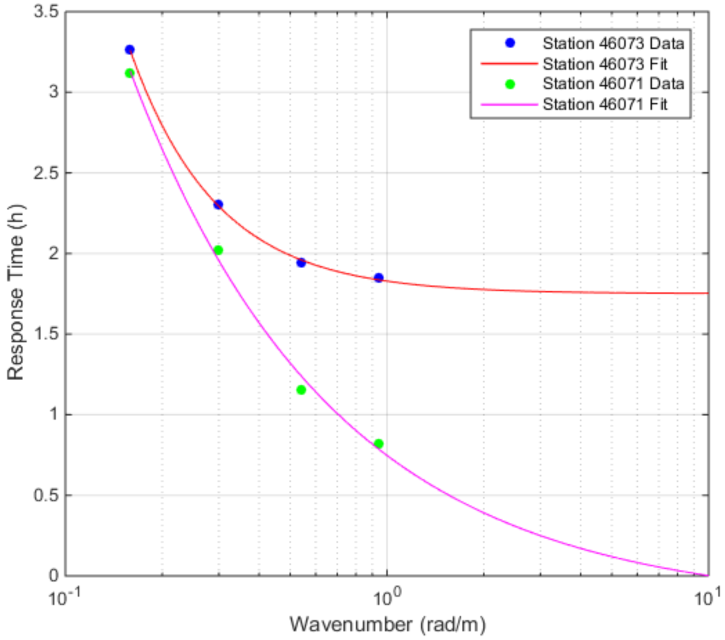

Figure 28: Power function (Equation 5) fittings of the wavenumber dependency of response time, for the two station with extremal response times at L-band. Note the logarithmic scale on the abscissa.

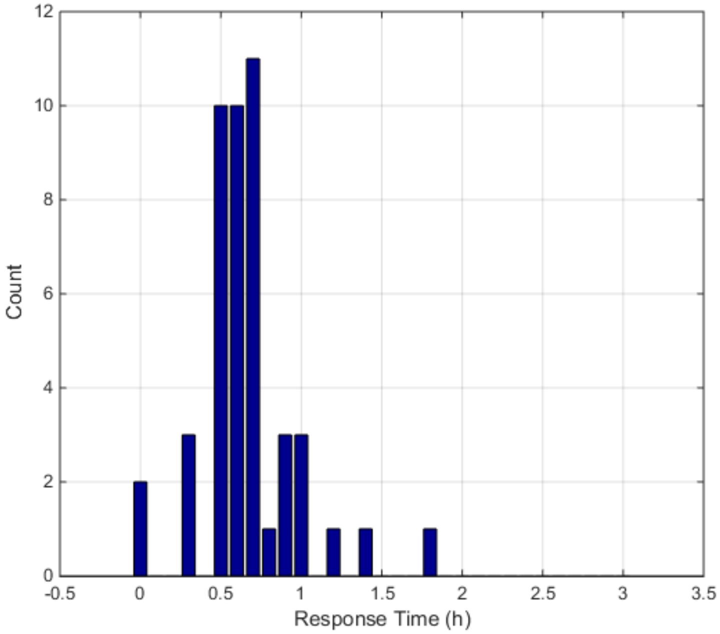

Figure 29: Histogram of the estimated L-band response times for the 46 buoys under study.

A histogram of the L-band response times derived for the 46 buoys is shown in Figure 29. It is seen that over 93% of the L-band response times fall between 0.3 and 1.4 hours, with a mean of 0.66 hours.

Weissman et al. [1996] analyzed the spectral correlation of wind and waves using data from an L-band scatterometer and a sonic anemometer. The radar data consisted of about 4 days of data in records of about 5 minutes long, which confined the applicability of their results to fluctuations on the order of 0.01 Hz and higher. The low coherence they found at L-band implies that if an L-band response time can be identified, it would be greater than timescales of 100 seconds. Our results are, therefore, in general agreement with this conclusion.

It should be noted that the response time extrapolation to L-band is speculative, and measurements of mss at these wavelengths, in a variety of conditions, would be needed validate this result.

2.12 Concluding Remarks

In this work, we analyzed collocated wind and wave data measured by 64 moored discus buoys over 11 years. We found the response times of mss to wind forcing for each buoy to be reasonably stable, and all response times are bounded between 0.4 and 1.8 hours. We also find that the mss response time is dependent on wind speed magnitude, fetch, atmospheric stability, and wavelength. The response times are, however, much greater than what current models of wave age dependent wave spectra predict. This may be due to effects of wave decay or inaccurate wave age dependency in the models.

Our results would be directly relevant to HF and VHF remote sensing of the ocean. They can also serve as bounds for L-band bistatic remote sensing. The Cyclone Global Navigation Satellite System (CYGNSS) is a spaceborne L-band bistatic mission to be launched in late 2016 [Ruf et al., 2016]. Integrations of the H spectrum reveal for wind speeds ranging from 5 m/s to 15 m/s, which constitutes most of the data collected by NDBC buoys, 50% of the LPmss sensitivity to wind is due to waves 6.6 m and longer (the NDBC buoy wavelength range). This percentage is very sensitive to wind speed, and becomes higher as the wind speed increases.

For CYGNSS's incidence angle, the upper wavenumber limit sensed is about 10 rad/m. We saw in Section 5.10 that the extrapolated L-band response exhibits a rather large variability about a mean of 0.66 hours. We noted that our results are in keeping with previous observations by Weissman and al. [1996]. Chen et al. [2012] showed that response times of bandpass filtered mss also decreases monotonically with increasing wavenumber, so our results are also applicable to L-band scatterometers like SMAP [Entekhabi et al., 2010]. Furthermore, this study indicates that ancillary data such SST and air temperature could be beneficial in improving the accuracy of the wind retrievals.

Finally, we note that the data used in this analysis are limited in wavelengths sensed by the buoys (on the shorter end). In-situ measurements of short, intermediate-scale waves can be quite challenging [Hwang, 2005b]. Remotely sensed data, like those to be provided by CYGNSS, coupled with collocated in-situ wind measurements, will likely be invaluable for advancing our understanding of this topic.

Some of the results discussed in this chapter are published in Chen et al. [2016], with Christopher S. Ruf and Scott T. Gleason as coauthors. Richard Bouchard and John Tancredi of NDBC are acknowledged for their assistance in the interpretation of NDBC data, and Paul Hwang is thanked for providing the code for the H spectrum. Mounir Adjrad, Dallas Masters, Valery Zavorotny, Mark Donelan, and Bill Plant are also acknowledged for their input.

Chapter 3

Investigation of Non-Local Sea State Dependencies Using a Coupled Wave and Electromagnetic Scattering Model

Modelling GNSS-R ocean scattering at L-band presents novel challenges. Gravity-capillary waves tens of centimeters long are in a different regime than the millimeter capillary waves, because they are governed by different physics. With surface tension being negligible, these gravity-capillary waves take longer to dissipate and propagate further before decaying. There have been questions [Cardellach, 2014] and results showing non-negligible GNSS-R sensitivity to long gravity waves. However, such waves have yet to be taken into account in GNSS-R forward models. For example, the end-to-end simulator for the upcoming Cyclone Global Navigation Satellite System (CYGNSS) mission [Ruf et al., 2016a] uses the Katzberg relationship to model the roughness, which assumes that the scattering cross section is determined by the local, instantaneous wind speed alone [Ruf et al., 2016b]. The limitation of this assumption is illustrated in the follow-on Chapter 4, in which spaceborne scattering measurements are shown to exhibit large differences from those predicted by the Katzberg-model (e.g., Figure 35 and Figure 36).

Our objective is to develop (this chapter), and then experimentally validate (next chapter), a more accurate GNSS-R forward model by incorporating forcing effects other than local winds. In Section 3.1, we describe the model, which includes a third-generation wave model that has not previously been incorporated into a GNSS-R forward model. The rationale for the choice of the surface model and parameters therein are discussed.

3.1 The Forward Model

Since our interest is in mss, we use the Ardhuin et al. [2010] source term package, which is the only reported source term package for WW3 validated for mss. As mentioned earlier in Chapter 1, the spectral tail of high frequency waves is not completely resolved. All third-generation waves thus explicitly model the wave spectrum only up to a certain frequency, and attach a high-frequency tail thereafter. We select a simple k^{-3} spectral tail, which is suggested by the work of Banner et al. [1989], Forristall [1981], and Phillips [1958]; it is also in keeping with tail used by Reichl et al. [2015] in a high-frequency model based on WW3 (Chapter 1). The tail is attached at the last frequency modeled by WW3, and thus is completely determined by the value of the spectrum at that frequency. A more elaborate model may include a high-frequency model like that of Plant [2015], Hwang et al. [2013], or Elfouhaily [1997], but this option is not pursued here.

Our WW3 run is driven by the ECMWF operational wind analysis, and has 3-hour temporal output resolution and 0.5-degrees latitude and longitude spatial resolution. The last wavenumber before spectral tail attachment is 2.06 rad/m. The k^{-3} spectral tail ends at k_u, which is determined by the incidence angle of the track under consideration. For our simulation, the model is driven by wind only; currents play a minimal role globally [Bidlot, personal communication, 2016] - however, in hurricane conditions, currents can have a significant role [Fan et al., 2009]. We limit ourselves to non-hurricane conditions in this work, and thus neglect currents. In the following, we refer to the WW3 with spectral tail attached as the extended WW3 model.

An example of the attachment of the spectral tail is shown in Figure 30.

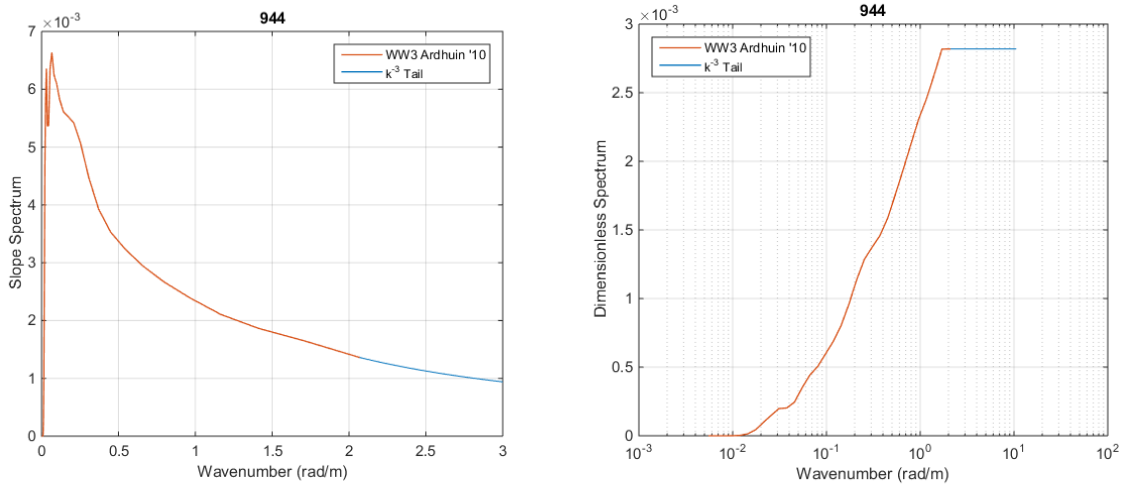

Figure 30: Example of extended WW3 slope spectrum with a) linear scale (plot upper limit adjusted to 3 rad/m), b) area conservative form.

3.2 GNSS-R Electromagnetic Scattering and Signal Processing Model

We use the Zavorotny and Voronovich [2000] model introduced in Chapter 1. In using Equation (1.12), τ's range is over about 30 us and f ranges over about 10 kHz. The glistening zone is chosen to be 200 km by 200 km centered at the specular point, which is sufficient for most scattering geometries of the TDS-1 instrument considered in Section 3.3. In order to focus on first-order effects, we make the simplifying assumption that the seas are isotropic and the two components of mss are equal. The two-dimensional Gaussian PDF in ZV, discussed in Appendix A, thus simplifies to

$$P(s_u, s_c) = \frac{1}{\pi mss} \exp\left\{ -\left(\frac{s_u^2 + s_c^2}{mss} \right) \right\} , \tag{3.1}$$

where the subscripts u and c denote the upwind and crosswind components. At the specular point, $P(0,0)$ is proportional to inverse of the mss.

3.3 Model Configuration and Post-Processing for TDS-1

TechDemoSat-1 (TDS-1) is a technology demonstration mission operated by Surrey Satellite Technology Limited (SSTL) [Jales and Unwin, 2015a], and one of the payloads is the Space GNSS Receiver Remote Sensing Instrument (SGR-ReSI), the GNSS-R instrument of interest. TDS-1 has a circular orbit with an altitude of about 630 km. Because there are other instruments on the TDS-1 mission, the SGR-ReSI has limited operating time, so the data it collects are limited. In this paper, all references to TDS measurements refer to data collected by the SGR-ReSI.

From Section 3.2, several pieces of information are required to compute the received signal. The GPS transmitted power is not published, so it is assumed to be constant. The other parameters needed are:

- transmitter position and velocity,
- receiver position and velocity,
- receiver antenna and instrument (RF and IF) gains, and
- mss.

All these quantities are functions of time. For a moving receiver, the specular point traces out a trajectory in time across the ground known as a track. In this work, two surface models are used for computing the mss: the Katzberg model and the extended WW3 model.

The GPS transmitter and TDS receiver positions and velocities, along with the TDS receive antenna pattern, are furnished by SSTL. However, the instrument gain is not available; in fact, the receiver has automatic gain control (AGC) turned on, so the instrument gain changes with signal level, and this time-varying gain is not recorded. We will subsequently process the DDMs in a way that is not sensitive to the gain value.

The glistening zone is set to 200 km by 200 km. The wind and mss over the area of integration are assumed to be constant.

In addition to the received signal power scattered by the ocean surface, P_s in Equation (1.12), the received signal also contains other components due to radiometric thermal emission by the scene, noise due to the receiver instrumentation (including the antenna), and radio-frequency interference (RFI) [e.g., Chen et al. 2015]. We neglect RFI in this paper. The total received signal (in uncalibrated units of counts) can then be modelled as:

$$C_T(\tau, f) = G_{ri}(P_N + P_s) \ , \tag{3.2}$$

where G_{ri} is the receiver instrument gain (excluding the antenna gain) and P_N is the total noise power. P_N includes the radiometric thermal emission from the scene referred to the output of the antenna and the noise due to receiver instrumentation. P_s is the GNSS-R signal power, given by the ZV model in Equation (1.12). To be precise, P_s is the ensemble mean of the signal power. In practice, there will also be speckle noise present in the measurements. Our model neglects the speckle noise and estimates the ensemble mean.

The noise contributions to the measurements are estimated by examining pixels of the DDM at delay values that correspond to altitudes higher than the surface. As such, these pixels contain no scattered surface signal and P_S=0 can be assumed. In that case, the uncalibrated measurements can be written as

$$C_N = G_{ri}(P_N) \ . \tag{3.3}$$

The pixel in the DDM corresponding to the specular point is found as the pixel with the highest power. With two equations $C_T(\tau_0, f_0) = G_{ri}(P_N + P_s(\tau_0, f_0))$ and $C_N = G_{ri}(P_N)$, we cannot completely resolve the three unknowns, $P_s(\tau_0, f_0)$, G_{ri}, and P_N. It should be noted that the upcoming CYGNSS mission carries an augmented version of the receiver that incorporates calibration targets and fixed receiver gain, so these unknowns can be determined. For TDS, no absolute calibration can be performed and the DDMA observable [Clarizia et al., 2014] is not easily computed. (An observable is a single number characterization of the DDM.)

Because of this, a proxy of the DDMA [Jales, 2015b] known as the SNR is now being used in the TDS community. It is defined by

$$SNR \triangleq \frac{C_T(\tau_0, f_0) - C_N}{C_N} = \frac{G_{ri}\left(P_N + P_s\right) - G_{ri}\left(P_N\right)}{G_{ri}\left(P_N\right)} = \frac{G_{ri}\left(P_s\right)}{G_{ri}\left(P_N\right)} = \frac{P_s}{P_N} \ . \tag{3.4}$$

We see that the SNR observable is independent of gain as desired, but depends on the noise power. Gain varies much faster than the noise power – the dominant factor is changes due to instrument temperature and AGC adjustments.

For our simulations, we only model P_s and do not model the thermal noise. To estimate P_N, we compute the ratio between the measured SNR and the modeled P_s over an entire track. Thus:

$$P_N = \frac{< P_s^{sim} >}{< SNR^{TDS} >} , \tag{3.5}$$

where $<.>$ is the time average operator, P_s^{sim} is the simulated signal power, and SNR^{TDS} is the TDS-measured SNR. This assumes that P_N is constant over the track, and there are no biases to P_s. With P_N known, the simulated SNR can then be computed.

The computation of modelled SNR requires the extraction of a single parameter from the measurements. Note that there are other observables that could alternately be used, such as the DDM volume observable [Marchan-Hernandez et al, 2008]. This observable, fundamentally, makes use of the ratio of the signal powers from DDM bins far away from the specular point to those at or near the specular point. We have considered this observable in our analysis and the results are similar in character to those using the SNR presented in Chapter 4, but they are found to exhibit a larger noise level than the SNR observable. For this reason, we will use an SNR-related observable in the following discussions.

To focus on the effects of sea state, we define the Scaled SNR as:

$$SSNR = SNR \frac{R_t^2 R_r^{\ 2}}{G_{rant}} . \tag{3.6}$$

We neglect scaling corrections for scattering area and incidence angle-dependent Fresnel reflectivity for simplicity and because the measurement geometries present in the TDS sample population (discussed in the next chapter) do not exhibit significant variations.

Lastly, we note that higher mss values (greater roughness) correspond to smaller SNR values.

Chapter 4

Model Comparison with Spaceborne Measurements

In this chapter, we compare spaceborne measurements with our model predictions and with the predictions produced by the Katzberg model. We also discuss of some of the non-local effects that contribute to the scattering measurements predicted by our model.

4.1 Description of Track under Consideration

We analyze one TDS track in this chapter: Track 407 in RD 17 of SSTL's Version 0.3 dataset. This track contains 16 minutes of continuous data, collected by a single receiver channel and a single GPS transmitter (GPS PRN #10 and Receiver Channel #2, per SSTL's numbering conventions). This track exhibits a good variation of coastal and oceanic conditions, as well as a variety of sea states. The track of the specular point is plotted in Figure 31.

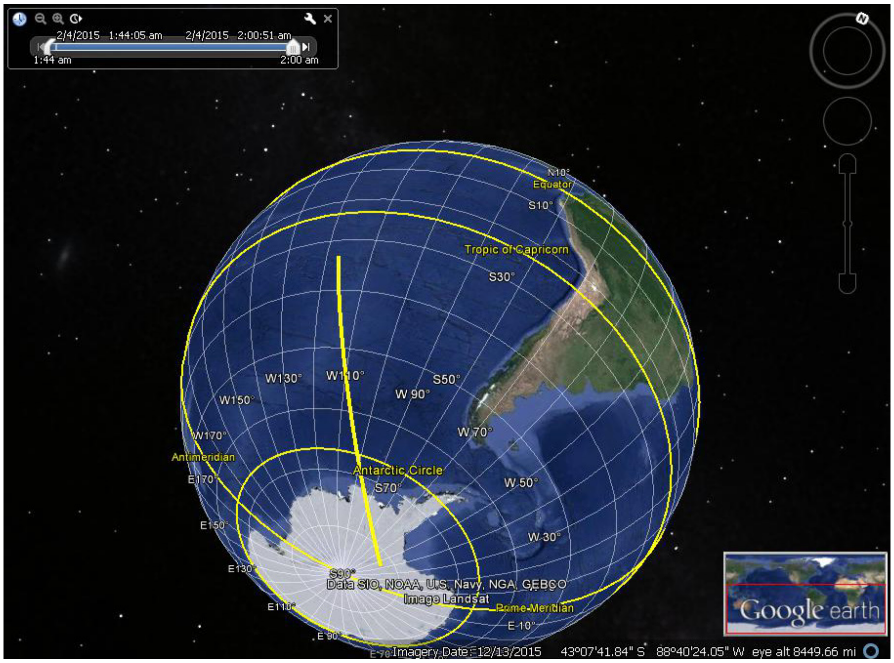

Figure 31: The specular point track for RD17 TR407 is shown as the bold yellow line running from Antarctica into the South Pacific.

The receive antenna gain along the track is plotted in Figure 32. The variation in gain results from the progression of transmitter and receiver locations, and the resulting change in measurement geometry, over time.

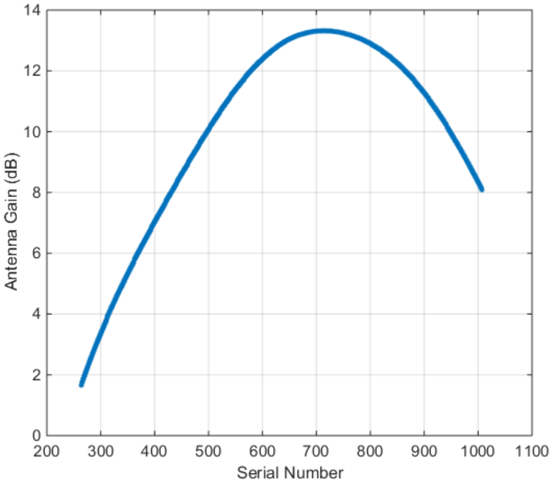

Figure 32 Along-track antenna gain for RD17 TR407.

Because antenna gain can affect the signal quality, we consider only measurements with gain greater than 3 dB in our analysis. In addition, since our interest is in ocean GNSS-R, we filter out any data with its specular point located less than 100 km away from the coast. This is the rationale for restricting the grid size to be 200 km by 200 km as mentioned in Chapter 3. Relative to the specular point, delay and Doppler bins with less than 18 us and 5000 Hz in either direction are considered, and this is the range plotted in the DDMs shown below. The average incidence angle for the track under consideration is 13.8 degrees, which results in a cut-off wavenumber, k_u, of 10.59 rad/m or 59 cm in wavelength.

4.2 Empirical Evidence of Measurement Sensitivity to Significant Wave Height

As seen from Equations (1.8) and (1.10), significant wave height (Hs) is much more sensitive to long waves than the mean square slope. These long waves include swell that is not correlated with wind. In this subsection, we explore the dependence of SSNR (and thus mss) on Hs using TDS measurements.

In Figure 33, U_{10} and Hs are plotted against sample number (SN) for Track 407. Each SN is separated by approximately one second, and, for this track, the specular points of two consecutive measurements are spaced about 6000 m apart. Hs is obtained from spatial interpolation of the same WW3 model run, as WW3 is skillful in modelling Hs. U_{10} comes from the same ECMWF wind reanalysis product that is used to force the WW3 model.

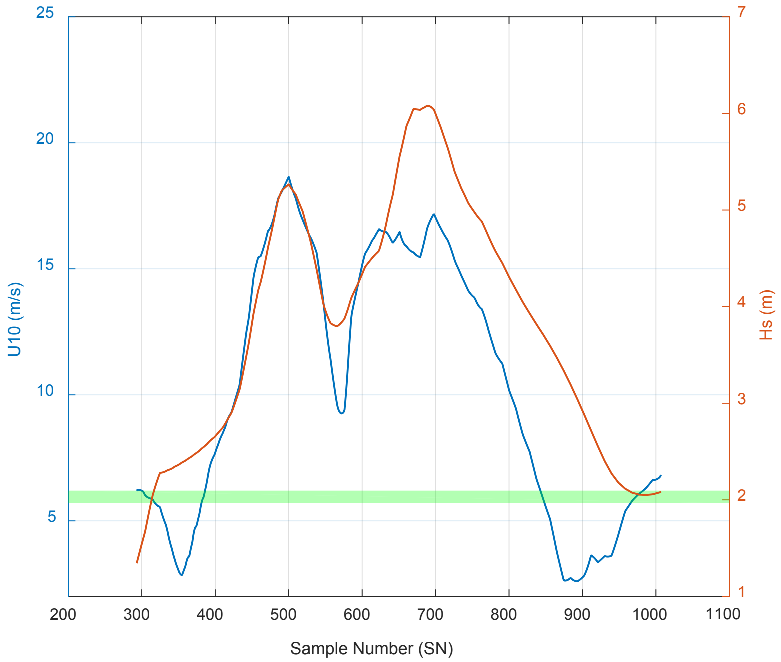

Figure 33: Along track U10 (left axis) and Hs (right axis). The green band denotes a narrow range of U10 values, the relevance of which is discussed in the text.

Although U_{10} exhibits some correlation with Hs, there are many points where they deviate from one another. To control for U_{10} and examine the variance of the SSNR explained by Hs alone, we restrict our analysis to measurements for which U_{10} lies in the narrow range between 5.7 and 6.2 m/s. This region is shaded by a horizontal green band in Figure 33. A scatterplot of the measured SSNR vs. Hs values in this region is shown in Figure 34.

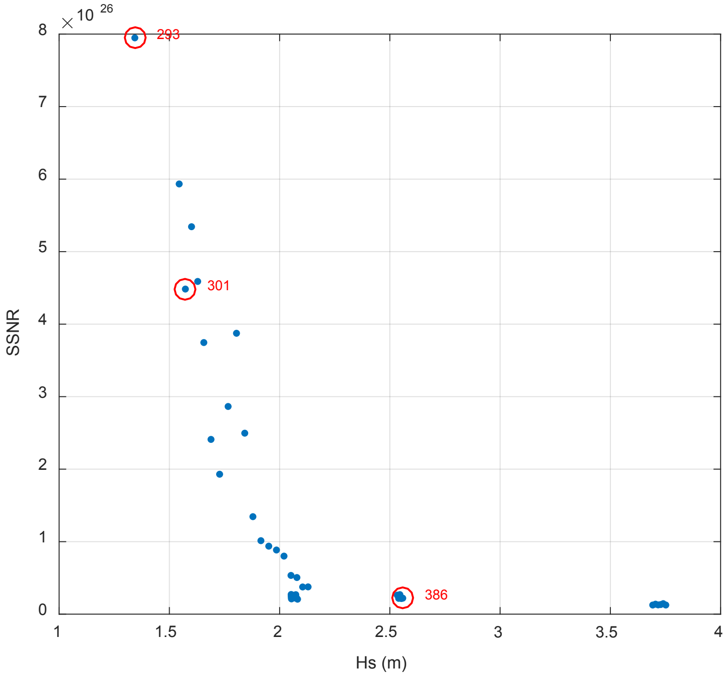

Figure 34: Measurement SSNR observable vs. Hs within a narrow (0.5 m/s) range of U10.

Hs is seen to have a strong effect on SSNR that cannot be accounted for by windspeed. Some scatter is also seen, indicating that SSNR has additional variability explained by neither Hs nor windspeed. In the figure, we have picked three representative measurements; these are circled in red with their SNs indicated. We examine their DDMs in this and the next subsections.

The three DDMs measured by TDS are presented in Figure 35. Both the magnitude and shape of the DDMs change significantly. The magnitude decreases monotonically as Hs increases, which is consistent with theoretical expectations.

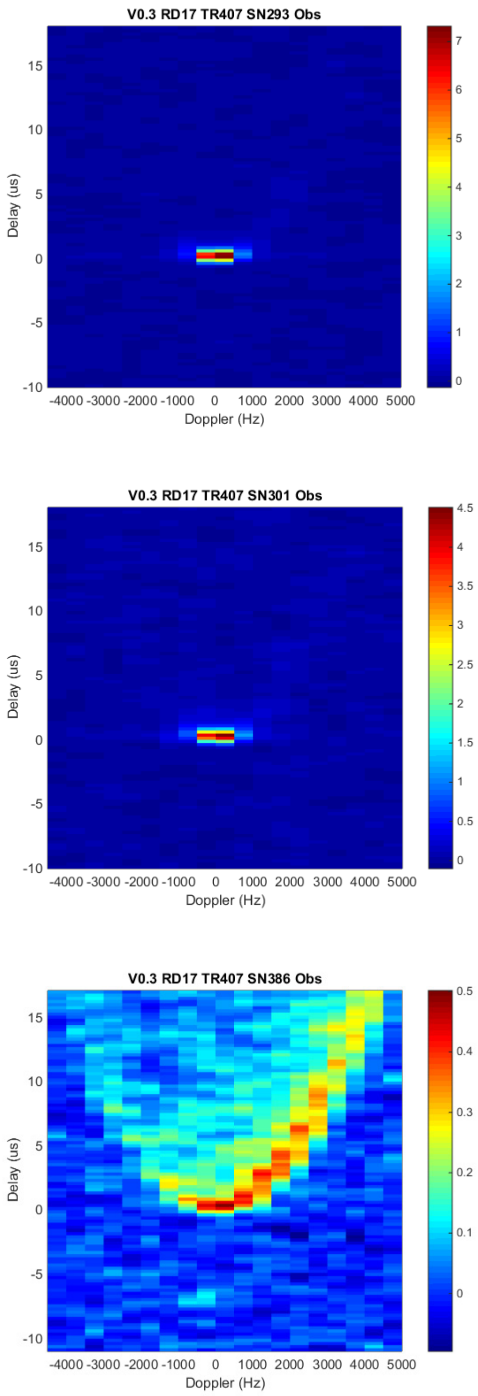

Figure 35: TDS Measurements. Top panel: SN 293 with Hs=1.34 m and U10=6.19 m/s. Middle panel: SN 301 with Hs=1.57 m and U10=6.18 m/s. Bottom panel: SN 386 with Hs=2.13 m and U10=5.70 m/s.

4.3 Modeling the Effect of Significant Wave Height on the Measurement

In this subsection, we examine modelled results and compare them to the measurements in the previous subsection. First, we look at the modelled DDMs of the three cases considered. Second, we look at the dependence on Hs predicted by the models. Lastly, we look at the along-track plots of the SSNR.

Because the windspeed is essentially the same in all three cases, the Katzberg DDMs should all look about the same. This is indeed the case, as seen the modelled DDMs in Figures 36 to 38 (right panels). The left panels show the results of the extended WW3 model. Comparing to the TDS measurements in Figure 35, it is seen that the WW3-based model is much better able to represent the behavior of the measurements, compared to the Katzberg model, in both the magnitude and shape of the DDMs.

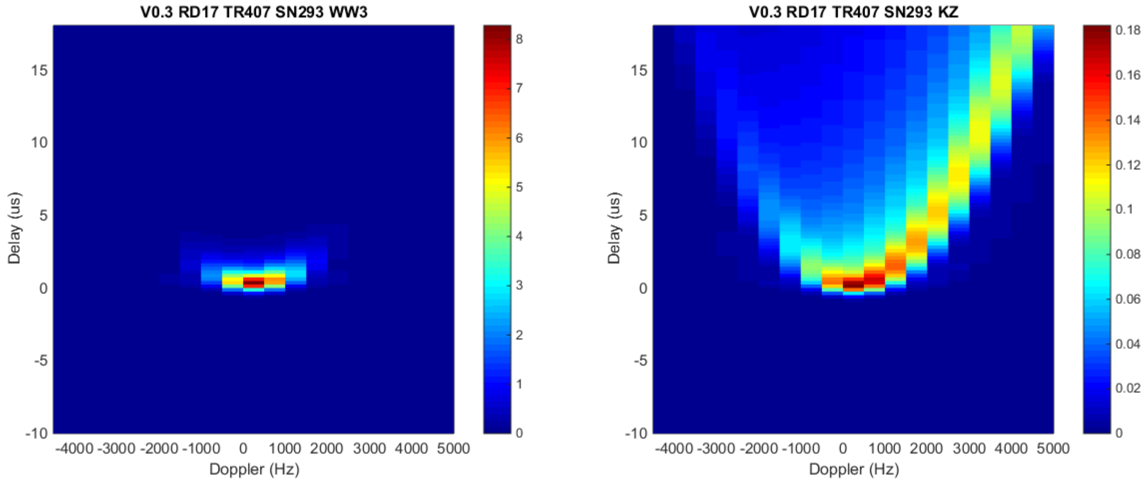

Figure 36: DDMs predicted by the two forward models: WW3 (left) and Katzberg (right) given ocean conditions Hs=1.34 m and U10=6.19 m/s consistent with observation SN 293. Compare to the top panel in Figure 35. For WW3, the DDM is in good agreement with the observation. For Katzberg, both the shape and signal magnitude show large discrepancies.

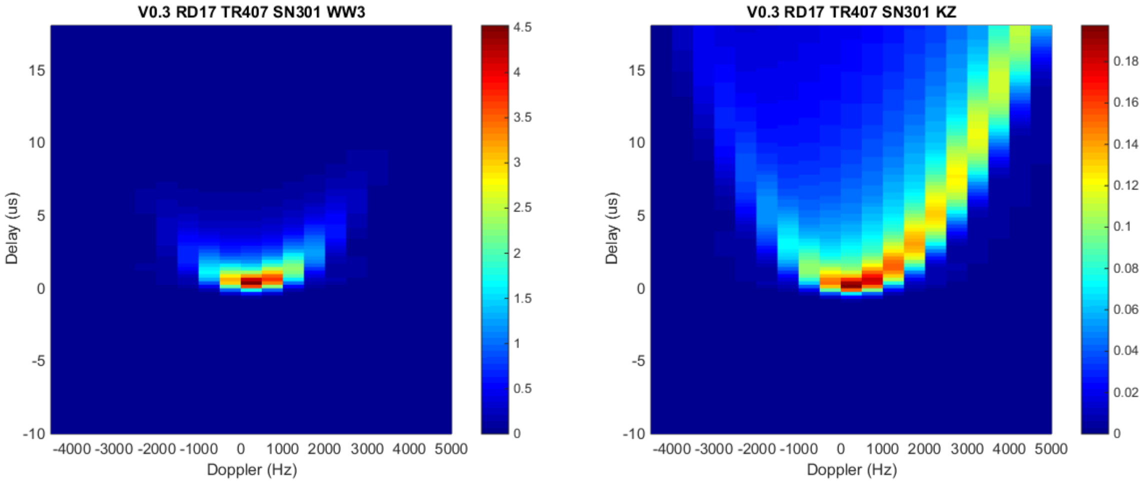

Figure 37: DDMs predicted by the two forward models: WW3 (left) and Katzberg (right) given ocean conditions Hs=1.57 m and U10=6.18 m/s consistent with observation SN 301. Compare to the middle panel in Figure 35. For WW3, the DDM is in good agreement with the observation. For Katzberg, both the shape and signal magnitude show large discrepancies.

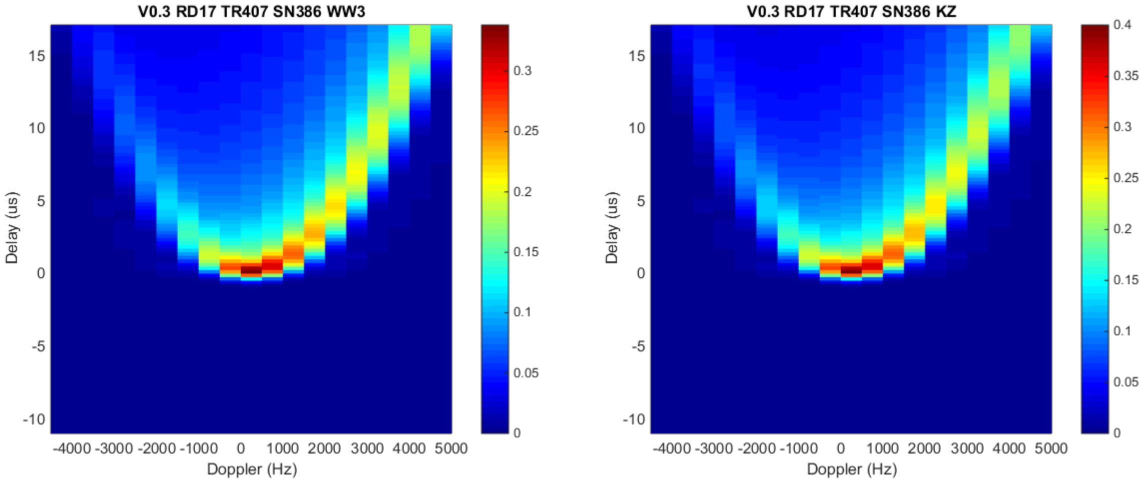

Figure 38: DDMs predicted by the two forward models: WW3 (left) and Katzberg (right) given ocean conditions Hs=2.13 m and U10=5.70 m/s consistent with observation SN 386. Compare to the bottom panel in Figure 35. Both models are both in good agreement with the observations.

We now plot modelled SSNR vs. Hs in Figure 39. These plots reaffirm WW3's skill over the Katzberg model. In particular, significant improvement is seen for low Hs values; these were found to occur at the beginning of the track near the coast. In addition, the Katzberg model demonstrates deficiencies in the “branch” near Hs=3 m and SSNR=3e24; these correspond to very low windspeeds of less than 3 m/s.

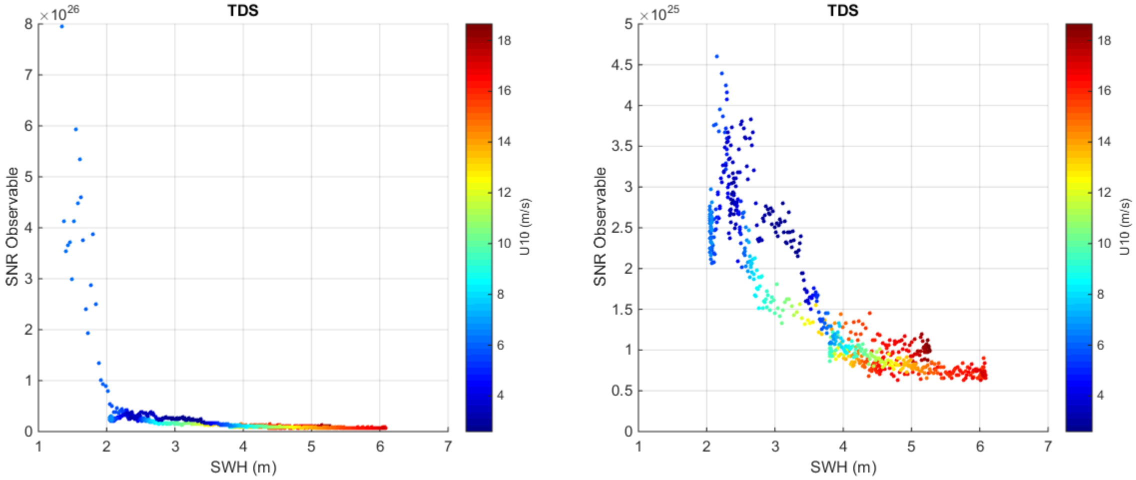

(a)

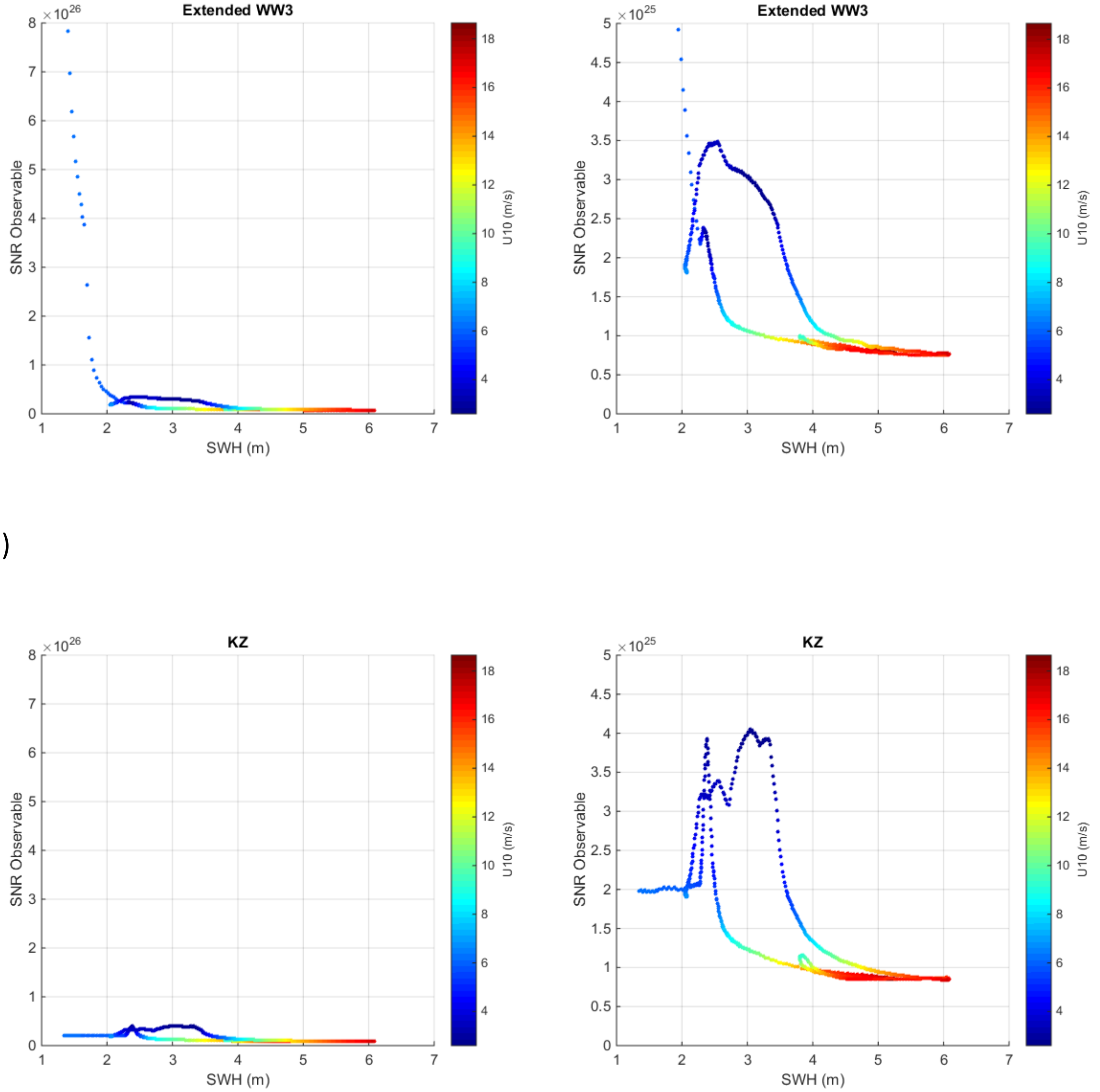

(b)

(c)

Figure 39: SSNR vs. SWH, with U10 colorcoded. The figures in the right column are zoomed in versions of the ones on the left.(a) TDS measurements(b) Extended WW3 (c) Katzberg. Because of the inverse dependence of mss, SNR is much more sensitive to mss changes when mss is small.

To gain additional insight, we plot the SSNR vs. along-track SN for the TDS measurements and both models in Figure 40. This figure should be used in conjunction with Figure 33, which shows the along-track U_{10} and Hs. Using the variance of the difference between simulations and measurements as the metric, the extended WW3 model shows a 68.7% improvement over the Katzberg model over the entire track. The improvements in the coastal region at the start of the track is one significant contributor. If we consider only SN 342 and higher, we still see a 30.2% improvement in the skill of the extended WW3 model. This improvement can largely be attributed to the SNs 850 to 900, for which the windspeed is very low.

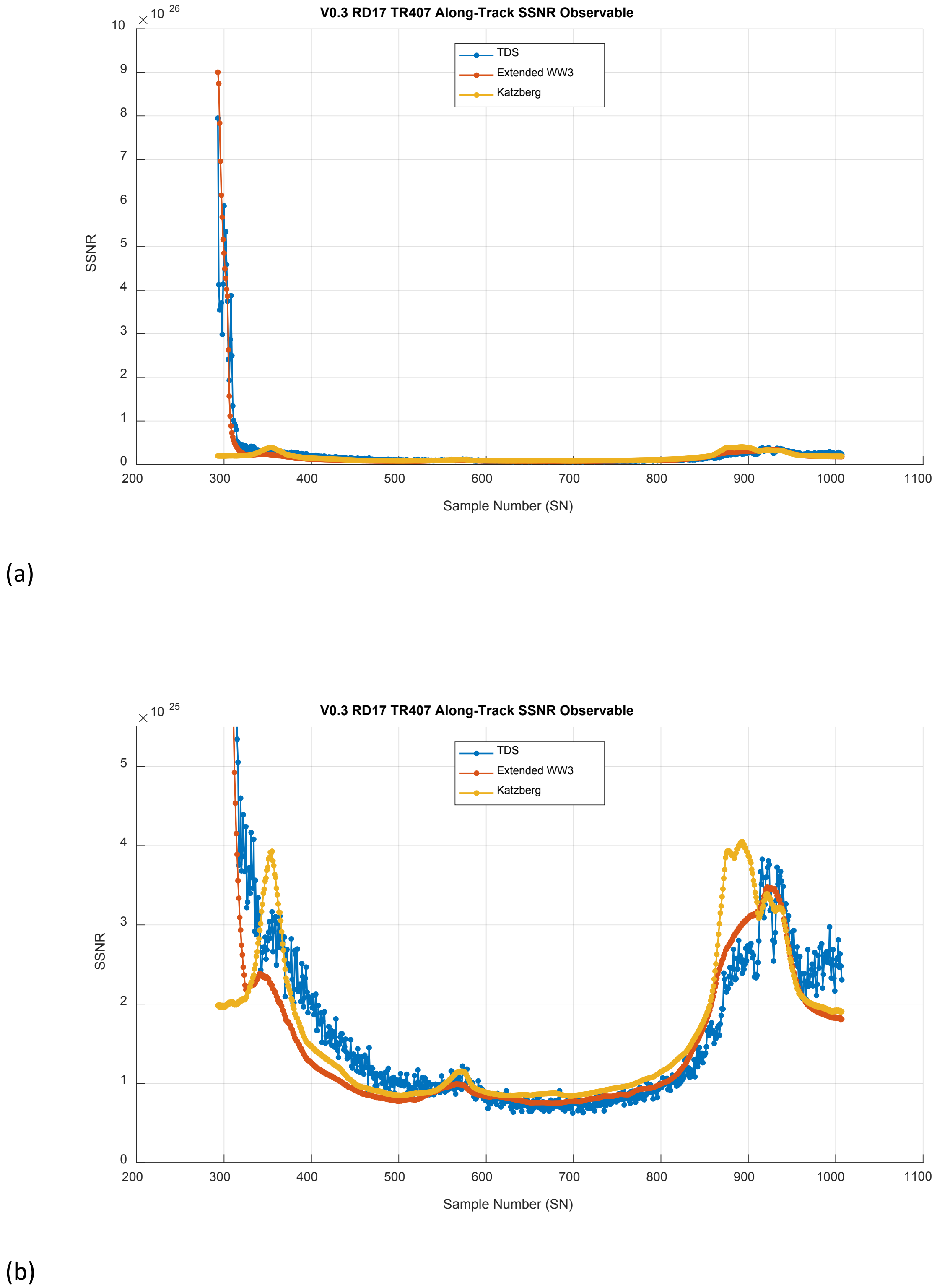

Figure 40. (a) Along track plot of measured SSNR, extended WW3 SSNR, Katzberg SSNR, and scaled Hs and U10. (b) Zoomed in version of a.

Another insight is that despite the attachment of a diagnostic tail, we see WW3 is also responsive to local wind: at SNs from about 900 to 950, Hs is decreasing but windspeed is increasing (see Figure 33). WW3 is able to model the decreasing behavior of the observable correctly.

This analysis shows that the extended WW3 model has considerable skill modelling the GNSS-R observable, derived from its ability to take non-local long waves into account, and in modelling the sea state in low windspeed conditions.

One implication of our results is that much of the sensitivity of the GNSS-R observable to the sea state derives from long and intermediate-scale waves of wavenumber 2 rad/m and lower. This is consistent with predictions of the parametric Elfouhaily model shown in Figure 3. However, it should be noted that this track does not contain winds that change quickly in time. A track with rapid changes in wind temporally and spatially will be able to better evaluate whether the diagnostic tail should be replaced one that has an explicit wind speed dependence. Fast changes in wind may also necessitate that the model be run at a higher spatial and temporal resolution with the corresponding wind speed products.

Lastly, we note that both models underestimate SSNRs between serial numbers 350 and 500, while a slightly positive bias is seen between 600 and 850. These discrepancies can be the result of an overall, constant bias that is not removed before determining and applying the SSNR scale factor in Equation (3.5). Such a bias may be due to errors in the cutoff k_u, or the spectral level. This bias may also contribute to the difference in shapes of the measured and WW3 DDMs shown in Figure 35 and Figure 37.

4.4 Chapter Conclusions

In this work, we have developed a novel GNSS-R forward model that incorporates a third-generation surface wave model. The analysis of one track of TDS measurements, with over 700 consecutive DDMs, shows that this model can account for both local and non-local effects. In contrast to conventional remote sensing techniques, the non-local effects are significant for GNSS-R due to frequency and geometry. The new model demonstrates improved skill over the widely used Katzberg one-to-one windspeed-mss model. Significant improvements are seen in low wave height conditions, in particular. The novelty and strength of our model is derived from the WW3 model, the source terms of which are the fruits of decades of work by the wave modeling, experimental, and remote sensing communities.

4.5 Acknowledgements

The author would like to thank Andrew O'Brien of Ohio State University (OSU) for coding up an optimized version of the ZV model. Designed for CYGNSS, it was modified by Jeonghwan Park of OSU for TDS by incorporating TDS antenna pattern projections. Fabrice Ardhuin of IFREMER is acknowledged for running the year-long WW3 simulation used in this work. In addition, Martin Unwin (SSTL), Philip Jales (SSTL), and Maria-Paola Clarizia are thanked for their input on working with the TDS-1 dataset.

Chapter 5

Conclusion and Future Work

In the context of GNSS-R remote sensing of ocean surface windspeed, the issue of the coupling of wind and waves is far being completely resolved. However, in this thesis, we have conducted studies from empirical and modelling approaches that have led to characterizations, bounds, and a better understanding of some issues in this vast research field. A summary of the work is provided below.

5.1 Contributions

All present techniques of ocean surface wind remote sensing make use of surface wave properties. In the case of bistatic GNSS-R sensors, the mean square slope (mss), integrated over an appropriate spectral band, is the direct observable. We presented an empirical study of the response time of surface wave mean square slope to local wind forcing using data collected over eleven years by forty-six discus buoys moored at a wide variety of locations. The response time is defined as the time lag at which the time dependence of the waves exhibits the highest correlation with that of the local wind speed. The response time at each location is found to be fairly stable, with the time varying between 0.4 and 1.8 hours depending on the location. Examination of long-term statistics reveals response time dependencies on wind speed magnitude, fetch, atmospheric stability, and wavelength.

Because reliable measurements of L-band mss are virtually non-existent, we derived the response time of the mss of longer waves, which are measured reliably by moored discus buoys. We used these empirical results on buoy mss evolution to validate a phase-averaged wave model, and then used the model to estimate the response time of L-band waves. We found the response time of L-band waves to be on the order of 20 minutes. Our finding is in keeping with the previous empirical study by Weissman et al. (1996). These results provide useful insights and bounds for the use of GNSS-R remotely sensed wind data.

Next, using a third-generation wave model that was validated with our buoy measurements, we presented a new, end-to-end forward model for GNSS-R. The model is motivated by recent spaceborne GNSS-R observations that indicate a strong scattering dependence on significant wave height, even after controlling for local wind speed. This behavior is not well represented by the most commonly used GNSS-R scattering model, which features a one-to-one relationship between wind speed and the mean-square-slope of the ocean surface. The new model includes WW3, an anchored spectral tail model, and a GNSS-R electromagnetic scattering model. In comparisons with the spaceborne measurements, the new model is much better able to reproduce the empirical behavior, especially in cases of low wave heights and low windspeeds.

5.1.1 All Journal Publications To-Date

Chen-Zhang, D.D., C. S. Ruf, F. Ardhuin, and J. Park (2016), GNSS-R Non-Local Sea State Dependencies: Model and Empirical Verification, J. Geophys. Res. Oceans. Submitted.

Chen, D. D., C. S. Ruf, and S. T. Gleason (2016), Response time of mean square slope to wind forcing: An empirical investigation, J. Geophys. Res. Oceans, 121, 2809–2823, doi:10.1002/2016JC011661.

Chen, D.D.; Ruf, C.S., “Adaptive Control of Undetected Radio Frequency Interference With a Spaceborne Microwave Radiometer,” in Geoscience and Remote Sensing, IEEE Transactions on , vol.53, no.9, pp.4972-4984, Sept. 2015 doi: 10.1109/TGRS.2015.2414395

Le Vine, D.M.; de Matthaeis, P.; Ruf, C.S.; Chen, D.D., “Aquarius RFI Detection and Mitigation Algorithm: Assessment and Examples,” in Geoscience and Remote Sensing, IEEE Transactions on , vol.52, no.8, pp.4574-4584, Aug. 2014 doi: 10.1109/TGRS.2013.2282595

5.1.2 All Peer-Reviewed Proceedings Publications To-Date

Morris, M.; Chen, D.D.; Ruf, C. S., “Earth Antenna Temperature Variability for CYGNSS,” in IEEE Geoscience and Remote Sensing Symposium (IGARSS), 2016. Accepted.

Chen, D.D.; Ruf, C., “A novel method to estimate the RFI environment,” in Geoscience and Remote Sensing Symposium (IGARSS), 2014 IEEE International , vol., no., pp.215-218, 13-18 July 2014 doi: 10.1109/IGARSS.2014.6946395

Le Vine, D.M.; de Matthaeis, P.; Ruf, C.; Chen, D.; Dinnat, E.P., “Aquarius RFI detection and mitigation,” in Geoscience and Remote Sensing Symposium (IGARSS), 2013 IEEE International , vol., no., pp.1798-1800, 21-26 July 2013 doi: 10.1109/IGARSS.2013.6723148

Chen, D.D.; Gleason, S.; Ruf, C.; Adjrad, M., “Spectral dependence of the response time of sea state to local wind forcing,” in Geoscience and Remote Sensing Symposium (IGARSS), 2012 IEEE International , vol., no., pp.3776-3779, 22-27 July 2012 doi: 10.1109/IGARSS.2012.6350495

Ruf, C.; Chen, D.; Le Vine, D.; de Matthaeis, P.; Piepmeier, J., “Aquarius radiometer RFI detection, mitigation and impact assessment,” in Geoscience and Remote Sensing Symposium (IGARSS), 2012 IEEE International , vol., no., pp.3312-3315, 22-27 July 2012 doi: 10.1109/IGARSS.2012.6350595

5.1.3 Selected Conference Presentations

D. D. Chen and P. A. Hwang*, “L-band GNSS-R Retrieval Algorithms for Tropical Cyclones Based on Wind-Wave Growth Similarity,” AMS 32nd Conference on Hurricanes and Tropical Meteorology, Apr. 2016, San Juan, PR, USA.

David D. Chen*, Christopher S. Ruf, and Scott T. Gleason, “Wavenumber Dependence of the Response Time of Mean-Square Slope to Wind Forcing,” AGU Ocean Sciences Meeting 2016, New Orleans, LA, USA.

C. Ruf, D. Chen*, and P. de Matthaeis, “The Aquarius RFI Detection Algorithm Parameter Tuning Problem,” in IEEE International Geoscience and Remote Sensing Symposium (IGARSS) 2013, July 2013, Melbourne, Australia.

C. Ruf*, D. Chen, J. Piepmeier, and D. Levine, “Aquarius Radiometer RFI Detection, Characterization And Mitigation,” in 12th Specialist Meeting on Microwave Radiometry and Remote Sensing of the Environment (MICRORAD 2012), March 2012, Frascati, Italy.
* Presenting Author

5.1.4 Selected Technical Reports

David D. Chen and Chris Ruf, “An Antenna Temperature Model for CYGNSS,” June 2015

David D. Chen and Chris Ruf, “The Wideband Radiometer (WBRad): Design, Characterization, and Usage,” December 2013

David D. Chen and Chris Ruf, “Characterization of the Wideband Digital Back End (WB-DBE) Subsystem,” July 2011

5.2 Future Work

5.2.1 Augmentations and Applications of the End-to-End Forward Model

A GNSS-R forward model incorporating a third-generation wave model has many areas where it can be improved upon. Some of the future improvements to the forward model include:

- The retrieval of mss from the measurements, and taking into account scattering area and Fresnel reflectivity,

- Modelling of anisotropic seas with two mss components and a more sophisticated pdf of slopes, in effect creating a tighter coupling between the scattering and wave models,

- Relaxation of assumption of uniformity of wind and mss fields over the 200 km by 200 km glistening zone,

- Augmenting the scattering model by taking the coherent scattering component into account for low windspeeds,

- Inclusion of the effects of wave-current interaction, atmospheric stability, and surfactants

- Usage of fully coupled atmospheric, ocean, and wave models.

The availability of CYGNSS data will undoubtedly be very beneficial to the further development of the end-to-end forward model. There are several aspects of CYGNSS data that make it helpful:

1. Volume of data. CYGNSS is a constellation of 8 satellites with 4 simultaneous measurements. This means a large volume of data will be available in a diverse set of conditions.
2. Signal-to-noise ratio (SNR). As a result of higher antenna gain and lower altitude, CYGNSS data are expected to have a higher SNR than the available TDS-1 data.
3. Absolute calibration. With absolute power calibration, observables like the DDMA can be used, instead of the SSNR observable used in this thesis. Not only is the DDMA expected to be less noisy, the mss can also be readily retrieved, which is more closely coupled to the sea state under study.
4. If collocated measurements of wave spectra (or mss with known wavenumber bounds) are available, the accuracy of the effective cutoff frequency of low-pass-filtered mss k_u used in the mss retrieval can be assessed.

To understand the underlying physical phenomena modelled by WW3 that allow it to produce better long-wave mss, it would be helpful to examine the two-dimensional wave spectra, as well as the source term spectra. The insights may lead to the development of ancillary parameters that can be helpful in constructing better wind retrieval algorithms for GNSS-R.

The model developed here can also be used to improve our understanding of surface waves with GNSS-R measurements. Possibilities include the tuning of the spectral tail and development of appropriate source terms. The model is also expected to be helpful in the design of future GNSS-R missions and experiments.

5.2.2 Investigation of Wind-Wave Coupling for Hurricanes

Wind waves in tropical cyclone conditions is presently an active area of research [e.g., Hwang, 2016; Chen and Hwang, 2016; Fan and Hara, 2012]. One approach of modelling hurricane surface waves is to use WW3 driven by high-resolution winds and currents. One outcome of this study for GNSS-R is that through the use of ancillary data (which may be introduced in the retrieval process), a more precise MSS-windspeed relationship can be obtained after controlling for these conditions, leading an increased accuracy of the retrieved windspeed. For hurricanes, ancillary parameters under consideration include the location of the eye, velocity vector of the eye, radial distance from the eye, and distance from the coast. As an example, we consider a snapshot of Hurricane Ivan when it is in the middle of the Gulf of Mexico on Sep. 15, 2004 at 03:00. The wind field and the associated MSS-windspeed scatter plot obtained from a WW3 simulation are shown in Figure 41 below.

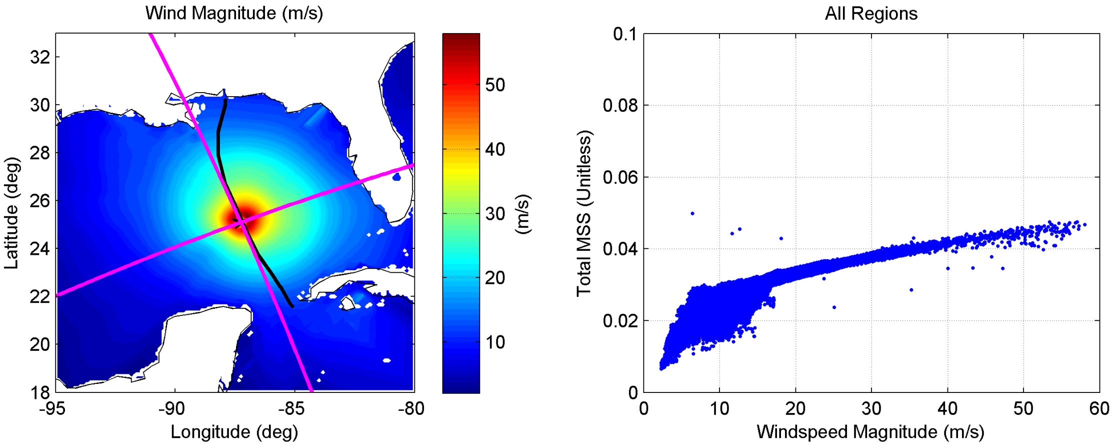

Figure 41: Ivan wind field at 2004 09 15 03:00. The storm track is shown in black and the magenta lines delineate the boundaries of the 4 quadrants under consideration (left). Scatter plot of MSS vs. windspeed (right).

The storm can be divided into four quadrants based on the direction of movement of the storm, with the storm track obtained from the NOAA HURDAT2 Best-Track dataset. To focus on the storm, locations more than 634 km away from the eye, or within 108 km of coast are not considered. The result for the north-east quadrant is shown below:

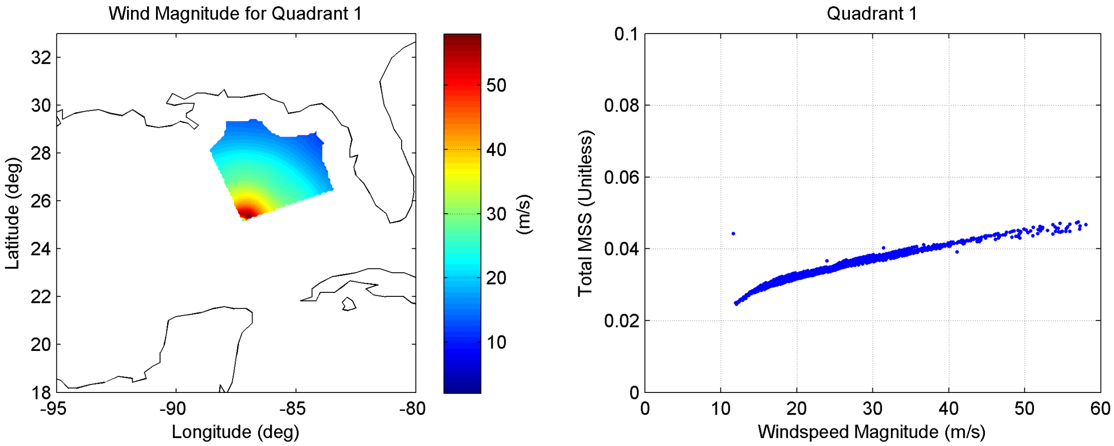

Figure 42: Portion of wind field included the northeast storm quadrant (left), and the corresponding scatter plot of MSS vs. windspeed (right).

It is observed that by subsetting the wind and MSS fields with respect to storm quadrant, distance from the eye, and distance from the coast, much scatter in the MSS-windspeed relationship can be removed. Future work could include applying the same subsetter to other storms to assess the repeatability of this characteristic.

5.2.3 Laboratory Measurements of Gravity-Capillary Waves

In-situ wavenumber spectrum measurements of intermediate scale waves are very challenging. The usage of moored buoys is an infeasible technique; the short waves are susceptible to Doppler shifting by currents and longer waves, which means the linear dispersion relation specified in Chapter 1 can no longer be applied to convert frequency spectra to wavenumber spectra.

One method of alleviating the Doppler shift issue is to use a free-floating, current following structure with capacitance wave gauges mounted in the middle region. The use of more than one gauge can be helpful in the derivation of directional spectra. As with any technique, issues remain: short waves “bound” or phase-locked to longer waves [e.g., Plant et al., 1999] may still not satisfy the linear dispersion relation. Also, the free floating structure may come under the effect of wind, and “sail” with the wind instead of floating with the current.

Here, we discuss a conceptually simple experiment of optical imaging of waves that may be executed in an indoor wind-wave tank facility. The issues with this method are outlined in Section 5.2.3.4. It is expected, however, that some of these issues may be of less concern for longer, gravity-capillary waves than for centimeter capillary waves.

5.2.3.1 An Example of the Facility

Many wave-tank facilities exist in the United States alone. The Air-Sea-Interaction Wind-Wave Facility at University of Michigan's Marine Hydrodynamics Lab (MHL) is one such facility; it features a 35-m long wind-wave tank fitted with glass panels on the side and on the bottom:

Figure 43: Downwind view of the wind-wave tank from. The suction fan providing the wind forcing can be seen at the end.

A suction fan at one end induces the air flow. The tank is covered at the top by glass or wood panels. Some specifications are listed below:

Table 4: MHL Wave Tank Facility Specifications

Basin Length	35 meters
Basin Width	0.7 meters
Maximum water depth	1.2 meters
Wind speed range	2 m/s to ~15 m/s

Computer controlled wedge wave generator	10 Hz maximum
Width of each glass panel	44 inches = 1.12 meters
Height of each glass panel	55 inches = 1.40 meters

The height of the tank increases downwind to accommodate the growing boundary layer. Most glass panels are tampered for strength. These tampered glass panels refract light differently than normal untampered glass. Only 2 glass panels are untampered; these have horizontal bars for support, as indicated by the red arrow:

The horizontal bar is 2 inches in thickness, and it's positioned 14 inches from the bottom and 38.5 inches from the top of the glass panel.

Anemometers can be deployed to measure the wind speed. Multiple fast-sampling capacitance wave gauges can also be deployed by mounting them on the ceiling of the tank to infer directional wave spectra. Although not of particular use to us, we note in passing there are computer-controlled wedges on both ends of the tank that can generate mechanical waves up to 10 Hz.

5.2.3.2 Measurement Technique

This technique makes spatial measurement by optically imaging the wave profile as seen through the glass sidewall. The optical image is processed to construct a histogram of upwind-downwind slopes. A detailed procedure is as follows.

A camera, an anemometer, and two wave gauges are deployed at a fixed location downwind. At the same time the suction fan is activated, the camera, anemometer, and wave gauges begin recording data. The synchronization is provided by a single computer. The camera captures the wave elevation seen through the glass sidewall. This is called a wave profile.

Figure 44: Sample photograph to derive wave profile

The camera would be stabilized by a tripod. Sufficient lighting, and a high shutter speed would minimize the noise due to blur. A normal camera light flash, though, may cause undesirable reflections from the glass that makes the image difficult to digitize (discussed later). A laser sheet may need to be used to aid in the image capture and subsequent processing.

After a sufficiently long period of time, another photo is taken. Waves of different frequencies propagate at different speeds, so if the next photo is taken immediately after the previous one, some longer waves would have passed while some shorter waves seen in the previous photo would still be present. This may lead to a biased sampling and an erroneous PDF. Therefore, the waiting period should be long enough to ensure consecutive photos are independent.

The photograph is then digitized to produce the water elevation as a function of position. A laser sheet or LEDs may be used underneath the tank to accentuate the wave elevation, and facilitate the subsequent image processing. This technique has been used by Tian and Choi [2013] to study wind effects on mechanically generated waves, and to study mechanically generated waves in general [e.g., Tian and Perlin, 2008].

We assume the surface elevation in the photograph is statistically stationary (over 1.12 meters). The slope as a function of position is estimated by taking the elevation's first derivative. A histogram of the slope is constructed from all the photos to estimate the PDF. The experiment can be repeated until the statistics converge.

For CYGNSS, it believed that waves with wavenumber 9.54 rad/m and below dominate the quasi-specular scatter. To include only these waves, we can apply a low-pass FFT filter to the elevation signal or the slope signal.

The benefit of the spatial technique is that few assumptions need to be made and thus the errors are expected to be small. No specialized instrument is required, barring the need for a high power laser sheet and optical lenses at the bottom of the tank. Even without a specialized laser, the image can be digitized manually. The very small scale noise (due to unavoidable hand jitters) can perhaps be removed by low-pass filtering. Also, high-resolution and high-speed cameras (such as Go-Pro Cameras) are readily available and affordable due to high market demand.

5.2.3.3 Other uses of the dataset

In addition to an investigation of the PDF, the dataset collected could be useful for investigation of other topics such as:

- Wind wave growth: the measurements need to be taken before the reflected waves arrives.

- The upwind wave spectrum can be derived and compared to modelled results, and if some function form of the full wave spectrum is assumed, it too can be estimated.

- By using wave probes, these measurements can also yield PDFs and wave spectra. Comparison with the results from the photographs will reveal the errors resulting from the Doppler effect.

In terms of instrumentation and techniques, it would be interesting to compare to the results of other instruments (like slope gauges) by deploying them at the same time.

5.2.3.4 Issues and Limitations

1. Meniscus effects of the glass imply the measurement technique should not be applied to short, capillary waves. In addition, the effects of the wall on directional waves should be considered.
2. Fetch is limited to the dimensions of the tank.
3. Depending on the wave phenomena under study, reflections from the end of the tank may pose an issue. A gently sloping beach or horse hair may decrease the reflected levels, but these techniques are, of course, never perfect. One may of course make measurements in a short period before significant reflections arrive. On the other hand, these reflections may allow the study of conditions where a specific type of swell is superposed on the wind waves.
4. There have been studies showing in-situ measurements in the open ocean sometimes show significant differences compared to those made in the lab.
5. The crosswind PDF cannot be derived using this technique.

Appendix A

Two-Dimensional Spectra and PDFs

In our modelling work, we assumed isotropic (non-directional seas) to focus on first-order effects, so it was not necessary to present two-dimensional formulations. We present some of those concepts here; these equations may be useful for further work on the forward model.

A.1 Directional Mean Square Slopes

At any given instant in time, the surface elevation of a non-breaking wave field can be represented by a two-dimensional scalar function, $\eta(x, y)$, where x and y are the two horizontal Cartesian spatial coordinates. Their orientations are arbitrary and immaterial to the present formulation, but it is common to select x as the eastward and y as the northward directions. The two components of the surface slopes are then defined as the two partials of η, the entries in the gradient vector or Jacobian of η:

$$\begin{aligned} s_x &\triangleq \frac{\partial \eta}{\partial x} \\ s_y &\triangleq \frac{\partial \eta}{\partial y} \end{aligned},$$

where s_x is the eastward slope, and s_y is the northward slope.

If we let s_{max} be the maximum slope (the slope in the direction of the gradient vector), and θ_{max} be the angle (with respect to the x-axis) of this max slope, then

$$\begin{aligned} s_x &= s_{max}\cos(\theta_{max}) \\ s_y &= s_{max}\sin(\theta_{max}) \end{aligned},$$

which is just a conversion between Cartesian and polar representations of the gradient vector of the scalar surface elevation function or field.

The randomness of s_x and s_y is induced by the surface elevation random process. Let us for now consider η to be stationary such that s_x and s_y are random variables independent of time. Then, mss_x and mss_y are defined simply to be the second moment of the slope processes [Massel, 2013, p. 153]

$$\begin{aligned} mss_x &\triangleq <(\frac{\partial\eta}{\partial x})^2>=<s_x{}^2>=\sigma_x{}^2 \\ mss_y &\triangleq <(\frac{\partial\eta}{\partial y})^2>=<s_y{}^2>=\sigma_y{}^2 \end{aligned}, \tag{A.1}$$

where σ denotes standard deviation of the corresponding subscripted random variable. The last equality holds because the first moments $<s_x>=<s_y>=0$.

The upwind and crosswind slopes are just the directional derivatives of η in the appropriate directions, similar to the definitions of eastward and northward slopes. Letting s_u be the upwind slope and s_c be the crosswind slope,

$$\begin{aligned} s_u &\triangleq J\hat{u}_u \\ s_c &\triangleq J\hat{u}_c \end{aligned},$$

where $J = \begin{pmatrix} s_x & s_y \end{pmatrix}$ is the Jacobian (row) vector and $\hat{u}$ is the (column) unit vector in the subscripted direction.

The mean square slope in the upwind and crosswind directions are defined as one would expect

$$\begin{aligned} mss_u &\triangleq < s_u^{\ 2} > = \sigma_u^{\ 2} \\ mss_c &\triangleq < s_c^{\ 2} > = \sigma_c^{\ 2} \end{aligned} .$$

If we let θ_u be the polar angle of upwind direction in the eastward-northward Cartesian coordinate system ($\theta_u = 0^\circ$ is East while $\theta_u = 90^\circ$ is North),

$$s_u = s_x \cos(\theta_u) + s_y \sin(\theta_u) \ .$$

Similarly, $s_c = s_x \cos(\theta_c) + s_y \sin(\theta_c)$. With the crosswind direction is defined such that crosswind and upwind/downwind conforms the right-hand-rule, that is, $\theta_c = \theta_u + 90^\circ$,

$$s_c = -s_x \sin(\theta_u) + s_y \cos(\theta_u) \ .$$

In matrix form,

$$\begin{bmatrix} s_u \\ s_c \end{bmatrix} = \begin{bmatrix} \cos(\theta_u) & \sin(\theta_u) \\ -\sin(\theta_u) & \cos(\theta_u) \end{bmatrix} \begin{bmatrix} s_x \\ s_y \end{bmatrix} . \tag{A.2}$$

The square conversion matrix above can be identified as a rotation matrix, which is always invertible (for all angles). The inverse is then

$$\begin{aligned} s_x &= s_u \cos(\theta_u) - s_c \sin(\theta_u) \\ s_y &= s_u \sin(\theta_u) + s_c \cos(\theta_u) \end{aligned} . \tag{A.3}$$

The reason for introducing upwind and crosswind directions is that s_u and s_c can be assumed to be uncorrelated. Upon substituting (A.3) into (A.1), the covariance term vanishes, and

$$\begin{aligned} mss_x &= mss_u \cos(\theta_u)^2 + mss_c \sin(\theta_u)^2 \\ mss_y &= mss_u \sin(\theta_u)^2 + mss_c \cos(\theta_u)^2 \end{aligned} .$$

In matrix form,

$$\begin{bmatrix} mss_x \\ mss_y \end{bmatrix} = \begin{bmatrix} \cos^2(\theta_u) & \sin^2(\theta_u) \\ \sin^2(\theta_u) & \cos^2(\theta_u) \end{bmatrix} \begin{bmatrix} mss_u \\ mss_c \end{bmatrix} .$$

Its inverse is

$$\begin{bmatrix} mss_u \\ mss_c \end{bmatrix} = \frac{1}{\cos^4(\theta_u) - \sin^4(\theta_u)} \begin{bmatrix} \cos^2(\theta_u) & -\sin^2(\theta_u) \\ -\sin^2(\theta_u) & \cos^2(\theta_u) \end{bmatrix} \begin{bmatrix} mss_x \\ mss_y \end{bmatrix} .$$

As an aside, we note that

$$mss_x + mss_y = mss_u \cos(\theta_u)^2 + mss_c \sin(\theta_u)^2 + mss_u \sin(\theta_u)^2 + mss_c \cos(\theta_u)^2 = mss_u + mss_c \ .$$

A.2 Two-dimensional PDF of Slopes

The joint probability distribution of the two components of slopes, $P(s_x, s_y)$, is of special interest in GNSS-R. Radar backscatter near normal incidence and forward scatter are both dependent on the PDF of slopes. In particular, the baseline mss retrieval algorithm of Cyclone Navigation Satellite System (CYGNSS), to be launched in late 2016, needs to have prior knowledge about the PDF of slopes (currently assumed to be a 2-D Gaussian) in order to retrieve the mss.

There have been many studies of the probability density function (PDF) of surface wave slopes. Cox and Munk [1954, JMarRes and JOS] took a series of photographs from flight campaigns in Monterey, CA and then in Maui, HI. They carefully corrected for the motion of the plane, and analyzed the distribution of reflected sunlight about the specular point, from which the tilts of facets can be inferred. Hwang and Shemdin [1988] provides a good review of this pioneering work. Cox and Munk's results remain, to this date, the gold standard in characterizations of PDF of slopes. Liu et al. [1997] proposed a new form of the slope PDF which generalizes the Gaussian and Gram Charlier PDFs introduced by Cox and Munk. It is parameterized by the "peakedness coefficient", which depends on some wave properties. This new PDF is shown be successful in predicting the measured cross-section of a C-band scatterometer. Many others [e.g., Ross et al. 2007; Hughes et al., 1977; Plant, 2003] have measured and attempted to explain the PDF of slopes. All studies suggest the PDF is Gaussian to the first order (especially the crosswind PDF).

Following our formulation in the previous subsection, because of s_u and s_c are assumed to be uncorrelated, the joint PDF is just the product of the univariate PDFs, which we assume to be Gaussian. The two-dimensional PDF can then be expressed in matrix form as:

$$\begin{aligned} P(s_u, s_c) &= \frac{1}{2\pi\sqrt{mss_u mss_c}} \exp\left\{-\frac{1}{2}\left(\frac{s_u^2}{mss_u}+\frac{s_c^2}{mss_c}\right)\right\} \\ &= \frac{1}{2\pi\sigma_u\sigma_c} \exp\left\{-\frac{1}{2}\left(\frac{s_u^2}{\sigma_u{}^2}+\frac{s_c^2}{\sigma_c{}^2}\right)\right\} = \frac{1}{2\pi\sigma_u\sigma_c} \exp\left\{-\frac{1}{2}\begin{bmatrix} s_u \\ s_c \end{bmatrix}^T C^{-1} \begin{bmatrix} s_u \\ s_c \end{bmatrix}\right\}, \end{aligned} \tag{A.4}$$

with $C = \begin{bmatrix} {\sigma_u}^2 & 0 \\ 0 & {\sigma_c}^2 \end{bmatrix}$ being the covariance matrix, with inverse $C^{-1} = \begin{bmatrix} 1/{\sigma_u}^2 & 0 \\ 0 & 1/{\sigma_c}^2 \end{bmatrix}$.

As an aside, we note that the level curve of the $P(s_u, s_c)$ at $\max(P)e^{-\frac{1}{2}}$ is an ellipse with mss_u and mss_c as radii along the principal axes.

It is straightforward to express this PDF in terms of s_x and s_y, the eastward and northward slopes, if needed. For the GNSS-R forward model, the inputs to the PDF depends on the coordinate system used by the KA-GO cross section coefficient. Given s_x and s_y, we can invoke Equation A.2 to get s_u and s_c, which can then be inserted in (A.4) to arrive at the desired expression.

Of course, once is the PDF is specified, the mean square slope in any direction can be computed; for example, by definition,

$$mss_x = \int_{-\infty}^{\infty} (s_x - \overline{s_x})^2 \int_{-\infty}^{\infty} P(s_x, s_y) ds_y ds_x$$

gives the eastward mean square slope. $\overline{s_x} = 0$ as noted previously.

A.3 Two-dimensional Spectra

Surface waves are often characterized statistically by different types of wave spectra. The connection between wavenumber wave spectra and PDF of slopes is through the slope variance, commonly known as the mean squared slope (mss). Many different types of wave spectra exist [Elfouhaily et al., 1997, Appendix]. If we let $\Psi(k_x, k_y)$ be the 2-D wavenumber elevation spectrum with units of m^4, then the upwind, mss_x, can be expressed as:

$$mss_x = \int_{-\infty}^{\infty} k_x{}^2 \int_{-\infty}^{\infty} \Psi(k_x, k_y) dk_y dk_x \ .$$

We can also express the wavenumber elevation spectrum in polar coordinates, as is commonly done in wave modelling literature, such that:

$$\Psi(k_x, k_y) dk_y dk_x = \Psi(k, \phi) k dk d\phi \ ,$$

where $k = \sqrt{k_x{}^2 + k_y{}^2}$ and ϕ is the polar argument.

Thus, $\Psi(k,\phi)$ also have units of m^4. And it can be shown that:

$$mss_x = \int_0^{\infty} \int_{-\pi}^{\pi} k^2 \cos^2(\phi) k \Psi(k, \phi) d\phi dk$$

Often, we will use the directionally integrated one-dimensional wavenumber spectrum, $S(k)$, with units of m^3, defined as:

$$S(k) = \int_0^{2\pi} \Psi(k, \phi) k d\phi \ .$$

It then follows

$$mss = \int_0^{\infty} k^2 S(k) dk \ ,$$

where mss is the sum of the mss components:

$$mss = mss_x + mss_y = mss_u + mss_c \ .$$

Our scattering model described in Section 3 is based on quasi-specular scatter from large-scale facets. Thus, the upper limit of the mss integral must be adjusted to compute the low-pass filtered mss, discussed previously.

Most wave models output the wave spectra, from which mss can be extracted and used to parameterize the PDF of slopes.

Appendix B

Buoy Stations Used for Temporal Response Time Determination and Their Properties

Station Number	Latitude (Deg. North)	Longitude (Deg. East)	Ocean Depth (m)	Distance to Coast (km)	Average Wind Speed (m/s)	Wind “From” Direction (Deg. Clockwise from North)	Average Air Temperature (Celsius)	Average SST (Celsius)
41002	31.86	-74.84	4091	342	6.89	169	23.40	22.52
41040	14.52	-53.02	4898	708	6.98	74	27.74	26.99
41041	14.33	-46.08	3587	1233	7.1	80	26.82	26.18
41043	21.02	-64.85	5286	256	6.26	94	27.32	26.44
41044	21.58	-58.63	5418	543	6.13	86	27.07	26.13
41046	23.89	-68.37	5570	386	6.07	96	27.01	26.02
41047	27.52	-71.48	5291	482	6.1	79	25.85	24.57
41048	31.87	-69.57	5358	447	6.82	225	23.93	22.51
41049	27.54	-62.95	5433	553	5.65	98	25.66	24.55
42002	26.09	-93.76	3063	341	6.44	129	25.63	25.29
42039	28.74	-86.01	293	122	5.63	104	24.86	22.58
42055	22.2	-94	3637	304	6.47	106	27.33	26.48
42056	19.8	-84.86	4569	213	6.6	83	28.38	27.40
42057	17	-81.5	423	225	6.71	75	28.35	27.83
42058	14.92	-74.92	4158	356	8.7	82	27.98	27.81
42059	15.18	-67.56	4780	307	7.32	89	28.23	27.76
42060	16.33	-63.24	1572	83	6.67	76	28.22	27.51
44018	42.14	-69.71	225	31	6.4	180	10.57	9.92
46002	42.61	-130.49	3454	487	7.08	354	13.67	13.07
46005	45.96	-131	2748	504	7.38	329	13.30	12.46
46006	40.75	-137.46	4235	1096	7.3	180	14.86	14.00
46011	34.96	-121.02	454	30	5.59	322	13.51	13.16
46012	37.36	-122.88	237	35	5.88	325	12.87	12.36
46014	39.24	-123.97	398	16	5.93	337	11.71	11.53
46015	42.76	-124.83	456	22	6.94	360	11.41	11.21

46022	40.72	-124.53	357	22	5.88	356	11.76	11.90
46025	33.75	-119.05	887	28	3.61	278	16.93	15.87
46028	35.75	-121.88	1138	40	6.74	325	13.76	13.31
46035	57.03	-177.74	3706	444	9.04	0	4.36	3.29
46042	36.79	-122.45	2001	35	5.98	325	13.28	12.80
46047	32.4	-119.54	1390	90	6.28	312	16.05	15.01
46054	34.26	-120.48	488	20	7.28	315	13.71	13.55
46059	38.05	-129.9	4570	538	7.02	360	15.11	14.26
46066	52.79	-155.05	4445	334	8.06	270	7.47	6.74
46071	51.14	179.12	1313	25	7.59	282	6.10	5.84
46072	51.66	-172.16	3583	71	8.03	270	5.99	5.44
46073	55.03	-172	3474	224	9	0	5.68	4.10
46077	57.89	-154.29	206	20	7.19	40	7.03	5.12
46078	55.99	-152.64	4357	100	7.96	306	7.98	6.82
46082	59.67	-143.39	302	44	6.74	101	8.65	7.40
46086	32.49	-118.03	1844	47	4.31	294	17.40	16.14
46087	48.49	-124.73	259	11	5.09	109	10.02	9.51
46089	45.89	-125.82	2401	141	6.34	346	12.72	11.71
51000	23.54	-153.81	4856	377	6.53	78	23.47	22.35
51004	17.6	-152.4	5098	330	7.55	279	25.35	24.81
51101	24.32	-162.23	4839	145	6.69	79	24.84	23.78

References

Amante, C. and B.W. Eakins (2009). ETOPO1 1 Arc-Minute Global Relief Model: Procedures, Data Sources and Analysis. NOAA Technical Memorandum NESDIS NGDC-24. National Geophysical Data Center, NOAA. doi:10.7289/V5C8276M Accessed: Nov. 13, 2015

Apel, J. R. (1994), An improved model of the ocean surface wave vector spectrum and its effects on radar backscatter, J. Geophys. Res., 99(C8), 16269–16291, doi:10.1029/94JC00846.

Ardhuin, Fabrice, Erick Rogers, Alexander V. Babanin, Jean-François Filipot, Rudy Magne, Aaron Roland, Andre van der Westhuysen, Pierre Queffeulou, Jean-Michel Lefevre, Lotfi Aouf, and Fabrice Collard (2010): Semiempirical Dissipation Source Functions for Ocean Waves. Part I: Definition, Calibration, and Validation. J. Phys. Oceanogr. 40, 1917–1941, doi: 10.1175/2010JPO4324.1.

Ardhuin, Fabrice (2016), Ocean Waves in Geosciences Available: ftp://ftp.ifremer.fr/ifremer/ww3/COURS/waves_in_geosciences_2016.pdf Accessed: July 29, 2016

Atlas, R., Hoffman, R. N., Ardizzone, J., Leidner, S. M., Jusem, J. C., Smith, D. K., and Gombos, D. (2011), A cross-calibrated, multiplatform ocean surface wind velocity product for meteorological and oceanographic applications, B. Am. Meteorol. Soc., 92, 157– 174, 2011.

Banner, M. L., I. S. F. Jones, and J. C. Trinder (1989), Wavenumber spectra of short-gravity waves, J. Fluid Mech., 198, 321–344, doi:10.1017

Barrick, D. E. (1968). Relationship between slope probability density function and the physical
optics integral in rough surface scattering. Proceedings of the IEEE , 56 (10), 1728–1729. doi: 10.1109/PROC.1968.6718

Bass, F. G., & Fuks, I. M. (1979). Wave scattering from statistically rough surfaces (Vol. 93). Elmsford, NY: Pergamon

Beckmann, Petr and André Spizzichino (1987), The Scattering of Electromagnetic Waves from Rough Surfaces, Artech House, Norwood, MA

Booij, N., R. C. Ris and L. H. Holthuijsen, (1999), A third-generation wave model for coastal regions, Part I, Model description and validation, J. Geophys. Res., 104, C4, 7649–7666

Brown, G. (1978), “Backscattering from a Gaussian distributed perfectly conducting rough surface,” IEEE Trans. Antennas Propag., vol. AP-26, no. 3, pp. 472–482, May 1978.

Brown, G. (1990), Chapter 10 Quasi-Specular Scattering from the Air-Sea Interface in Surface Waves and Fluxes, Vol. II – Remote Sensing, Geernaert, G. L. and W. J. Plant, 1990 Eds., Dordrecht, Kluwer Academic Publishers

Cardellach, E., S. G. Jin, and F. Xie (2014), Chapter 8 of GNSS Remote Sensing: Theory, Methods and Applications. New York, London: Springer, 2014.

Chen, D.D.; Gleason, S.; Ruf, C.; Adjrad, M. (2012), "Spectral dependence of the response time of sea state to local wind forcing," in Geoscience and Remote Sensing Symposium (IGARSS), 2012 IEEE International , vol., no., pp.3776-3779, 22-27 July 2012 doi: 10.1109/IGARSS.2012.6350495

Chen, D.D.; Ruf, C.S. (2015), “Adaptive Control of Undetected Radio Frequency Interference With a Spaceborne Microwave Radiometer,” in Geoscience and Remote Sensing, IEEE Transactions on , vol.53, no.9, pp.4972-4984, Sept. 2015 doi: 10.1109/TGRS.2015.2414395

Chen, D. D., C. S. Ruf, and S. T. Gleason (2016), Response time of mean square slope to wind forcing: An empirical investigation, J. Geophys. Res. Oceans, 121, doi:10.1002/2016JC011661

Chu, Peter C., Yiquan Qi, Yuchun Chen, Ping Shi, and Qingwen Mao (2004), South China Sea Wind-Wave Characteristics. Part I: Validation of Wavewatch-III Using TOPEX/Poseidon Data. J. Atmos. Oceanic Technol., 21, 1718–1733, doi: 10.1175/JTECH1661.1.

Clarizia, M. P., Ruf, C.; Jales, P. and Gommenginger, C. (2014), “Spaceborne GNSS-R Minimum Variance Wind Speed Estimator,” IEEE Trans Geosci. Remote Sens., 52(11), 6829-6843, doi: 10.1109/TGRS.2014.2303831, Nov. 2014.

COAPS (Center for Ocean-Atmospheric Prediction Studies) (2016), Scatterometry and Ocean Vector Winds Satellite Studies [Available: https://coaps.fsu.edu/scatterometry/about/overview.php, last accessed Aug. 29, 2016].

Cox, C. S., and W. Munk (1954a), Statistics of the sea surface derived from sun glitter, J. Mar. Res., 13, 198–227.

Cox, C. S., and W. Munk (1954b) “Measurement of the roughness of the sea surface from photographs of the Sun’s glitter,” J. Opt. Soc. Am., vol. 44, no.11, pp. 838–850, 1954.

Donelan, M. A., M. Curcic, S. S. Chen, and A. K. Magnusson, 2012, Modeling waves and wind stress, J. Geophys. Res., 117, C00J23, doi:10.1029/2011JC007787.

Elfouhaily, Chapron, Katsaros and Vandemark, 1997, “A unified directional spectrum for long and short wind-driven waves”, Journal of Geophysical Research, Vol 102, No. C7, pp 15,781-15,796, July 15, 1997.

Entekhabi, D.; Njoku, E.G.; O'Neill, P.E.; Kellogg, K.H.; Crow, W.T.; Edelstein, W.N.; Entin, J.K.; Goodman, S.D.; Jackson, T.J.; Johnson, J.; Kimball, J.; Piepmeier, J.R.; Koster, R.D.; Martin, N.; McDonald, K.C.; Moghaddam, M.; Moran, S.; Reichle, R.; Shi, J.-C.; Spencer, M.W.; Thurman, S.W.; Leung Tsang; Van Zyl, J. (2010), "The Soil Moisture Active Passive (SMAP) Mission," in Proceedings of the IEEE , vol.98, no.5, pp.704-716, May 2010 doi: 10.1109/JPROC.2010.2043918

F. T. Ulaby, R. K. Moore, and A. K. Fung (1986), Microwave Remote Sensing: Active and Passive vol. 3, pp.1649, 1986.

Forristall, G. Z. (1981), Measurements of a saturated range in ocean wave spectra, J. Geophys. Res., 86(C9), 8075–8084, doi:10.1029

Fu, L.-L., E. J. Christensen, C. A. Yamarone Jr., M. Lefebvre, Y. Ménard, M. Dorrer, and P. Escudier (1994), TOPEX/POSEIDON mission overview, J. Geophys. Res., 99(C12), 24369–24381, doi:10.1029/94JC01761.

Garrison, J. L., Komjathy, A., Zavorotny, V. U., & Katzberg, S. J. (2002). Wind speed measurement using forward scattered GPS signals. Geoscience and Remote Sensing, IEEE Transactions On , 40 (1), 50–65. doi: 10.1109/36.981349

Gleason, S. (2006), “Remote sensing of ocean, ice and land surfaces using bistatically scattered GNSS signals from low earth orbit,” Ph.D. dissertation, Univ. Surrey, Guildford, U.K., 2006.

Gleason, S.T., S. Hodgart, S. Yiping, C. Gommenginger, S. Mackin, M. Adjrad, and M. Unwin (2005), “Detection and processing of bistatically reflected GPS signals from low Earth orbit for the purpose of ocean remote sensing,” IEEE Trans. Geosci. Remote Sensing, vol. 43, no. 6, pp. 1229–1241, June 2005.

Gleason, S., C. Ruf, M. P. Clarizia, A. O’Brien (2016), “Calibration and Unwrapping of the Normalized Scattering Cross Section for the Cyclone Global Navigation Satellite System (CYGNSS),” IEEE Trans. Geosci. Remote Sens., doi: 10.1109/TGRS.2015.2502245, 2016.

H*WIND. Available: http://www.aoml.noaa.gov/hrd/Storm_pages/ivan2004/wind.html

Hasselmann, K. et al. (1973), "Measurements of wind-wave growth and swell decay during the Joint North Sea Wave Project (JONSWAP)", Dtsch. Hydrogh. Z., Suppl. A, 8, 12, 95pp.

Holthuijsen, L. H. (2007), Waves in Oceanic and Coastal Waters, Cambridge University Press, New York

Hughes, B. A., Grant, H. L., & Chappell, R. W. (1977). A fast response surface-wave slope meter and measured wind-wave moments. Deep Sea Research, 24(12), 1211-1223.

Hwang, P. A., and O. H. Shemdin (1988), The dependence of sea surface slope on atmospheric stability and swell conditions, J. Geophys. Res., 93(C11), 13903–13912, doi:10.1029/JC093iC11p13903.

Hwang, P. A., and D. W. Wang (2004b), An empirical investigation of source term balance of small scale surface waves, Geophys. Res. Lett., 31, L15301, doi:10.1029/2004GL020080.

Hwang, P.A., and David W. Wang (2004a): Field Measurements of Duration-Limited Growth of Wind-Generated Ocean Surface Waves at Young Stage of Development*. J. Phys. Oceanogr., 34, 2316–2326. doi: http://dx.doi.org/10.1175/1520-0485(2004)034<2316:FMODGO>2.0.CO;2

Hwang, P. A., and David W. Wang (2005a): CORRIGENDUM*. J. Phys. Oceanogr., 35, 268–270. doi: http://dx.doi.org/10.1175/JPO-2731.1

Hwang, P. A. (2005b), Wave number spectrum and mean square slope of intermediate-scale ocean surface waves, J. Geophys. Res., 110, C10029, doi:10.1029/2005JC003002.

Hwang, P.A., Francisco J. Ocampo-Torres, and Héctor García-Nava (2012): Wind Sea and Swell Separation of 1D Wave Spectrum by a Spectrum Integration Method*. J. Atmos. Oceanic Technol., 29, 116–128. doi: http://dx.doi.org/10.1175/JTECH-D-11-00075.1

Hwang, P.A., Derek M. Burrage, David W. Wang, and Joel C. Wesson (2013): Ocean Surface Roughness Spectrum in High Wind Condition for Microwave Backscatter and Emission Computations*. J. Atmos. Oceanic Technol., 30, 2168–2188. doi: http://dx.doi.org/10.1175/JTECH-D-12-00239.1

Hwang, P. A., and F. Fois (2015), Surface roughness and breaking wave properties retrieved from polarimetric microwave radar backscattering, J. Geophys. Res. Oceans, 120, 3640–3657, doi:10.1002/2015JC010782.

Hwang, Paul A. (2016), Fetch- and Duration-Limited Nature of Surface Wave Growth inside Tropical Cyclones: With Applications to Air–Sea Exchange and Remote Sensing. J. Phys. Oceanogr., 46, 41–56, doi: 10.1175/JPO-D-15-0173.1.

Jackson, F. C., W. T. Walton, D. E. Hines, B. A. Walter, and C. Y. Peng (1992), Sea surface mean-square slope from Ku-band backscatter data, J. Geophys. Res., 97, 11,411– 11,427.

Jales, P., and M. Unwin (2015a), “Mission description - GNSS reflectometry on TDS-1 with the SGR-ReSI,” Tech. Rep. SSTL report No. 0248367 Revision 001, Surrey Satellite Technology Ltd; Available from http://www.merrbys.co.uk.

Jales, P., (2015b), “MERRByS Product Manual - GNSS Reflectometry on TDS-1 with the SGR-ReSI,” Tech. Rep. SSTL report No. 0248366 Revision 001, Surrey Satellite Technology Ltd; Available from http://www.merrbys.co.uk.

Kahma, Kimmo K. and Charles J. Calkoen (1992), Reconciling Discrepancies in the Observed Growth of Wind-generated Waves. J. Phys. Oceanogr., 22, 1389–1405. doi: http://dx.doi.org/10.1175/1520-0485(1992)022<1389:RDITOG>2.0.CO;2

Katzberg, S. J., J. Dunion, and G. G. Ganoe (2013), The use of reflected GPS signals to retrieve ocean surface wind speeds in tropical cyclones, Radio Sci., 48, 371–387, doi:10.1002/rds.20042.

Komen, G. J., L. Cavaleri, M. Donelan, K. Hasselmann, S. Hasselmann, and P. A. E. M. Janssen, Eds.,1994: Dynamic and Modelling of Ocean Waves. Cambridge University Press, 532 pp.

Komjathy, A., V. U. Zavorotny, P. Axelrad, G. H. Born, and J. L. Garrison, “GPS signal scattering from sea surface: Wind speed retrieval using experimental data and theoretical model,” Remote Sens. Environ., vol. 73, no. 1, pp. 162–174, 2000.

Li Li; Chang, P. (1996), "Ocean surface wind speed and direction retrievals from the SSM/I," Geoscience and Remote Sensing Symposium, 1996. IGARSS '96. 'Remote Sensing for a Sustainable Future.', International, vol.3, no., pp.1707-1709 vol.3, 27-31 May 1996

Lin, B., S. J. Katzberg, J. L. Garrison, and B. A. Wielicki (1999), Relationship between GPS signals reflected from sea surfaces and surface winds: Modeling results and comparisons with aircraft measurements, J. Geophys. Res., 104(C9), 20713–20727, doi:10.1029/1999JC900176.

Liu, Y., Yan, X. H., Liu, W. T., & Hwang, P. A. (1997). The probability density function of ocean surface slopes and its effects on radar backscatter. Journal of physical oceanography, 27(5), 782-797.

Lyzenga, D. R., and J. R. Bennett (1988), Full-spectrum modeling of synthetic aperture radar internal wave signatures, J. Geophys. Res., 93(C10), 12345–12354, doi:10.1029/JC093iC10p12345.

Marchan-Hernandez, N. Rodriguez-Alvarez, A. Camps, X. Bosch-Lluis, I. Ramos-Perez and E. Valencia, "Correction of the Sea State Impact in the L-Band Brightness Temperature by Means of Delay-Doppler Maps of Global Navigation Satellite Signals Reflected Over the Sea Surface," in IEEE Transactions on Geoscience and Remote Sensing, vol. 46, no. 10, pp. 2914-2923, Oct. 2008.
doi: 10.1109/TGRS.2008.922144

Martin, Seelye (2014), An Introduction to Ocean Remote Sensing, Cambridge University Press; 2nd edition.

Moghaddam, M.; Moran, S.; Reichle, R.; Shi, J.-C.; Spencer, M.W.; Thurman, S.W.; Leung Tsang; Van Zyl, J. (2010), "The Soil Moisture Active Passive (SMAP) Mission," in Proceedings of the IEEE , vol.98, no.5, pp.704-716, May 2010 doi: 10.1109/JPROC.2010.2043918

Munk, W. H., (1950), Origin and generation ofwaves, Proc. 1st Conf. Coastal Engineering (Long Beach), New York, ASCE

N. Pierdicca, L. Guerriero, R. Giusto, M. Brogioni, A. Egido (2014), “SAVERS: A simulator of GNSS reflections from bare and vegetated soils,” IEEE Trans. Geosci. Remote Sensing, vol. 52, no. 10, pp. 6542–6554, 2014.

NASA's Ocean Biology Processing Group (2009), “Distance to the Nearest Coast”, June 2009. Available: http://oceancolor.gsfc.nasa.gov/DOCS/DistFromCoast Accessed: Nov. 13, 2015

National Data Buoy Center (NDBC), Dec. 8, 2015b Measurement Descriptions and Units. Available: http://www.ndbc.noaa.gov/measdes.shtml

National Data Buoy Center (NDBC) (1996), Nondirectional and directional wave data analysis procedures, NDBC Tech. Doc. 96-01. [Available
at http://www.ndbc.noaa.gov/wavemeas.pdf, last accessed 1 Dec. 2015.]

National Data Buoy Center (NDBC) (2002), Non-standard acquisition times. [Available at http://www.ndbc.noaa.gov/nsacq.shtml, last
accessed 6 Dec. 2015.]

National Data Buoy Center (NDBC) (2009a), At what heights are the sensors located on Moored Buoy and at C-MAN sites?. [Available at
http://www.ndbc.noaa.gov/bmanht.shtml, last accessed 6 Dec. 2015.]

National Data Buoy Center (NDBC) (2009b), What are the sensors’ reporting, sampling, and accuracy readings?. [Available at http://www.
ndbc.noaa.gov/rsa.shtml, last accessed 6 Dec. 2015.]

National Data Buoy Center (NDBC) (2012a), Do NDBC’s meteorological and oceanographic sensors measure data for the entire hour?.
[Available at http://www.ndbc.noaa.gov/acq.shtml, last accessed 22 Dec. 2015.]

National Data Buoy Center (NDBC) (2012b), Wave acquisition times. [Available at http://www.ndbc.noaa.gov/waves.shtml, last accessed 6
Dec 2015.]

National Data Buoy Center (NDBC) (2015a), Measurement Descriptions and Units. [Available at http://www.ndbc.noaa.gov/measdes.shtml, last accessed 15 Aug. 2016.]

National Data Buoy Center (NDBC) (2015b), Historical NDBC Data. [Available at http://www.ndbc.noaa.gov/historical_data.shtml, last accessed 16 Dec. 2015.]

Phillips, O. M. (1958), The equilibrium range in the spectrum of wind generated waves, J. Fluid Mech., 4, 426–434.

Pierson W.J., and L. Moskowitz (1964), “A proposed spectral form for fully developed wind seas based on the similarity theory of S.A. Kitaigordskii”, Journal of Geophysical Research 69: 5181–5190, 1964.

Plant, W. J., W. C. Keller, V. Hesany, T. Hara, E. Bock, and M. A. Donelan (1999), Bound waves and Bragg scattering in a wind-wave tank, J. Geophys. Res., 104(C2), 3243–3263, doi:10.1029/1998JC900061.

Plant, W. J. (2003). A new interpretation of sea-surface slope probability density functions. Journal of Geophysical Research: Oceans, 108(C9).

Plant, W. J. (2015), Short wind waves on the ocean: Wavenumber-frequency spectra, J. Geophys. Res. Oceans, 120, doi:10.1002/2014JC010586.

Reichl, B. G., T. Hara, and I. Ginis (2014), Sea state dependence of the wind stress over the ocean under hurricane winds, J. Geophys. Res. Oceans, 119, 30–51, doi:10.1002/2013JC009289.

Remote Sensing Systems (2016), WindSat, [Available http://www.remss.com/missions/windsat, last accessed Aug. 29, 2016].

Ross, V., & Dion, D. (2007). Sea surface slope statistics derived from Sun glint radiance measurements and their apparent dependence on sensor elevation. Journal of Geophysical Research: Oceans, 112(C9).

Ruf, C. S. et al. (2012), "The CYGNSS nanosatellite constellation hurricane mission," 2012 IEEE International Geoscience and Remote Sensing Symposium, Munich, 2012, pp. 214-216.

doi: 10.1109/IGARSS.2012.6351600

Ruf, C. S., R. Atlas, P. S. Chang, M. P. Clarizia, J. L. Garrison, S. Gleason, S. J. Katzberg, Z. Jelenak, J. T. Johnson, S. J. Majumdar, A. O'Brien, D. J. Posselt, A. J. Ridley, R. J. Rose, V. U. Zavorotny (2016a), "New Ocean Winds Satellite Mission to Probe Hurricanes and Tropical Convection," Bull. Amer. Meteor. Soc., doi:10.1175/BAMS-D-14-00218.1, pp385-395, Mar 2016.

Ruf, C., P. Chang, M.P. Clarizia, S. Gleason, Z. Jelenak, J. Murray, M. Morris, S. Musko, D. Posselt, D. Provost, D. Starkenburg, V. Zavorotny (2016b), CYGNSS Handbook, Ann Arbor, MI, Michigan Pub., ISBN 978-1-60785-380-0, 154 pp, 1 Apr 2016.

Smith, S. D. (1988), Coefficients for sea surface wind stress, heat flux, and wind profiles as a function of wind speed and temperature, J. Geophys. Res., 93(C12), 15467–15472, doi:10.1029/JC093iC12p15467.

Stewart, Robert (2008), "Introduction to Physical Oceanography", [Online]. Available: http://oceanworld.tamu.edu/home/course_book.htm, Sept. 2008, pp. 285, pp. 288, pp. 46, pp. 121

Teng, Chung-Chu, Stephen Cucullu, Shannon McArthur, Craig Kohler, Bill Burnett, Landry Bernard (2010), "Vandalism of Data Buoys", Mariners Weather Log Vol.54 No. 1 April 2010. Available: http://www.vos.noaa.gov/MWL/apr_10/vandalism.shtml Accessed: Dec. 31, 2015

Tian, Zhigang and Perlin, Marc and Choi, Wooyoung (2008), Evaluation of a deep-water wave breaking criterion, Physics of Fluids, 20, 066604 (2008), DOI: http://dx.doi.org/10.1063/1.2939396

Tian, Zhigang; Wooyoung Choi (2013), Evolution of deep-water waves under wind forcing and wave breaking effects: Numerical simulations and experimental assessment, European Journal of Mechanics - B/Fluids, Volume 41, September–October 2013, Pages 11-22, ISSN 0997-7546, http://dx.doi.org/10.1016/j.euromechflu.2013.04.001.
(http://www.sciencedirect.com/science/article/pii/S0997754613000320)

Thompson, D. R., Elfouhaily, T. M., & Garrison, J. L. (2005). An improved geometrical optics model for bistatic GPS scattering from the ocean surface. Geoscience and Remote Sensing, IEEE Transactions On , 43 (12), 2810–2821. doi: 10.1109/TGRS.2005.857895

Tolman, H. L. and the WAVEWATCH III Development Group, March (2014): User manual and system documentation of WAVEWATCH III version 4.18. NOAA / NWS / NCEP / MMAB Technical Note 316

Ulaby, F. T., Richard K. Moore, and Adrian K. Fung (1982), Microwave Remote Sensing, Active and Passive, Vol. II: Radar Remote Sensing and Surface Scattering and Emission Theory, Addison-Wesley Publishing Company, Inc.

U.S. Army Coastal Engineering Research Center (CERC) (1977), "Shore protection manual, 3rd Edition Volume 1”.

Valenzuela, G.R. (1978) "Theories for the Interaction of Electromagnetic and Oceanic Waves: A Review," Bdry-Layer Met., 13, p. 61, 1978.

Voronovich, A. G., and V. U. Zavorotny (2001), Theoretical model for scattering of radar signals in Ku and C bands from a rough sea surface with breaking waves, Waves Rand. Media, 11, 247– 269.

Vos van Steenwijk, R. de, M. Unwin and P. Jales (2010), "Introducing the SGR-ReSI: A next generation spaceborne GNSS receiver for navigation and remote-sensing," 2010 5th ESA Workshop on Satellite Navigation Technologies and European Workshop on GNSS Signals and Signal Processing (NAVITEC), Noordwijk, 2010, pp. 1-7.
doi: 10.1109/NAVITEC.2010.5708063

WAMDI Group, The (1988), The WAM Model—A Third Generation Ocean Wave Prediction Model. J. Phys. Oceanogr., 18, 1775–1810, doi: 10.1175/1520-0485(1988)018<1775:TWMTGO>2.0.CO;2.

Weissman, D. E., W. J. Plant, and S. Stolte (1996), Response of microwave cross sections of the sea to wind fluctuations, J. Geophys. Res., 101(C5), 12149–12161, doi:10.1029/96JC00558.

Wilheit, T.T. (1979), "A Model for the Microwave Emissivity of the Ocean's Surface as a Function of Wind Speed," Geoscience Electronics, IEEE Transactions on , vol.17, no.4, pp.244-249, Oct. 1979

Willoughby, H. E. and M. E. Rahn (2004), Parametric Representation of the Primary Hurricane Vortex. Part I: Observations and Evaluation of the Holland (1980) Model. Mon. Wea. Rev., 132, 3033–3048, doi: 10.1175/MWR2831.1.

Yalin Fan, Isaac Ginis, and Tetsu Hara (2009), The Effect of Wind–Wave–Current Interaction on Air–Sea Momentum Fluxes and Ocean Response in Tropical Cyclones. J. Phys. Oceanogr., 39, 1019–1034, doi: 10.1175/2008JPO4066.1.

Young, I. R., L.A. Verhagen (1996), The growth of fetch limited waves in water of finite depth. Part 1. Total energy and peak frequency, Coastal Engineering, Volume 29, Issues 1–2, December 1996, Pages 47-78, ISSN 0378-3839, http://dx.doi.org/10.1016/S0378-3839(96)00006-3.

Young, I. R. (1998), An experimental investigation of the role of atmospheric stability in wind wave growth, Coastal Engineering, Volume 34, Issues 1–2, July 1998, Pages 23-33, ISSN 0378-3839, http://dx.doi.org/10.1016/S0378-3839(98)00011-8.

Young, I. R. (1999), Wind Generated Ocean Waves, Elsevier, Amsterdam

Yueh, S.; Stiles, B.; Liu, W.T. (2003), "QuikSCAT wind retrievals for tropical cyclones," OCEANS 2003. Proceedings, vol.2, no., pp.1045 Vol.2, 22-26 Sept. 2003

Yueh, S. H., W. J. Wilson, S. V. Nghiem, F. K. Li and W. B. Ricketts (1994), "Polarimetric passive remote sensing of ocean wind vectors," Geoscience and Remote Sensing Symposium, 1994. IGARSS '94. Surface and Atmospheric Remote Sensing: Technologies, Data Analysis and Interpretation., International, Pasadena, CA, 1994, pp. 2416-2418 vol.4.
doi: 10.1109/IGARSS.1994.399755

Zavorotny, V.U.; Voronovich, A.G., (2000), "Scattering of GPS signals from the ocean with wind remote sensing application," in Geoscience and Remote Sensing, IEEE Transactions on , vol.38, no.2, pp.951-964, Mar 2000 doi: 10.1109/36.841977

Zavorotny, S. Gleason, E. Cardellach and A. Camps (2014), "Tutorial on Remote Sensing Using GNSS Bistatic Radar of Opportunity," in IEEE Geoscience and Remote Sensing Magazine, vol. 2, no. 4, pp. 8-45, Dec. 2014. doi: 10.1109/MGRS.2014.2374220

Zavorotny, V. (2016), "Appendix. Ocean Surface Bistatic Scattering Forward Model" in CYGNSS Handbook, Ann Arbor, MI, Michigan Pub., ISBN 978-1-60785-380-0, 154 pp, 1 Apr 2016.